MEMS Technologies for Energy Harvesting and Sensing

Ronnie Varghese

Dissertation submitted to the faculty of the
Virginia Polytechnic Institute and State University
in partial fulfillment of the requirements for the degree of

Doctor of Philosophy
In
Materials Science and Engineering

Shashank Priya (Chair)

Alex O. Aning

Jean Heremans

William Reynolds

25th July 2013

Blacksburg, VA

Keywords: Energy Harvesting, MEMS, Piezoelectric, Magnetoelectric, Magnetostriction

MEMS Technologies for Energy Harvesting and Sensing

Ronnie Varghese

Abstract

MEMS devices are finding application in diverse fields that include energy harvesting, microelectronics and sensors. In energy harvesting, MEMS scale devices are employed due to its efficiencies of scale. The miniaturization of energy harvesters permit them to be integrated as the power supply for sensors often in the same package and also extends their use to remote and extreme ambient applications. Unlike inductive harvesting, piezoelectric and magnetoelectric devices lend easily to MEMS scaling. The processing of such Piezo-MEMS devices often requires special fabrication, characterization and testing techniques. Our research work has focused on the development of the various technologies for a) the better characterization of the constituent materials that make up these devices, b) the conceptualization and structural design of unique MEMS energy harvesters and finally c) the development of the unit operations (many novel) for fabrication and the mechanical and electrical testing of these devices.

In this research work, we have pioneered some new approaches to the characterization of thin films utilized in Piezo-MEMS devices: (1) Temperature –Time Transformation (TTT) diagrams are used to document texture evolution during thermal treatment of ceramics. Multinomial and multivariate regression techniques were utilized to create the predictor models for TTT data of $Pb(Zr_{0.60}Ti_{0.40}O_3)$ sol-gel thin films. (2) We correlated the composition (measured using Energy

Dispersive X-ray analysis (EDX) and Electron Probe Micro Analysis (EPMA)) of $Pb(Zr_{0.52}Ti_{0.48}O_3)$ RF sputtered thin films to its optical dispersion properties measured using Variable Angle Spectroscopic Ellipsometry (VASE). Wemple-DiDomenico, Jackson-Amer, Tauc and Urbach optical dispersion factors and Lorentz Lorenz polarizability relationships were combined to realize a model for predicting the elemental content of any thin film system. (3) We developed in house capability for strain analysis of magnetostrictive thin films using laser Doppler Vibrometry (LDV). We determined a methodology to convert the displacements measurements of AC magnetic field induced vibrations of thin film samples into magnetostriction values. (4) Finally, we report the novel use of a thermo-optic technique, Time Domain Thermoreflectance (TDTR) in the study of Pb(Zr,Ti)O3 (PZT) thin film texturing. Time Domain Thermoreflectance (TDTR) has been proved to be capable of measuring thermal properties of atomic layers and interfaces. Therefore, we utilized TDTR to analyze and model the heat transport at the nano scale and correlate with different PZT crystalline orientations.

To harvest energy at the low frequency (<100Hz) of ambient vibrations, MEMS energy harvesters require special structures. Extensive research has led us to the development of Circular Zigzag structure that permits inertial mass free attainment of such low frequencies. In addition to Si micromachining, we have fabricated such structures using a new Micro water jet micromachining of thin piezo sheets, unimorphs and bimorphs. For low frequency magnetic energy harvesting, we also fabricated the first magnetoelectric macro fiber composite. This device also employs a novel low temperature metallic bonding technique to fuse the magnetostrictive layer to the piezoelectric layers. A special low viscosity epoxy enabled the joining of the flexible circuit to the magnetoelectric fibers. Lastly, we developed a nondimensional tunable Piezo harvester, called PiezoCap, which decouples the energy harvesting

component of the device from the resonant vibration component. We do so by using magnets loaded on piezo harvester strips, thereby making them piezomagnetoelastic and vary the spacing between 2 magnet+piezoelectric pairs to eliminate dimensionality and permit active tunability of the harvester's resonant frequency.

Acknowledgements

This research was completed under the tutelage of my Advisor, Dr. Shashank Priya, and guidance of my Advisory Committee of Dr. Alex Aning, Dr. Jean Heremans and Dr. William Reynolds. I am grateful for the assistance and support from my colleagues in Bio-inspired Materials and Device Laboratory (BMDL), Center for Energy Harvesting and Systems (CEHMS) and Center for Intelligent Material Systems and Structures (CIMSS), my friends and family. My tenure at Virginia Tech was especially made comfortable by the timely and gracious advisory, administrative and technical support from Jamie Archual, Justin Farmer, Ai Fukushima, Kim Grandstaff, Beth Howell, Donald Leber, Lauren Mills, Ben Poe and Erin Singleton.

Table of Contents

List of Figures

List of Tables

Chapter 1

Introduction

Scope, Purpose and Significance of Research

Energy harvesting is the field in which various transduction mechanisms are utilized to convert excess or vestigial sources of energy into useful energy. Vibrational energy is one of the most common sources of ambient waste energy. Piezoelectric and electromagnetic transduction schemes are the most popular for vibrational energy conversion. Miniaturization of wireless sensors, autonomous electronic systems and harsh environment or remote sensor nodes require the scaling down of energy harvesters to the MEMS scale.

Figure 1.1 delineates the range of operation of piezoelectric MEMS vs. the electromagnetic energy harvester[1]. With decrease in size, piezoelectric MEMS devices become the preferred mode of transduction.

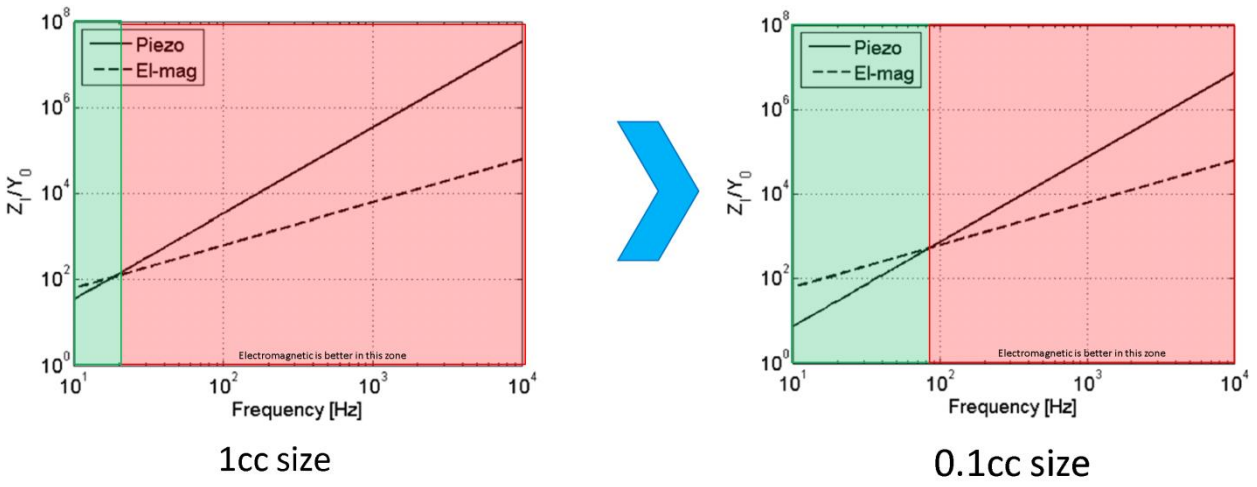

Figure 1.1 Z_l/Y_0 ratio, a measure of the ability to convert energy (Z_l is the max energy harvester displacement and Y_o is the source vibration amplitude) vs. type of transduction vs. device size (© IOP Publishing. Reproduced with permission. All rights reserved)

A piezoelectric MEMS harvester comprises of a Piezo thin film element on an elastic cantilever which transfers the source vibration into the device. Therefore, the fabrication of such a device includes the development and characterization of the piezoelectric thin film, the development and fabrication of the MEMS cantilever structure and finally the MEMS device characterization. In this research, we explore different concepts of Energy Harvester devices from the perspective of structural resonance frequency, band width of operation, ease of manufacturability, tunability and versatility. With the addition of a magnetostrictive layer, the Piezo MEMS can double as a Magnetoelectric MEMS harvester.

Most vibrational sources of energy in nature and industry have a frequency signature < 1kHz. Often these ambient frequencies are in the < 100Hz range and therefore, the focus of most MEMS energy harvesting research has been to achieve that level of operation. As the fundamental frequency of a simple cantilever beam is given as $\frac{1}{2\pi}\sqrt{k/m}$, where k is the stiffness

(proportional to $width \times \frac{thickness^3}{length^3}$) and m is the mass (proportional to $width \times thickness \times length$), when dimensions reduce to micron sizes, the natural frequency of a simple cantilever scale higher than that in the macro scale. Therefore, considerable emphasis in research has been placed in discovering low frequency structures in the MEMS scale. These structures tend to have non-standard and non-linear shapes that are attuned for low frequency vibrational energy transfer.

Dissertation Structure

The active element in a Piezoelectric or Magnetoelectric MEMS device is the piezoelectric thin film which in our case is PZT, Lead Zirconium Titanate. We therefore delved into the development of PZT thin film by sol-gel spin coating and RF sputtering techniques. For the magnetostrictive component, we developed NFO, Nickel Ferrite, thin films by RF sputtering. During the detailed characterization of these films, we discovered some gaps in existing metrology and predictive data modeling and proceeded to resolve them.

The first area of derivative research was in Ceramic Data Analytics of $Pb(Zr_{0.60}Ti_{0.40}\ O_3)$ sol-gel thin films. We describe an analytical model to define the temperature-time-transformation (TTT) diagram of sol-gel deposited $Pb(Zr,Ti)O_3$ thin films on platinized silicon substrates. Texture evolution in film occurred as the pyrolysis and thermal annealing conditions were varied. We demonstrate that the developed model can quantitatively predict the outcome of thermal treatment conditions in terms of texture evolution. Multinomial and multivariate regression techniques were utilized to create the predictor models for TTT data. Further, it was found that

multinomial regression can provide better fit as compared to standard regression and multivariate regression. We have generalized this approach so that it can be applied to other thin film deposition techniques and bulk ceramics.

The second area of derivative research was in Photo Elemental Analysis of $Pb(Zr_{0.52}Ti_{0.48}O_3)$ RF sputtered thin films. This work provides the correlation between the compositions of a given thin film to its optical dispersion properties. Gladstone-Dale (G-D) relationships have been used in optical mineralogy to relate density of crystalline compounds to their average refractive index. We purport to use a 'reverse' G-D approach and determine the composition of multi-component thin films from their optical properties. As a model system, we focused on complex perovskite ferroelectric thin film and applied the derived relationship to determine the stoichiometry. The wavelength dispersion of refractive index and extinction coefficient of various $Pb(Zr,Ti)O_3$ (PZT) thin films was measured using Variable Angle Spectroscopic Ellipsometry (VASE). Elemental compositions were measured using Energy Dispersive X-ray analysis (EDX) and Electron Probe Micro Analysis (EPMA). Wemple-DiDomenico, Jackson-Amer, Tauc and Urbach optical relationships were used to extract correlations to elemental content. Also, theoretical and semi-empirical approaches to calculate the electronic polarizability of PZT were employed and their variation with elemental content was computed. Perovskite tolerance and octahedral factors were also analyzed against the optical and polarizability parameters. These factors and relationships were combined to realize a model for predicting the elemental content of a thin film system.

A third area of derivative research was in the development of in house capability for strain analysis of magnetostrictive thin films. As we are well equipped to measure vibrations using laser Doppler Vibrometry (LDV), we embarked on determining a methodology to convert the

displacements measurements of AC magnetic field induced vibration of thin film samples into magnetostriction values.

A fourth area of derivative research was in the quest for a materials characterization technique to detect differences in interfacial layers of a few atomic layers. These atomic layers are claimed to determine texturing of PZT thin films grown over platinized Si substrates. After futile attempts at using Raman Scattering, FTIR, TEM and XRD techniques, we were unable to settle on a well-established materials characterization technique that had the spatial resolution and the sensitivity to detect these texturing atomic layers. Time Domain Thermoreflectance (TDTR) has been proven to be capable of measuring thermal properties of atomic layers and especially that at interfaces. Therefore, we explored the use of TDTR to correlate with PZT texturing trends.

Chapter 6-7 will introduce device designs and concepts for energy harvesting in and with alternating magnetic fields and vibrations. The straightforward concept is to take the Piezo MEMS described in Chapter 8 and apply a magnetostrictive layer like Nickel Ferrite ($NiFe_2O_4$) over the Piezo capacitor. Another tactic employed is the development of energy harvesting concepts that will fit in the same foot print of a fully packaged MEMS device but circumvents intensive and sensitive wafer processing. A MEMS device requires special vacuum packaging to prevent damage and minimize air damping. For the most low frequency MEMS structures, the package can extend to dimensions of almost 25mm x 25mm x 20mm. In such a volume, we can supplement the wafer based MEMS approach with non-wafer based solutions. On the non-wafer side, we developed a MEMS scalable prototype of a) a magnetically levitated system with piezoelectric macro fiber composite harvesters and b) a magnetoelectric macro fiber composite (ME MFC) simple cantilever. The former, called PiezoCap, delivered on its design objectives and then made one giant leap forward by revealing to us a methodology to make vibration piezo

harvesters non-dimensional. PiezoCap resonance frequency is tuned purely by magnetic stiffness force. The ME MFC was developed with better magnetoelastic coupling to the piezo realized by using a low temperature solder bonding process between the magnetostrictive ferrite and the piezo.

Chapter 8 describes the approach undertaken to achieve a low frequency Piezo MEMS energy harvester. The study of various cantilevered structures to determine the path to attain low frequency. We describe our unique fabrication methodology to realize these structures. We also describe the extensive work that went into MEMS wafer test bench setup. A circular labyrinth structure was proven to achieve <100Hz resonant energy harvesting operation whilst generating ample power at low acceleration of 0.1g. Micro water jet cutting is introduced as a bulk Piezo micromachining technique.

Chapter 9 divulges methodologies to improve the oxidation resistance of copper ink for direct writing purposes. We utilize technology from the dispersion strengthening of copper to do so without adversely affecting electrical conductivity.

Chapter 11 will divulge studies completed on a) the additive fabrication methodology for Piezo thin film based transformers and b) flow induced vibration energy harvesters.

References

[1] Mitcheson PD, Reilly EK, Toh T, Wright PK, Yeatman EM. Performance limits of the three MEMS inertial energy generator transduction types. Journal of Micromechanics and Microengineering 2007;17:S211.

Chapter 2

Temperature-time Transformation Diagram for Pb(Zr,Ti)O3 Thin Films [1]

Ronnie Varghese, Matthew Williams[1], Shashaank Gupta, and Shashank Priya[*]

Center for Energy Harvesting Materials and Systems (CEHMS), Department of Materials Science and Engineering, Virginia Tech, Blacksburg, VA 24061.

[1]Department of Statistics, Virginia Tech, Blacksburg, VA 24061.

Abstract

In this paper, we describe an analytical model to define the temperature-time- transformation (TTT) diagram of sol-gel deposited $Pb(Zr,Ti)O_3$ thin films on platinized silicon substrates. Texture evolution in film occurred as the pyrolysis and thermal annealing conditions were varied. We demonstrate that the developed model can quantitatively predict the outcome of thermal treatment conditions in terms of texture evolution. Multinomial and multivariate regression techniques were utilized to create the predictor models for TTT data. Further, it was found that multinomial regression can provide better fit as compared to standard regression and multivariate regression. We have generalized this approach so that it can be applied to other thin film deposition techniques and bulk ceramics.

Keywords: Thin films; piezoelectric ; texturing; multiple regression

[1] Reprinted with permission from [J. Appl. Phys. 110, 014109 (2011)]. Copyright [2011], AIP Publishing LLC

Introduction

$Pb(Zr,Ti)O_3$ (PZT) thin films deposited using sol-gel process, a chemical solution deposition (CSD) technique, are frequently used in micro-electronics industry. This industry focus has lead to detailed studies on the effect of sol-gel process variables on texturing of PZT films. It is well-known that piezoelectric properties are maximized along certain crystallographic direction depending upon the parent phase symmetry. To exemplify, <001> oriented single crystals of morphotropic phase boundary composition 0.92 $Pb(Zn_{1/3}Nb_{2/3})O_3$ – $0.08PbTiO_3$ (PZNT) have been shown to possess high electromechanical coupling coefficients of 0.94, high piezoelectric constants of between 2000 and 2500 pC/N and high electrically induced strains of 1.7%.[1],[2],[3],[4] Park and Shrout attributed this high electromechanical performance to domain engineered state achieved through polarization rotation from <111> to <001>.[3],[4] First principles calculations have indicated that the transformation under electric field between ferroelectric rhombohedral and ferroelectric tetragonal phases proceeds by rotation of the polarization between <111> and <001>, via the <110>.[5] This rotation causes a large coupling between the polarization and electric field causing a giant piezoresponse. In general, a rhombohedral composition oriented along <100> direction and a tetragonal composition oriented along <111> direction will exhibit optimum magnitude of electromechanical coefficients[6]. Thus, texturing is desired in PZT but poses several challenges in synthesis. The growth of bulk PZT in single crystal or textured form has been difficult due to the incongruent melting of ZrO_2. However, PZT films can be textured due to the low annealing temperature required to achieve proper crystallinity. The questions which we pose in this study are: “How to predict the texture of sol-gel deposited PZT thin films with high degree of confidence?”; and “Can a generalized

mathematical model be developed for predicting the texture in ferroelectric materials in terms of synthesis parameters for any given synthesis process?".

There are numerous variables in sol-gel deposition process including choice of bottom electrode, interfacial layers, precursor chemistry and concentration, solvent, chelating agents, dilution rate (determined by molarity and effects viscosity of sol), hydrolysis ratio, spin coating speed and times, and pyrolysis and annealing conditions (including ramp up and down rates)[7]. The innumerability of the variables presents the difficulty in optimizing the conditions for achieving high texture degree. Further, it makes the deposition process susceptible to human errors. This is evident from the fact that a large pool of data exists in literature on sol-gel deposition of PZT thin films but the research has shown that there exists significant variation in the measured results across the laboratories. For repeatability, current methodology requires detailed documentation of process conditions and procedures and access to similar type of equipment and starting material. The situation becomes more complex when one is looking for specific texture in the deposited film. This describes the motivation behind our study. We focus on developing mathematical criterion for predicting the texture in sol-gel deposited thin films by fixing many of the variables and just varying the pyrolysis and thermal annealing conditions. These two variables are most commonly used to modulate the phase of the films and thus we could refer to them as "texture controlling parameters" (TCP).

In PZT sol-gel studies, Temperature-Time-Transformation (TTT) diagrams have been developed to represent the variation of texture as a function of TCP[8]. These diagrams are commonly invoked to understand the texturing mechanisms[9],[10] and quantify the operating regime for achieving specific orientation. However, these diagrams are just pictorial guides specific to a given sol-gel deposition process. Besides, these guides can be misleading as they can only depict

the dominant crystalline phase or texture and do not provide the reader with an understanding of the extent of the other mixture of phases. Mathematical modeling of the TCP data has never been attempted and therefore, no predictor models are available. This paper attempts to fill that void by proposing a statistical methodology to predict the crystalline orientation. The ability to define the boundaries in terms of TCP will allow repeatability in synthesis of textured films.

Polycrystalline thin films can have one or two predominant crystalline orientation. Compiling XRD data from several samples can lead to binary trends, that is, higher the texturing in one orientation lower it is in the other possible orientations. In case of PZT 60/40 (where Zr = 0.60 and Ti = 0.40 mol fraction) thin films, the three dominant textures are <100>, <110> and <111> and therefore the data can be considered trinomial and interdependent. Standard multiple regression methods cannot adequately describe these interdependent responses and so multivariate regression is recommended. But multivariate regression approaches can be complicated and difficult. Thus, a non-linear simultaneous or multinomial regression approach is proposed and compared to consecutive multiple and simultaneous multivariate linear regression approaches.

Experimental Procedure

The sol-gel deposition process was optimized from that described in Reference [11] and consists of the following steps (see figure below): (1) preparation of the sol from Pb, Zr and Ti precursors in a glove box, (2) spin coating of the sol onto the substrate, (3) pyrolysis of the sol-gel thin film on a hot plate to remove solvents and organics and, (4) densification and crystallization of the thin film in a high temperature tube furnace. The mixture of individual sols results in a final composition of 0.4M $Pb_{1.1}(Zr_xTi_{1-x})O_3$ with x = 0.6. An extra 10% Pb was included to

compensate for the losses during thermal treatments as PbO has high vapor pressure of 2Torr at 700^{o}C.

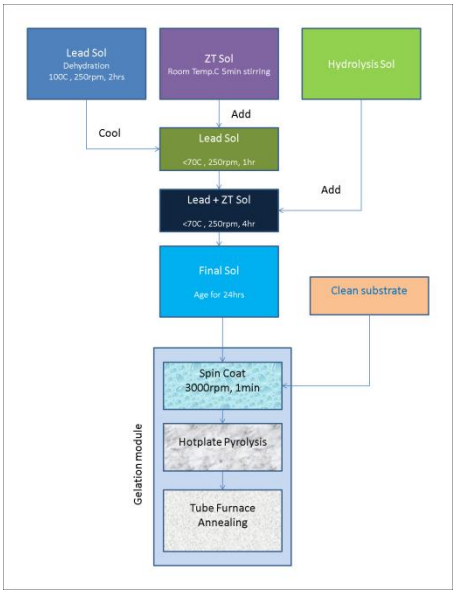

Figure 2.1 Sol-gel process flow

The lead sol comprises of lead acetate trihydrate 99.99% diluted in 2-methoxymethanol 99.9% solvent. The lead sol was dehydrated at 100^{o}C for 2hrs. The zirconium + titanium sol (henceforth referred to as ZT) was created by first mixing Zr (IV) propoxide 70% in 1-proponal solvent (1-propanol 99%) at room temperature. After a few minutes of mixing, Ti (IV) propoxide 97% was added, mixed, followed by addition of acetyl acetonate, a chelating agent. The third sol was the hydrolysis sol comprising of the deionized water (> 18 Mohms) with 1-propanol 99% in equal ratios. After the lead sol has cooled down to room temperature, the ZT sol was added to it while stirring at 250rpm. After one hour of stirring, the hydrolysis sol was added slowly and after four more hours of stirring, the clear sol was aged for twenty four hours. The aged sol was then spun

onto platinized silicon substrates (Pt/Ti/SiO_2/Si) at 3500rpm for 30 sec. After spin coating, the thin films were pyrolyzed and annealed as per table below. Table 2.1 depicts a 2^4 full factorial screening experiment in the four factors (TCP) – pyrolysis time, pyrolysis temperature, annealing time and annealing temperature. Pyrolysis was conducted on a hot plate whilst annealing was accomplished in a vertical furnace exposed to ambient air. The resultant thin film thickness was in the range of 65-85nm.

Table 2.1 2-factorial statistical designed screening experiment to initiate PZT sol-gel texturing study

Name	***Units***	***Type***	***Low Actual***	***High Actual***
Pyrolysis temperature	^oC	Numeric	250	350
Pyrolysis time	min.	Numeric	1.5	4.5
Annealing temperature	^oC	Numeric	650	750
Annealing time	min.	Numeric	10	20

The gelation process of pyrolysis and perovskite crystallization process of annealing were optimized for 3 different textures ((100), (110) and (111)) of PZT thin films on platinized silicon substrates. Subsequent detailed experimentation included the investigation on thermal budget to identify all the regions on operating space and the data from these samples was used to rigorously fill the TTT diagram for three different crystalline orientations. For the screening experiments, platinized silicon substrates from Nova Electronic Materials, FlowerMound, TX, were used and to develop the TTT diagrams followed by more detailed experiments, substrates from Inostek, South Korea, were utilized. The former had a micron of Pt over a Ti glue layer on SiO_2/ Si whilst the latter had the configuration of 150nm Pt/10nm Ti/300nm SiO_2/Si. X-ray diffraction was used to measure the orientation of the thin films. The X-ray peak heights

(alternatively FWHM can be employed too) were measured and normalized. Design Expert software was used to generate and analyze the statistically designed screening experiments (SDE). JMP and R software's were used in the mathematical modeling of the TTT data.

Results and Discussion

A SDE of 17 (2^4+ 1 center point) runs was designed and conducted on the platinized Si substrates. These substrates had a micron thick Pt on Ti/SiO2/Si. XRD pattern was collected on 17 samples and the heights of peaks for (100) at $2\theta = 22^{\circ}$, (110) at $2\theta = 31^{\circ}$ and (111) at $2\theta = 38^{\circ}$ was measured from the type of graph shown in figure below. The normalized XRD peak heights for (100), (110) and (111) orientations was then used as the response of the SDE and an ANOVA (Analysis of Variance) was conducted. In the experimental range explored, ANOVA shows that annealing temperature and time effects (C, D and interaction CD) are more significant than the pyrolysis conditions (A, B and interaction AB) and the interaction between the annealing and pyrolysis effects (AC, AD, BC, etc). This is clearly evident in the half normal probability plots of the Effects (measure of the process variable's influence on the response) shown in Figure 2..

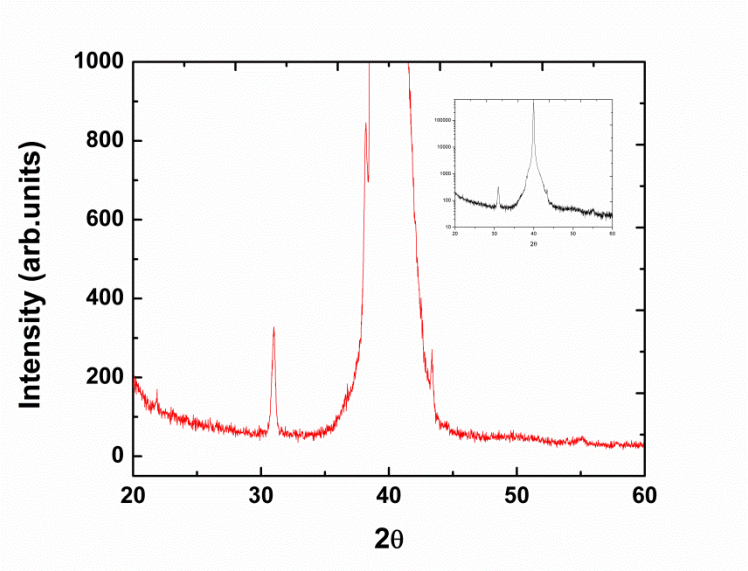

Figure 2.2 A typical XRD plot from a PZT sol-gel thin film showing small (100), substantial (110) and a large (111) shoulder (inset shows the whole spectrum on log scale). The film was deposited on a platinized silicon substrate

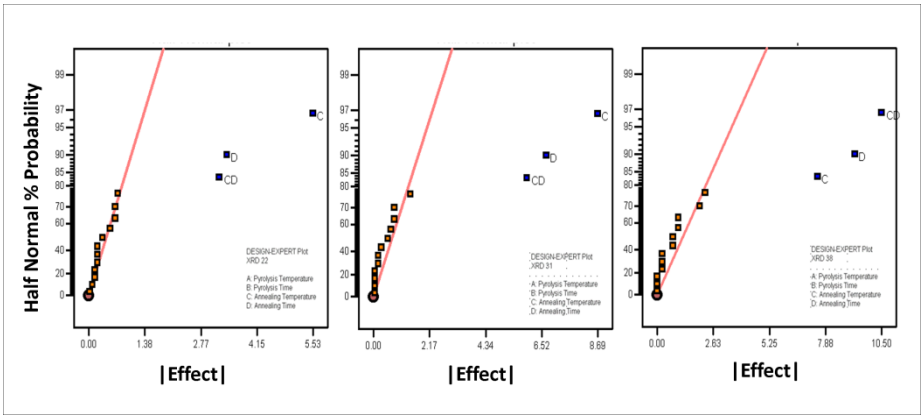

Figure 2.3 Half Normal probability plots of XRD responses – (100), (110) and (111) peak heights

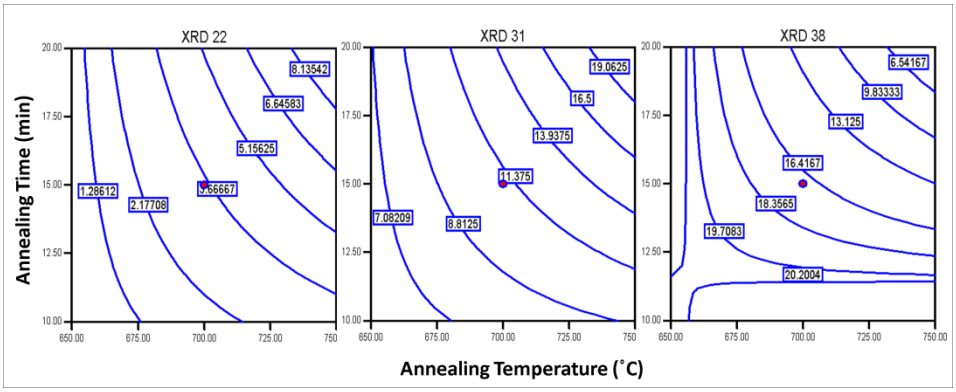

Figure 2.4 Contour plots showing increasing trends with respect to annealing conditions for (100) at 2θ = 22˚, (110) at 2θ = 31˚ and (111) at 2θ = 38; the Pyrolysis conditions were 300 ^{o}C and 3 min

The resultant regression models generated the contour plots shown in figure above. We find that higher annealing time and temperature yields higher desired peak (100) and decreases the undesired peak (111). However, the (110) peak also increases in this process regime. These XRD peaks were independent of pyrolysis time and temperature in the range explored. Also below 700^{o}C, longer annealing times will make the peak height independent of annealing time. Using this information, further extensive exploration of the sol-gel thermal budget operating space yielded the TTT diagrams shown in figure below. This diagram is similar to that developed by Chen and Chen[8, 9] except that their main process variables were pyrolysis temperature and time and they had maintained annealing temperature and time constant. It can be seen that films with pyrolysis at 300^{o}C for 3 min were textured in (100) direction until ~ 750^{o}C annealing temperature, after which they start showing random orientation (labeled ‘not textured’ in figure below). This trend is a confirmation of the contour plot trends observed in the screening experiments. With increase in annealing temperature and time, the (100) and (110) orientations increases whilst (111) orientation decreases and at > 750^{o}C, all three orientation co-exist and so

the film was not textured. On the other hand, the films pyrolyzed at lower temperatures and for shorter times are textured in (100) or (110) (for no pyrolysis) direction until a certain threshold temperature and thereafter in (111) direction and that too is independent of annealing time. Ternary diagrams show the frequency of the orientations obtained for each pyrolysis binned as per the ranges in annealing temperature (see figure below) and annealing time (see figure below).

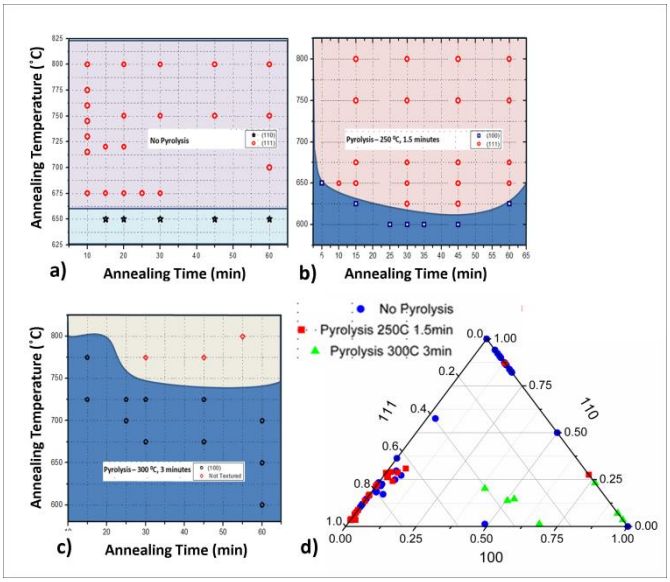

Figure 2.5 Temperature-Time-Transformation diagrams of PZT sol-gel thin films pyrolyzed at a) No pyrolysis b) 250˚C, 1.5 minutes, c) 300˚C, 3 minutes and d) the ternary plot of all the data

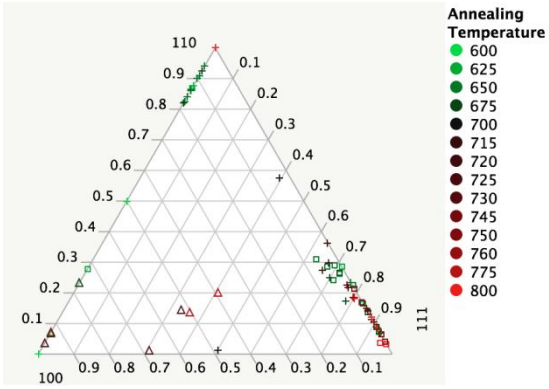

Figure 2.6 Observed data by Pyrolysis coded by Annealing Temperature

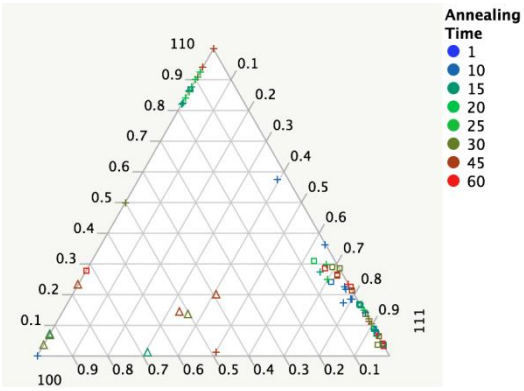

Figure 2.7 Observed data by Pyrolysis coded by Annealing Time

The data utilized to create the TTT diagrams was analyzed using the JMP statistical software and the quadratic fits are shown in Figure 2.8. Despite moderate R^2 values (reported in figure description), the predictability of the quadratic models was found to be poor. A good hint towards this unpredictability can be witnessed in the portion of points that do not trend with the surface plots. We omitted to include the proportionality between the crystalline orientations (the

3 box plots at the apex of Figure 2.9) which can explain this difference. In the left bottom of this figure, one can also notice the large spread in the response data (i.e. the lack of a linear or higher order trend) with respect to the processing variables.

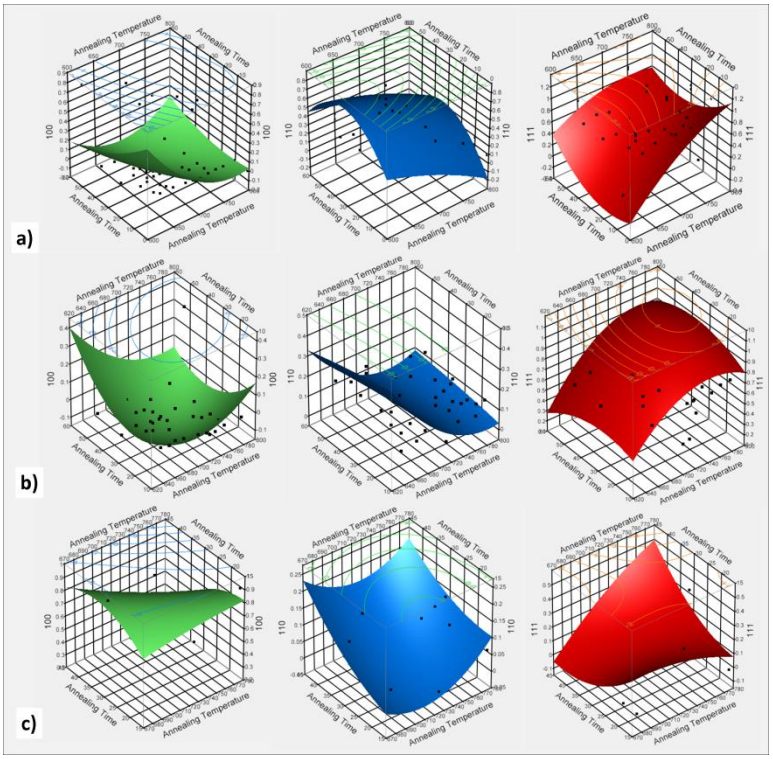

Figure 2.8 JMP Contour plots of PZT sol-gel thin films pyrolyzed at a) No Pyrolysis – (100) with R^2 = 0.662, (110) with R^2 = 0.381 and (111) with R^2 = 0.644, b) 250˚C 1.5min Pyrolysis – (100) with R^2 = 0.495, (110) with R^2 = 0.451 and (111) with R^2 = 0.527and at c) 300˚C, 3min pyrolysis – (100) with R^2 = 0.722, (110) with R^2 = 0.961 and (111) with R^2 = 0.694

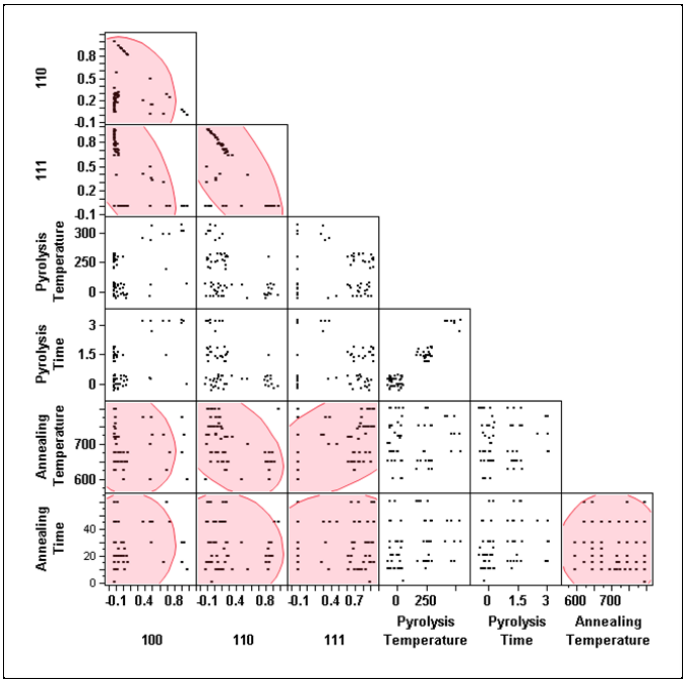

Figure 2.9 JMP Scatter plot matrix of the responses (XRD peak data) vs. the factors - pyrolysis and annealing conditions

Multiple regression takes a single response (or several separately ones at a time) and models its relationship to multiple independent factors. The quadratic model, which is a multiple regression, was inadequate to explain correlated response data evocative of XRD pattern data. To model this joint relationship, a multivariate regression approach had to be employed. Multivariate regression simultaneously relates several responses to each other and to multiple independent factors. As mentioned earlier, the XRD peak data was normalized and so the three responses add up to one and therefore are inherently related (i.e. not independent). Therefore we must model them simultaneously. As pyrolysis conditions were lumped into three pairs of temperature and time combinations in the TTT experimentation, each pair was considered as a single categorical

process variable. The other two process variables were considered as either categorical or continuous variable in the regression.

After separate independent regressions (the aforementioned quadratic regression), two other methods of regression, multinomial logistic[12] and log ratio multivariate[13], were evaluated. For multinomial regression, we convert the normalized XRD data into counts. Bearing in mind that the normalized data are the observed proportions of crystalline orientations in each film or sample, then the 100 points or counts can be the sum total of all three crystalline orientations. For example, if we observed percentages of 5%, 10%, and 85%, we would assign counts of 5, 10, and 85 respectively. Now we treat this transformed data as observed counts from a multivariate binomial (multinomial) distribution. Our multinomial distribution is described by three parameters representing the true unordered proportions in our mixture: p[100]; p[110]; p[111] with p[100] + p[110] + p[111] = 1. In order to perform regression to model these parameters we use

$$\boldsymbol{Lin[110] = \ln\left(\frac{p_{[110]}}{p_{[111]}}\right) = X\beta}$$

(1) below:

$$\boldsymbol{Lin[100] = \ln\left(\frac{p_{[100]}}{p_{[111]}}\right) = X\alpha}$$

$$\boldsymbol{Lin[110] = \ln\left(\frac{p_{[110]}}{p_{[111]}}\right) = X\beta}$$

(1)

where X is the covariate matrix from pyrolysis, annealing time, and annealing temperature, α and β are the regression coefficients that we estimated using maximum likelihood methods. Together Xα and Xβ are called linear predictors. After modeling Lin[100] and Lin[110], p[100], p[110] and p[111] can be recovered from (2):

$$p_{[100]} = (1 + \exp(-Lin[100]) + \exp(Lin[110] - Lin[100]))^{-1}$$

$$p_{[110]} = (1 + \exp(-Lin[110]) + \exp(Lin[100] - Lin[110]))^{-1}$$

$$p_{[111]} = (1 + \exp(Lin[100]) + \exp(Lin[110]))^{-1}$$

(2)

The main concept here is that the data are counts from a multinomial distribution and the unknown parameters are proportions. The linear predictors are the ratio of probabilities of occurrence of each orientation in a particular thin film sample at the stipulated thermal conditions. The second method evaluated was Log Ratio regression for which multivariate normal regression of the log of the ratios of the normalized XRD peak data was performed. As in the multinomial case, this method also preserves the constraint that the data must sum to one. The log ratio strategy as described by Aitchison[13] transforms similar to that in multinomial regression. For the log ratio technique, we transform the data (100), (110) and (111) through (3):

$$LR1 = \ln\left(\frac{[100]}{[111]}\right)$$

$$LR2 = \ln\left(\frac{[110]}{[111]}\right)$$

(3)

Thus the new data are LR1 and LR2 with mean vector ($\mu 1$; $\mu 2$) and covariance matrix S. In order to perform regression we use (4):

$$\mu_1 = X\alpha$$

$$\mu_2 = X\beta$$

(4)

After modeling $\mu 1$ and $\mu 2$, we can recover the fitted (predicted) concentrations with (5):

$$\widehat{[100]} = (1 + \exp(-LR1) + \exp(LR2 - LR1))^{-1}$$

$$\widehat{[110]} = (1 + \exp(-LR2) + \exp(LR1 - LR2))^{-1}$$

$$[\widehat{111}] = (1 + \exp(LR1) + \exp(LR2))^{-1}$$

(5)

Therefore, in this case, the main concept is that the data is in LR1 and LR2 and they are normally distributed with parameters mean and covariance matrix.

The purpose of regression is to find α and β so that Xα and Xβ best describe or fit the data. Both the multinomial and the log-ratio regression will produce estimates for α and β. The columns of the X matrix can be either categorical or continuous predictors. Categorical variables such as "High", "Medium", "Low" or "Red", "Green", "Blue" describe distinct states of classes. Continuous variables such as "Length", "Age", and "Weight" are measured on a continuous scale. Often when we have continuous regressors such as temperature, we can either use continuous values or discretize them by binning them into categories such as "High", "Medium", and “Low". The benefit of using continuous regressors over categories is reduction in number of terms, which means savings in efficiency or fewer samples needed for good model fitting. The benefit of using categories is that they are more flexible and tend to fit better when a non-linear relationship exists. As mentioned previously, we will always use pyrolysis as a categorical variable with three settings. Annealing time and temperature can be used as either continuous or categorical variables, so we will fit both continuous and categorical models and compare their characteristics.

In the Continuous model, we will use pyrolysis “P” (P1, P2, P3) as a categorical variable and annealing time (Tm) and annealing temperature (Tp) as continuous variables. Our linear predictors Xα and Xβ are now:

$$\mathbf{X\alpha} = \alpha_0 + \alpha_P \mathbf{P} + \alpha_{Tm} \mathbf{Tm} + \alpha_{P*Tm} \mathbf{P} * \mathbf{Tm} + \alpha_{P*Tp} \mathbf{P} * \mathbf{Tp} + \alpha_{Tp} \mathbf{Tp} + \alpha_{Tm*Tp} \mathbf{Tm} * \mathbf{Tp} + \alpha_{P*Tm*Tp} \mathbf{P} * \mathbf{Tm} * \mathbf{Tp}$$

$$\mathbf{X\beta} = \beta_0 + \beta_P \mathbf{P} + \beta_{Tm} \mathbf{Tm} + \beta_{P*Tm} \mathbf{P} * \mathbf{Tm} + \beta_{P*Tp} \mathbf{P} * \mathbf{Tp} + \beta_{Tp} \mathbf{Tp} + \beta_{Tm*Tp} \mathbf{Tm} * \mathbf{Tp} + \beta_{P*Tm*Tp} \mathbf{P} * \mathbf{Tm} * \mathbf{Tp}$$

(6)

Notice that "P" and all α's and β's associated with "P" change depending on whether P = P1, P2, and P3. Since pyrolysis (P) can take on three values, we are fitting three models at the same time.

$$\mathbf{X\alpha} = \alpha_0 + \alpha_P \mathbf{P} + \alpha_{Tm} \mathbf{Tm} + \alpha_{P*Tm} \mathbf{P} * \mathbf{Tm} + \alpha_{P*Tp} \mathbf{P} * \mathbf{Tp} + \alpha_{Tp} \mathbf{Tp}$$

$$\mathbf{X\beta} = \beta_0 + \beta_P \mathbf{P} + \beta_{Tm} \mathbf{Tm} + \beta_{P*Tm} \mathbf{P} * \mathbf{Tm} + \beta_{P*Tp} \mathbf{P} * \mathbf{Tp} + \beta_{Tp} \mathbf{Tp}$$

(7)

In the Categorical Model we treat Tm and Tp as categories. Our linear predictors' form remains the same but there are fewer interaction terms (Eq. ((7)). In this case, we fit a separate model for each P, Tm, and Tp combination. If we had 5 levels of Tm, 5 levels of Tp, and 3 levels for P, we would have 75 models that we estimate at the same time.

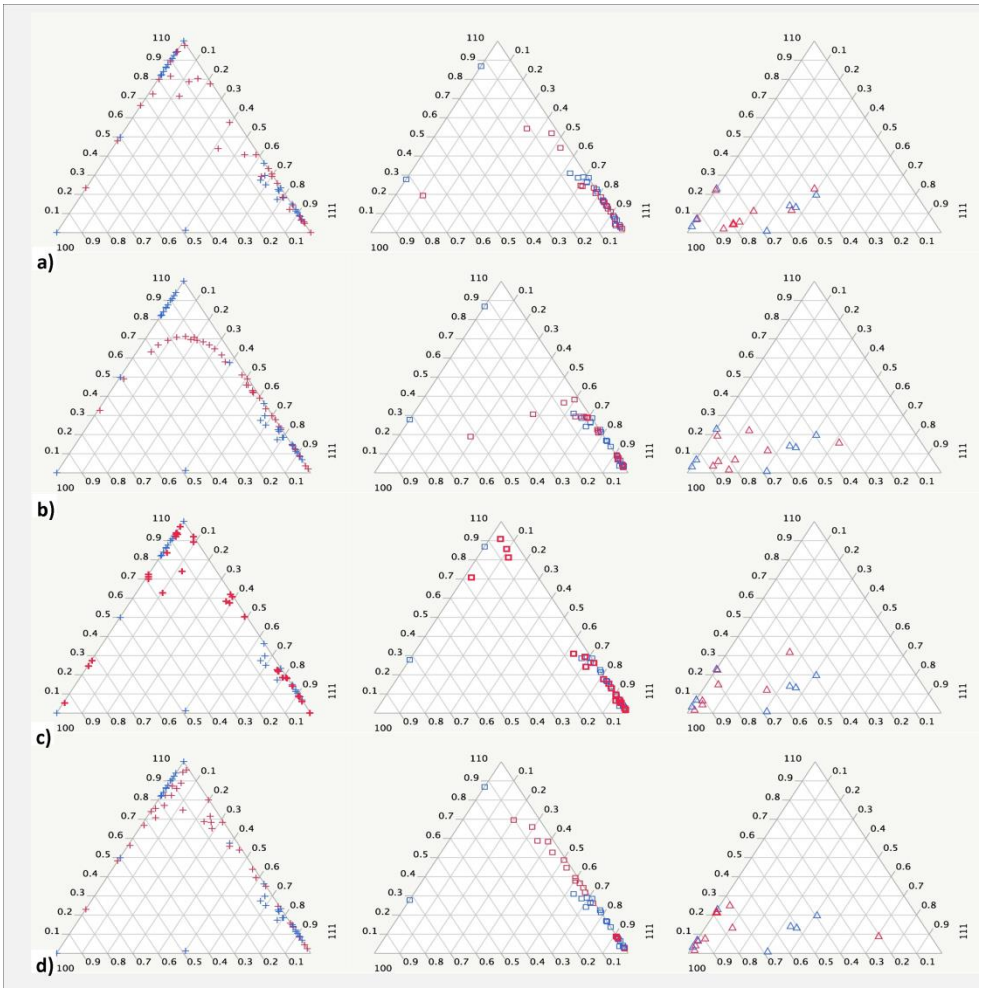

Figure 2.10 Actual vs. Predicted for a) Multinomial Categorical b) Multinomial Continuous c) Log-Ratio Categorical and d) Log-Ratio Continuous (blue-observed, red-fitted) models

We used continuous and categorical models of both the multinomial and the log ratio methods to fit the data. We then compared them to the observed data and the saturated categorical model (which is essentially the same or a point by point fit). From Figure 2.(a) – (d) we see that the categorical models have better fits than the continuous ones, suggesting a possible nonlinear relationship in the predictor. Also, it seems that the multinomial model has a better fit than the log ratio model. This is confirmed when plotting observed versus fitted data for each (100), (110), (111) orientations separately in Figure 2.(a) – (c). Besides the saturated model, which is

not a realistic model (unless we have replicates), the categorical model with the multinomial data (2nd from the left) gives the closest fit to the one-to-one line for the observed and fitted values.

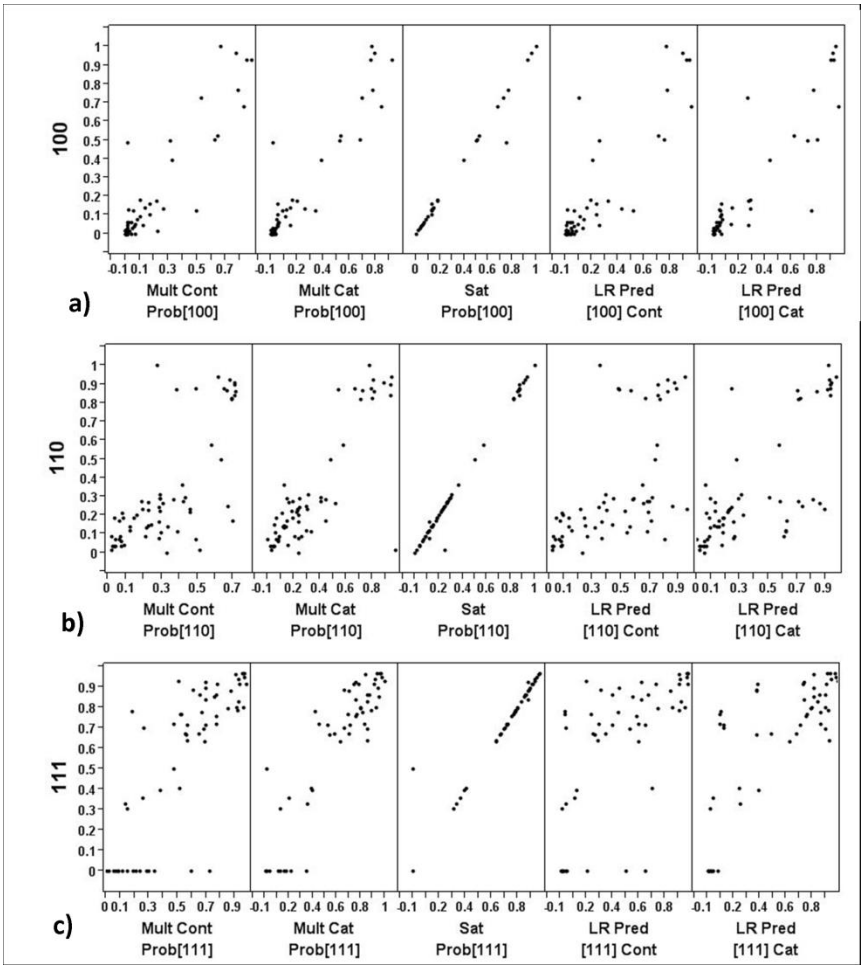

Figure 2.11 Actual vs. Fitted for a) (100),: b) ([110) and c) (111)

In using the multinomial model with categorical factors for prediction, the choice of annealing temperature and time is restricted to that used in the original model whilst with continuous factors, any annealing temperature and time value (but within the range used in the model) is permitted. To elucidate (refer to Figure 2. and Figure 2.), with the continuous model one can

predict the response for an annealing temperature of 685˚C and 22 min but for the categorical model (where discretized fixed values of the factors are used), we have to use an annealing temperature and time that have been used in the original regression (say, 675˚C or 700˚C and 20 or 25min but not necessarily the same original combination of the two factors).

Table 2.2 XRD normalized data vs. model predictions for 4 different samples

Sample	*Pyrolysis & Annealing Conditions*	*XRD peak*	*Actual*	*Multinomial Categorical Model*	*Multinomial Continuous Model*	*Log-Ratio Categorical Model*	*Log-Ratio Continuous Model*
SG1	300C 3min	(100)	0.88	0.924	0.878	0.928	0.952
	675C 30min	(110)	0.12	0.076	0.0417	0.0721	0.0428
		(111)	0	4.29E-06	0.08	0.0003	0.0056
SG2	300C 3min	(100)	0.896	0.924	0.878	0.928	0.952
	675C 30min	(110)	0.104	0.076	0.0417	0.0721	0.0428
		(111)	0	4.29E-06	0.08	0.0003	0.0056
RV1	300C 3min	(100)	0.91	0.924	0.878	0.928	0.952
	675C 30min	(110)	0.09	0.076	0.0417	0.0721	0.0428
		(111)	0	4.29E-06	0.08	0.0003	0.0056
RV2	250C 1.5min	(100)	0.0042	0	0	0.0008	0.0007
	800C 30min	(110)	0.083	0.022	0.034	0.0172	0.0273
		(111)	0.875	0.978	0.966	0.982	0.972

For final experimental verification, we created 4 samples, SG1, SG2, RV1 and RV2 (see table above) where SG and RV refers to PZT sol created up by 2 different operators but SG1, SG2 and RV1 were processed at the same pyrolysis and annealing condition. From Figure 2., we see that the predictability using mutltinomial categorical fit is the best amongst the four models attempted. The continuous models over predict the lowest rank response (i.e. they are not very good at predicting a zero response). The Log ratio models consistently over predict the

predominant orientation (i.e. the largest response). Based on these results, we believe this mathematical formulation of TTT diagram allows the prediction of the predominant orientation and the ranking of each orientation of interest (i.e. the orientations used in the XRD data modeling). This regressive modeling can be applied to more than three peaks of an XRD pattern and therefore, for 'n' number of peaks will lead to 'n' proportions and (n-1) equations similar to Eq. ((1). In addition, such type of modeling can be undertaken for XRD patterns from any (i.e. non-PZT) thin film or bulk ceramics (including PZT). Understandably, this mathematical approach is only as accurate as the methodology employed in calculating the XRD peak heights.

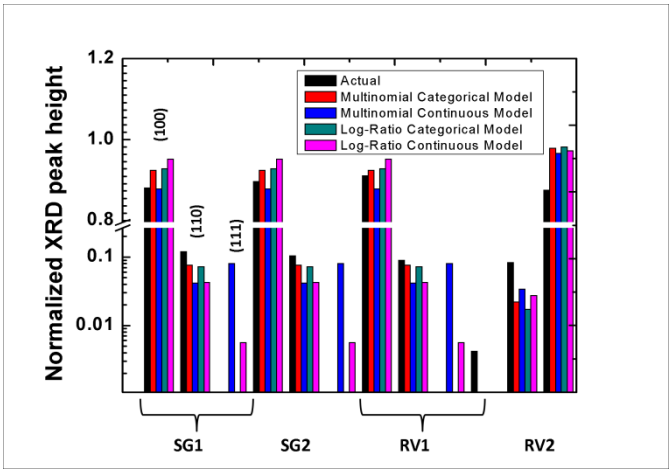

Figure 2.12 Comparison of prediction results for 4 sol-gel samples

Conclusion

In summary, we developed a mathematical model to refine the typical temperature-time-transformation (TTT) diagrams by quantitatively describing both the predominant phase and any secondary phases. Utilizing data from the two-step thermal treatments (pyrolysis and annealing) of a PZT sol-gel or chemical solution deposition process, different regression schemes, namely, multiple linear, multinomial and multivariate, were explored to derive predictor models for the

level of (100), (110) and (111) crystallinity in a thin film sample. The best validation of experimental data was obtained with multinomial regression. We have demonstrated the simplicity and efficacy of this methodology for every day laboratory use and expect extendibility to non thin film systems. In doing so, we have also taken out some of the specificity, like operator induced variability, that is usually observed in such experimentation.

References

[1] Kuwata J, Uchino K, Nomura S. Phase transitions in the Pb (Zn1/3Nb2/3) O3-PbTiO3 system. Ferroelectrics 1981;37:579.

[2] Kuwata J, Uchino K, Nomura S. Dielectric and piezoelectric properties of 0.91 Pb (Zn1/3Nb2/3) O3-0.09 PbTiO3 single crystals. Japanese journal of applied physics 1982;21:1298.

[3] Park S-E, Shrout TR. Ultrahigh strain and piezoelectric behavior in relaxor based ferroelectric single crystals. Journal of applied physics 1997;82:1804.

[4] Park S-E, Shrout TR. Characteristics of relaxor-based piezoelectric single crystals for ultrasonic transducers. IEEE transactions on ultrasonics, ferroelectrics, and frequency control 1997;44:1140.

[5] Fu H, Cohen RE. Polarization rotation mechanism for ultrahigh electromechanical response in single-crystal piezoelectrics. Nature (London) 2000;403:281.

[6] Du X-h, Zheng J, Belegundu U, Uchino K. Crystal orientation dependence of piezoelectric properties of lead zirconate titanate near the morphotropic phase boundary. Applied physics letters 1998;72:2421.

[7] Norga GJ, Fe L. Orientation selection in Sol-gel derived PZT thin films. Mat. Res. Soc. Symp. Proc. 2001;655:CC9.1.1.

[8] Chen S-Y, Chen I-W. Temperature-Time Texture Transition of Pb(Zr(1-x)Ti(x))O3 Thin Films: II, Heat Treatment and Compositional Effects. Journal of American Ceramic Society 1994;77:2337.

[9] Chen S-Y, Chen I-W. Temperature-Time Texture Transition of Pb(Zr(1-x)Ti(x))O3 Thin Films: I, Role of Pb-rich Intermediate Phases. Journal of American Ceramic Society 1994;77:2332.

[10] Huang Z, Zhang Q, Whatmore RW. The rolo of an intermetallic phase on the crystallization of lead zirconate titanate in sol-gel process. Journal of Materials Science Letters 1998;17:1157.

[11] Park CS, Kim SW, Park GT, Choi JJ, Kim HE. Orientation control of lead zirconate titanate film by combination of sol-gel and sputtering deposition. Journal of materials research 2005;20:243.

[12] Agresti A. Categorical Data Analysis: Wiley-Interscience, 2002.

[13] Aitchison J. The Statistical Analysis of Compositional Data (Monographs on Statistics and Applied Probability): Springer, 1986.

Chapter 3

Ellipsometric Characterization of Multi-component Thin Films: Determination of Elemental Content from Optical Dispersion

Ronnie Varghese,[1*] Greg Pribil,[2] W. T. Reynolds Jr,[3] and Shashank Priya[1]

[1]Center for Energy Harvesting Materials and Systems (CEHMS), Bio-Inspired Materials and Devices Laboratory (BMDL), Virginia Tech, Blacksburg, VA 24061, USA
[2]J.A. Woollam. Co. Inc, Lincoln, NE 68508, USA
[3]Materials Science and Engineering Department, Virginia Tech, Blacksburg, VA 24061, USA

Abstract

This paper provides the correlation between the composition of a given thin film to its optical dispersion properties. Gladstone-Dale (G-D) relationships have been used in optical mineralogy to relate density of crystalline compounds to their average refractive index. We purport to use a 'reverse' G-D approach and determine the composition of multi-component thin films from their optical properties. As a model system, we focus on complex perovskite ferroelectric thin film and apply the derived relationships to determine the stoichiometry. The wavelength dispersion of refractive index and extinction coefficient of various Pb(Zr,Ti)O3 (PZT) thin films was measured using Variable Angle Spectroscopic Ellipsometry (VASE). Elemental compositions were measured using Energy Dispersive X-ray analysis (EDX) and Electron Probe Micro Analysis (EPMA). Wemple-DiDomenico, Jackson-Amer, Tauc and Urbach optical relationships and related parameters were used to extract correlations to elemental content. Both theoretical and semi-empirical approaches to calculate the electronic polarizability of PZT were employed

and their variation with elemental content was computed. Perovskite tolerance and octahedral factors were also analyzed against the optical and polarizability parameters. Lastly, these factors and relationships were combined to realize a model for predicting the elemental content of a thin film system.

Keywords: Thin films; Optical properties; Refractive index; Optical dispersion; Absorption coefficient

Introduction

Many attempts have been made to empirically or theoretically derive the correlation between optical absorption, mass density and electronic properties of materials. Gladstone and Dale[1] (G-D) provided the empirical correlation between the average index of refraction 'n' and mass density ρ_m of a mixture as:

$$\frac{(n-1)}{\rho_m} = \sum_i k_i w_i \qquad (1)$$

where k_i is the refractive coefficient and w_i is the weight fraction of component 'i' making up the solution. The common applications of G-D relationships are: (l) the calculation of the refractive index 'n' from measured density and the specific refractive energy derived from the chemical analysis; and (2) the calculation of density from the mean refractive index and the specific refractive energy. Specific refractive energy refers to the refractive index of any substance minus unity, divided by the density. The G-D relationship defines the optical properties of a solid solution as the sum of the optical properties of its comprising oxides. An analogous relationship is the Beer-Lambert's law which is used to describe the relationship between light absorption and the concentration of an irradiated sample. One drawback of the G-D relationship is that the

refractive coefficients are empirically derived for a certain optical spectrum or line. In many cases, the relationship is only valid for n > 1.4[2],[3]. Also in the G-D relation, specific refractivity of each component assumes unrealistically that the effect of each component is separate and independent of the others.

To illustrate, on applying the G-D relationship to $Pb_{1.1}(Zr_{0.52}Ti_{0.48}O_3)$ (PZT) thin film and using the refractive coefficients for the constituent oxides derived by Larsen[4] with the stoichiometry and molecular weights we get:

$$\frac{(n-1)}{\rho_m} = \frac{mw_{PbO} \times mole\ fraction_{PbO} \times 0.15 + mw_{ZrO2} \times mole\ fraction_{ZrO2} \times 0.20}{mw_{PbO} \times mole\ fraction_{PbO} + mw_{ZrO2} \times mole\ fraction_{ZrO2} + mw_{TiO2} \times mole\ fraction_{TiO2}} + \frac{mw_{TiO2} \times mole\ fraction_{TiO2} \times 0.40}{mw_{PbO} \times mole\ fraction_{PbO} + mw_{ZrO2} \times mole\ fraction_{ZrO2} + mw_{TiO2} \times mole\ fraction_{TiO2}} \quad (2)$$

For PZT,ρ_m~7.8gm/cc and so, n=2.457. From the above equation, we realize that by changing the stoichiometry or the concentration one can alter the average refractive index. Conversely, as seen from the above equation, the change in average refractive index will not uniquely identify a particular concentration. Inspired by the literature on the G-D relationship, we decided to investigate the possibility of developing a reverse relationship whereby optical properties could be used to determine the composition. Particularly, can the optical properties of a solid solution provide a measure of the concentration or composition of its constituents in complex oxides?

To illustrate the approach, we selected PZT due to its huge industrial relevance. PZT films have been studied for ferroelectric random access memory that can provide nonvolatile memory operation with fast writing time while reducing the power requirement. PZT films are also being pursued as gate dielectric in ferroelectric memory field-effect transistor providing a

nondestructive readout operation with high density. La-modified PZT films are candidate materials for the electro-optic modulators and light activated actuators. Further, doped PZT films near morphotropic phase boundary form the part of vast number of actuation and sensing devices.

Teertstra[5] invoked Newtonian particle theory of light to explain the G-D relationship and postulated that incident light (as a particle) is affected by inter-atomic bonding (i.e. non-linear path through material). He proposed a new coefficient, 'specific ionic refractivity', which is characteristic of each elemental ion in a material. For each atom at a particular crystallographic site, this coefficient can be calculated from the physical properties of its ion in the structure [5-7]. For a specific structural formula of a crystalline material, Teertstra[7] suggested that the weight fraction of its components can be determined by iteration from the calculated (from existing empirical data of similar compounds) ionic G-D coefficients of the constituent elements, measured average refractive index and unit cell parameters from crystallographic data (i.e. *a-priori* knowledge of site occupancies; not possible for amorphous or polycrystalline material). The values derived under so many constraints must also meet the boundary condition of measured density and be valid across a wide incident wavelength range. These ionic coefficients cannot be assumed to remain constant in different compounds – for example, Pb^{2+} coefficients will be different in $PbTiO_3$ vs. $PbZrO_3$. Multivalent states of the same ion will present challenges in analysis as the substitution may not be site specific.

In contrast, we utilized the dielectric polarization effect of an electromagnetic light wave traversing a medium. The optical dispersion (i.e. the variation of refractive index and extinction coefficient with incident light wavelength or energy) of a material is inherently related to its concentration, valency or coordination of its constituents, band tails and gap states. An increase

in refractive index can occur by the increase in ionic charge or valency, increased atomic number or decreased atomic or ionic radii of a cation and covalently bonded anion[5]. Therefore, we can expect that a variation in elemental composition will affect the broad spectrum (including optical energies > band gap) of an analyte[8]. The models thus developed can be used to predict the composition of a multi-component compound irrespective of its level of crystallinity.

Experimental Details

Material Characterization

Unlike DC sputtering of conductive films, non-conductive PZT films require RF power sources for plasma generation. $Pb_{1.1}(Zr_xTi_{1-x})O_3$ target for x = 0.52 with 10% excess Pb to compensate for Pb loss during post deposition annealing, was prepared by mixed oxide method. RF sputtering plasma deposition (Figure 3.1(a)) involves Argon ion bombardment on the PZT target and subsequent deposition of the sputtered PZT material onto a grounded or biased substrate. The sputter target concentrations based on the stoichiometry were Pb at 21.57%, Zr at 10.20%, Ti at 9.41% and O at 58.82%. On the Aja International (Scituate, MA, USA) RF sputtering system, the process variables were argon and oxygen flows, chamber pressure, RF power (DC Bias), working distance, temperature, rotation speed and substrate bias. The deposition time was fixed at 30 minutes. RF sputter deposition operating space was explored using statistical Design of Experiments (DOE using DesignExpert™ software) and trends and ANOVA (Analysis of Variance) models were formulated. After measurement of the dispersion of refractive index and extinction coefficient using Variable Angle Spectroscopic Ellipsometry (VASE), the composition of these films was measured using either Energy Dispersive X-ray analysis (EDX) or Electron Probe Micro Analysis (EPMA) or both. In the first screening experiment (Figure

3.1(b)), we combined O_2 and Ar flow factors by varying O_2 flow in a fixed Ar flow. We also fixed the working distance and rotation speed and fixed substrate temperature at two settings of room temperature and 100^{o}C. In doing so, we reduced the experiment to 2^4 = 16 runs + 2 temperature blocks + 2 center runs per block = a total of 18 experiments. These runs resulted in PZT thin films in the range of 30-130nm over a 150nm Pt/10nm Ti/300nm SiO2/500mm Si substrate (referred as 'platinized Si') and pristine Si substrate. No further annealing was undertaken so as to prevent Pb loss from film and minimize substrate and other interfacial effects on film properties. A 2nd DOE with process variables of RF power, RF bias and O_2 flow were used to further narrow down the processing space. This DOE had process pressure fixed at 7 mTorr, Ar flow at 12 sccm, working distance at 25 cm and rotation speed at 40rpm as these were the recommended conditions for the highest deposition rate with the least optical absorption and a composition closest to stoichiometry as per the 1st DOE ANOVA models.

Top down elemental characterization of thin films by EDX or EPMA, assays the underlying substrate too (interaction volume has 2-10μm depth and dependent beam energy) and frequently this signal overwhelms the detector and interacts with the signal from the film. EDX spectral analysis on platinized-Si posed problem with the Zr primary peak buried under the substrate Pt primary peak (Figure 3.1(c)). On confirming minimal differences in elemental contents between the different substrates, we used Si substrate based samples for the elemental characterization. To minimize the substrate effects in EDX, the SEM voltage was restricted to 8 keV at a sample current of 25 nA. EPMA was equipped with 4 tunable wavelength dispersive spectrometers. PET analyzing crystal was used for Zr, Pb and Ti whilst TAP for Si. The standards were Pyromorphite for Pb, Ti-6 for Ti Ka, and Zr-6 for Zr and a Si wafer for Si.

Interestingly, Ti and Zr concentrations were found to be linearly correlated which could be attributed to their equivalent sputtering yields.

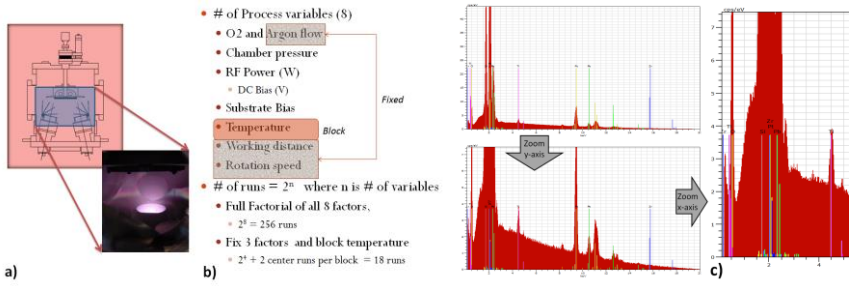

Figure 3.1 (a) RF sputter configuration for PZT thin films, (b) PZT RF Sputter process variables, and (c) EDX of PZT on platinized Si – on zooming in, Zr peak is buried under Pt peak

As deposited PZT RF thin films were mostly amorphous - which is expected as the crystallization temperature is generally above 600^{o}C (confirmed by X-ray diffraction).

Optical Characterization

Optical measurements were performed on a J.A.Woollam VASE in rotating analyzer mode in the wavelength range of 300-800nm (4.13-1.55eV) at incidence angles of 65˚, 70˚ and 75˚. Ellipsometry measures two values Ψ and Δ that expresses the amplitude ratio and phase difference between the ‘s’ and ‘p’ polarizations of the reflected light from the sample. A general oscillator layer (hereafter, referred to as ‘Genosc’) model was employed to fit the ellipsometric data of each as-deposited thin film. The Genosc layer models the dielectric function of the PZT thin film as a linear summation of the real and complex oscillators (each a function of wavelength or photon energy)[9]. The PZT Genosc included a summation of two Gaussian oscillators and an offset to the real part of the dielectric function ε_{∞}:

$$\varepsilon(E)=\varepsilon_1(E)+\ i\varepsilon_2(E)=\text{Offset}+\ \text{Gaussians}(\text{E},\ \text{A1},\ \text{E1},\ \text{B1})+\ \text{Gaussians}(\text{E},\ \text{A2},\ \text{E2},\ \text{B2})\quad(3)$$

For a Gaussian Oscillator model[9], the above equation simplifies to the Gaussians terms for ε_2 with a Kramer-Kronig consistent profile for ε_1.

$$\varepsilon_2(E)=A_n e^{-\left(\frac{E-E_n}{\sigma}\right)^2}-A_n e^{-\left(\frac{E+E_n}{\sigma}\right)^2}\ \text{where}\quad \sigma=\frac{B_n}{2\sqrt{\ln 2}}\qquad(4)$$

The fit parameters for the 'n'th Gaussian Oscillator are amplitude (A_n), center energy (E_n) and broadening (B_n) of the absorption peak. B_n equals the Full Width-Half-Maximum (FWHM) value of the Gaussian curve.

The constitutive relationships relating dielectric polarization and optical properties with respect to energy or wavelength are reproduced here from reference [10].The complex dielectric function is given as –

$$\varepsilon(E)=\varepsilon_1(E)-i\varepsilon_2(E)\ \ \textit{where}\ E=\frac{hc}{\lambda}$$

$$\varepsilon_1=n^2-k^2;\ \varepsilon_2=2nk\ \ ;\ \ a=\frac{4\pi}{\lambda}k\ ;\ n^*=n-ik=\sqrt{[\varepsilon_1-i\varepsilon_2]}\qquad(5)$$

The Kramer Kronig relationship link 'n' and 'k' (and therefore, ε_1 and ε_2) as:

$$n=1+\frac{2}{\pi}\int_0^\infty\frac{E'k(E')}{E'^2-E^2}dE'\ ;\ k=-\frac{2}{\pi}\int_0^\infty\frac{n(E')-1}{E'^2-E^2}dE'\qquad(6)$$

The optical band gap E_g of amorphous PZT thin films can be considered as a direct band gap transition between the valence band and the conduction band states (these states can include the band tails created by localized states at the absorption edge)[8]. The Tauc Gap E_g of amorphous

materials is derived from the following relationships between ε_2 and 'a' absorption coefficient vs. photon energy[11, 12].

$$\varepsilon_2 = B_{Tauc}\frac{\left(E-E_g\right)^2}{E^2}\ ;\ \ a = B_{Tauc}\left(E-E_g\right)^{1/2} \qquad (7)$$

B_{Tauc} is inversely related to refractive index. For direct band gap material, the optical band gap, E_g, is derived from the intercept on the x-axis of a tangent line from the curve generated by square of 'aE' vs. photon energy 'E' (often referred to as the Tauc plot; for indirect band gap material, the square root of 'aE' is used).

$$(aE)^2 \propto \left(E-E_g\right) \qquad (8)$$

Below this power law region of Tauc plot, there is an exponential region where the Urbach rule[11] applies and this area accounts for band tails or the localized states in the band gap. The inverse slope, Urbach width, E_u, determined from log(a) vs. photon energy plot is a measure of the disorder of the system producing the absorption tail in the Tauc plot.

$$a = a_0 e^{E/E_u} \qquad (9)$$

In the sub-gap region, as per Jackson and Amer[13], the area under the absorption 'a' vs. photon energy 'E' curve, is proportional to the localized defect states in the band gap. This proportional parameter is '$a_{s\text{-}g}$' and is given as:

$$a_{s-g} \propto a_o \int_{E}^{sub-E_g} \alpha\, dE \qquad (10)$$

In materials with a band gap, the refractive index at energies below the band gap is correlated to the absorption above the band gap as per the following version of the Kramer-Kronig relationship ($\mathcal{P}$ denotes the principal part)[14].

$$n^2 - 1 = \mathcal{P}\frac{2}{\pi}\int_{E_g}^{\infty}\frac{E' k(E')}{E'^2 - E^2}dE' \qquad (11)$$

Below the band gap the relationship evolves into the Wemple-DiDomenico dispersion model for refractive index given as:

$$n^2 - 1 = \frac{E_d E_o}{E_o^{\,2} - E^2} \qquad (12)$$

where E_d is the dispersion energy and is a measure of the optical transitions below the band gap and affected by the structural order of the material. Whilst E_o is the single oscillator energy that is correlated with the band gap and peak of the imaginary part of the complex permittivity or refractive index. These two parameters can be estimated from the plot of $1/(n^2-1)$ vs. E^2. E_d , is empirically found to be dependent on coordination number of the cation N_c , chemical valency of the anion Z_a, the effective number of valence electrons per anion N_e and finally β which has the value 0.26 +/-0.04 eV for ionic and 0.37 +/- 0.05 eV for covalent bonded atoms in the material.

$$E_d = \beta N_c Z_a N_e \qquad (13)$$

Results

Due to the variation in optical constants across the large number of samples (and process conditions), not all samples required the use of all the fit parameters (A1, B1, E1, A2, B2, E2 for 2 Gaussians and an e1 offset) of Equation 3. For some samples, 2 Gaussian oscillators were

required to describe the n & k dispersion. The 2nd Gaussian was less important for samples with simpler dispersions (in which case there would be more inter-correlation between the parameters of the 2 Gaussians due to the less flexibility necessary to fit a simpler dispersion shape). The challenge occurs when multiple oscillators are employed to describe the overall (particularly broad) dispersion shape, there will likely be some internal correlation between the parameters. To avoid such concerns, our goal was to use the oscillator(s) to determine the final overall n & k dispersion shape and that this dispersion shape could be described by using different general dispersion models which are available to the researcher. In our case, 2 Gaussians were used, but the overall basic shape could likely be obtained by using combinations of multiple oscillators – say, multiple Gaussian, Lorentz, or Tauc-Lorentz, etc. So once an optical model is used to determine the overall n & k dispersion, then we followed up with other relationships (Tauc, Urbach, Jackson-Amer, Wemple DiDomenico, etc) to extract parameters specific to this overall shape. These relationships were based off spectroscopic data and therefore, are expected to show correlation to film composition. The details of 1^{st} DOE are shown in table below. We did not get any visible deposition for 2 runs. The significant factors (labeled; out of the 2^n-1 combinations of the 4 factors) were easily decipherable as shown in the Half Normal Probability plots (Figure below). The design, resultant responses and significant factors of the 2^{nd} DOE are shown in Table 3.2 and Figure 3.3 below. Uncertainty Figure of Merit (FOM)[9] of n & k was calculated using Monte Carlo Fit-Result Analysis to be ±0.000212748 and ±6.58962E-05 respectively or ±0.010% and ±0.256% of average n and k. The uncertainty is calculated as FOM(n) and FOM(k) where the FOM is product of the standard 90% confidence limit and the square root of the Mean Square Error (MSE), a weighted Chi-square estimate of measurement error.

Table 3.1 1st Full Factorial Statistical Design of Experiment in 4 process variables and the measured VASE responses

Run	Block	Factor 1	Factor 2	Factor 3	Factor 4	Thickness (A)	n@633nm	k@633nm
		A:O2 :Ar ratio	B:Pressure	C:RF Power	D:RF1 bias			
		sccm	*mT*	*W*	*W*			
1	100C	0.25	7	200	0	672.66	1.9781	0.0044
2	100C	0.25	3	200	10	320.77	2.1745	0.0232
3	100C	0	3	200	0	1297.76	2.2848	0.0066
4	100C	0	3	100	10	312.11	2.3674	0.0259
5	100C	0	7	200	10	561.92	2.1993	0.0014
6	100C	0	7	100	0	666.47	2.2757	0.3482
7	100C	0.5	5	150	5	270.01	2.0949	0.0263
8	100C	0.25	3	100	0	347.19	2.1596	0.0841
9	100C	0.25	7	100	10			
10	25C	0.5	5	150	5	342.77	2.2178	0.0140
11	25C	0.25	7	200	10	363.15	2.267	0.0122
12	25C	0.25	7	100	0	264.13	2.1342	0.0096
13	25C	0.25	3	200	0	827.52	2.2697	0.0243
14	25C	0	7	100	10	281.59	2.1595	0.0026
15	25C	0.25	3	100	10			
16	25C	0	3	200	10	663.79	2.2118	0.0082
17	25C	0	7	200	0	1280.71	2.2647	0.0125
18	25C	0	3	100	0	564.84	2.5352	0.5790

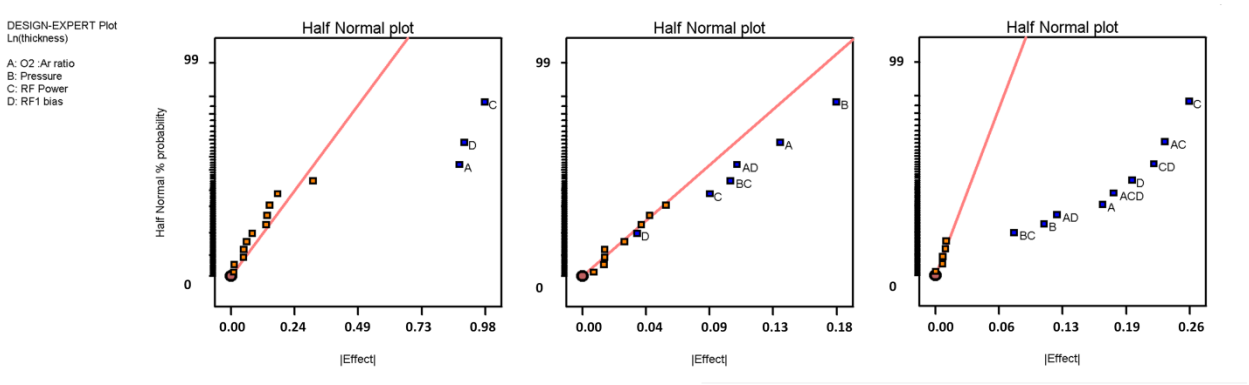

Figure 3.2 Half Normal Probability plots of VASE responses – Thickness, refractive index 'n' and extinction coefficient 'k' for the 1st DOE

Table 3.2 2nd Full Factorial Statistical Design of Experiment in 3 process variables and the measured VASE responses

Run	Factor 1	Factor 2	Factor 3	Thickness (A)	n@633nm	k@633nm
	A:O2 flow	B:RF Power	C:RF1 Bias			
	sccm	*mT*	*W*			
1	0	200	0	1186.47	2.3377	0.0060
2	0	200	2	969.42	2.3772	0.0000
3	2	200	2	492.52	2.2235	0.0048
4	0	150	0	822.34	2.3109	0.0066
5	2	150	2	257.9	2.2001	0.0035
6	1	175	1	476.87	2.3204	0.0161
7	2	150	0	348.7	2.1702	0.0149
8	2	200	0	613.42	2.2253	0.0175
9	0	150	2	648.55	2.2580	0.0027

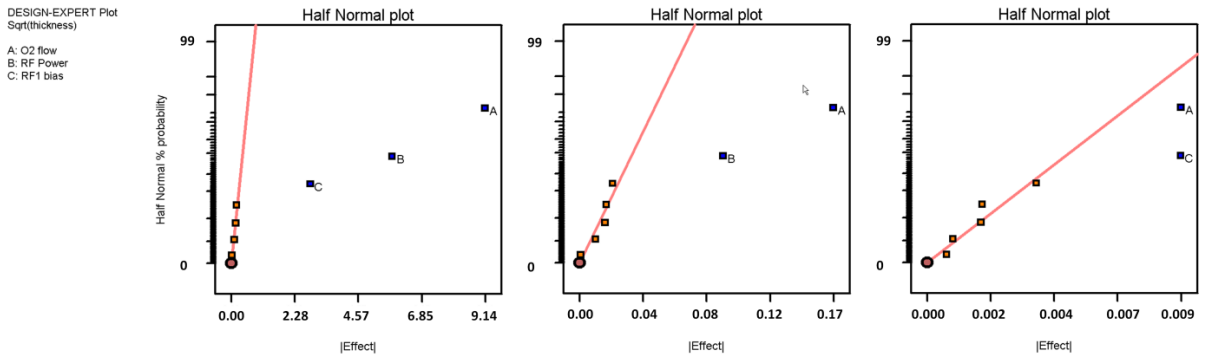

Figure 3.3 Half Normal Probability plots– Thickness, Refractive Index 'n' and Extinction coefficient 'k' for the 2nd DOE

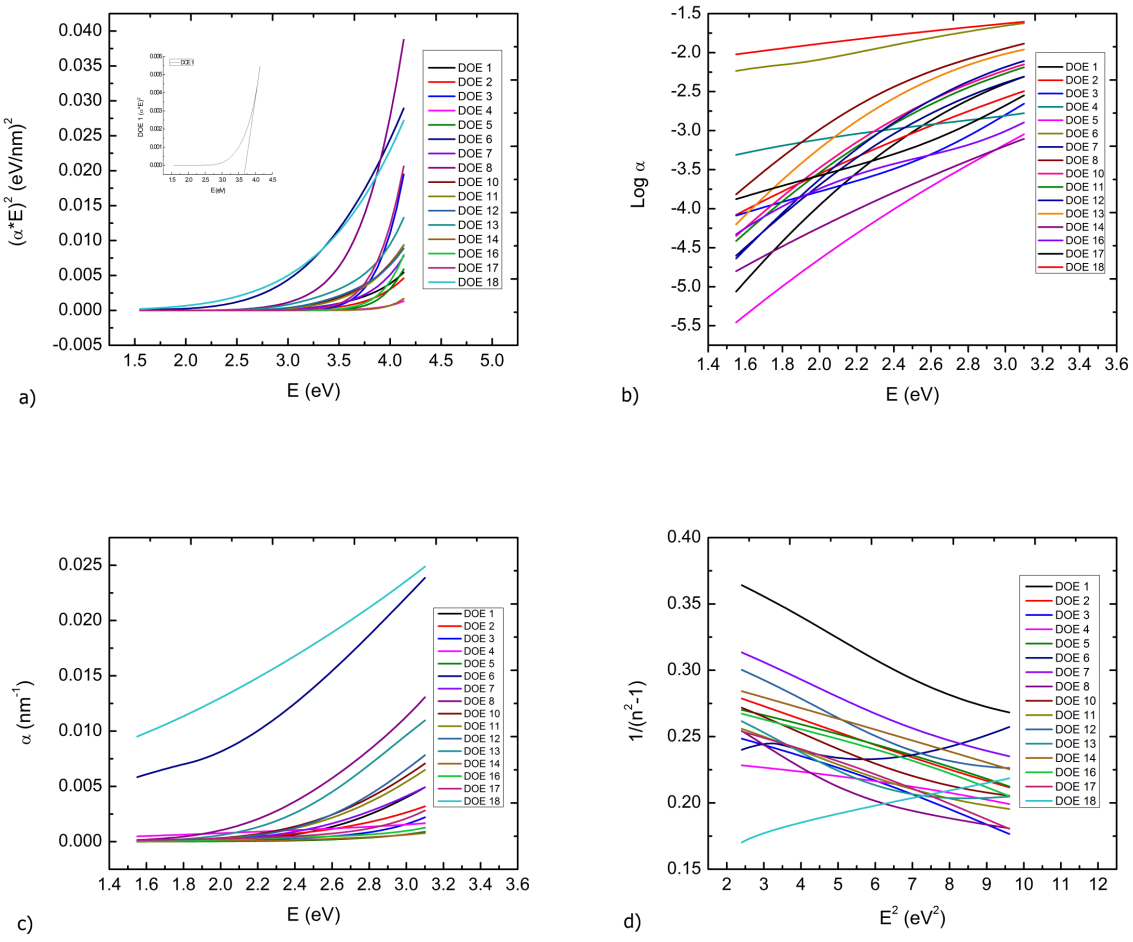

Figure 3.4 (a) Tauc plot with inset showing the tangent line to x-axis to derive E_g, (b) Urbach plot to derive E_u, (c) Jackson-Amer plot to determine sub-gap absorption and (d) Wemple-DiDomenico plot to derive E_o and E_d

Figures 3.4(a)-(d) depict the plots based on equations 8-13. This graphical data and derived parameters are summarized in Table 3.3. Wemple-DiDomenico parameters for Samples 6 and 18 could not be derived as they did not follow the $1/(n^2-1)$ vs. E^2 relationship. These samples have very high optical absorption (as evidenced by the high k, α_{s-g} and B_{Tauc} and low E_g values) and therefore do not conform to the single oscillator approximation employed in the Wemple-DiDomenico relationship[14].

Table 3.3 Various Optical Dispersion parameters derived from n &k for 1st DOE samples

	Moss's Rule	E_g	E_u	E_o	E_d	α_{s-g}	B_{Tauc}	Tauc m
DOE1	56.01	3.658	0.537	5.235	13.147	1.802E-03	0.001520	3.054
DOE2	85.70	3.759	0.963	5.636	18.717	1.470E-03	0.005685	2.538
DOE3	104.57	3.838	1.185	5.312	19.426	7.835E-04	0.004157	2.621
DOE4	114.87	3.853	2.938	7.882	33.040	1.578E-03	0.022416	1.808
DOE5	90.52	3.867	0.634	6.094	21.012	2.859E-04	0.000747	3.093
DOE6	83.32	3.147	2.431			1.974E-02	0.067273	1.775
DOE7	71.81	3.738	0.643	5.402	15.891	2.052E-03	0.002829	2.856
DOE8	103.96	3.629	0.766	4.975	18.159	6.575E-03	0.008019	2.642
DOE10	87.00	3.593	0.675	5.379	18.299	3.014E-03	0.003978	2.784
DOE11	94.78	3.586	0.668	5.496	19.885	2.712E-03	0.003603	2.808
DOE12	75.60	3.644	0.580	6.451	22.464	3.110E-03	0.002645	2.933
DOE13	96.89	3.651	0.654	4.529	15.290	5.206E-03	0.005263	2.748
DOE14	85.65	3.939	0.902	6.111	20.104	3.372E-04	0.002353	2.662
DOE16	93.22	3.895	1.156	5.928	20.574	6.285E-04	0.004401	2.545
DOE17	100.01	3.802	1.268	5.304	18.968	1.110E-03	0.005794	2.532
DOE18	131.39	3.168	3.657			2.545E-02	0.098372	1.568

Wemple-DiDomenico parameters show correlation to elemental content - similar to that observed for epitaxial, crystalline and stoichiometric PZT thin films[15]. However, in our 1st DOE films the Zr and Ti contents are directly correlated and Pb and O contents inversely correlated to E_g, E_o and E_d. Also, the refractive index is inversely correlated to E_o and not correlated to E_d. Please note that E_o is correlated to band gap E_g whilst E_d is the average strength of interband optical transitions and is affected by the structural order of the material[14]. In the 1st DOE, the stoichiometry ratio Pb/(Ti+Zr) varies from 0.28-2.24 whilst Zr/Ti varies 0.13-0.86 (<1.083 for PZT 52/48). The refractive index increases with both Ti and Zr concentration and only slightly with Pb.

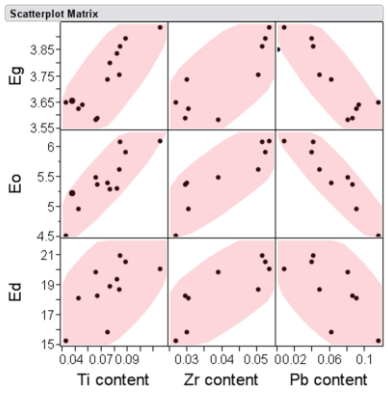

Figure 3.5 Scatterplot of Tauc Optical Gap E_g and Wemple-DiDomenico parameters E_o and E_d vs. Atomic fractions

For the 2nd DOE, the various optical parameters were derived from n & k data (Table 3.4). Both E_o and E_d show good dependence on elemental content with the latter being the best. O, Zr and Ti content were more correlated than Pb. We attribute the better correlations to the tighter distribution of relative atomic contents of Pb, Zr vs. Ti. The Pb/(Zr+Ti) for all 2nd DOE samples are > 1 (1.23-2.13) and Zr/Ti ratio ranges from 0.6-1.8 (ideal = 1.083).

Table 3.4 Various Optical Dispersion parameters derived from n & k for 2nd DOE samples

	Moss's Rule	E_g	E_u	E_o	E_d	α_{s-g}	B_{Tauc}	Tauc m
DOE1	118.00	3.644	0.2744	5.049	20.028	2.113E-03	0.002501	2.919
DOE2	118.70	3.730	0.2681	6.179	25.855	6.393E-05	0.000000	5.241
DOE3	91.63	3.817	0.2620	5.243	17.646	2.204E-03	0.002068	2.979
DOE4	111.62	3.853	0.2595	5.344	20.317	1.269E-03	0.002391	2.878
DOE5	79.08	3.874	0.2581	4.325	12.017	2.131E-03	0.002672	2.881
DOE6	87.44	3.147	0.3178	4.756	16.887	4.277E-03	0.004888	2.751
DOE7	73.99	3.708	0.2697	4.391	12.113	3.443E-03	0.006103	2.633
DOE8	86.23	3.579	0.2794	4.667	15.047	4.411E-03	0.004095	2.818
DOE9	92.69	3.593	0.2783	5.430	19.407	7.724E-04	0.001443	2.992

Discussion

Background and Description of Prediction Methodology

As per Robertson[16],[17] and Silva[18], the band states of PZT are blended as - a) the valence band is populated mostly with the 2p states of the O^{2-} ions, b) the Pb^{2+} leaves a lone pair 6s state that interacts strongly with the O 2p orbitals; these interactions sets the upper limit of the valence band; the valence band in PZT is thus determined by the Pb s to O p interaction independent of Zr/Ti stoichiometry, c) the conduction band is defined by the Ti^{4+} 3d states but its minimum is defined by Pb 6p states with increase in Zr content and d) the Pb 6p character increases with Zr content. In addition, Robertson[19] discovered that 3.6eV (344nm) UV light created shallow hole traps Pb^{3+}(hole trapped at a Pb^{2+} site) and Ti^{3+} electron traps (electron trapped at Ti^{4+} site). This phenomenon can occur in our tests too as the VASE lower wavelength limit was 300nm. As

per Silva[18], the Pb to Zr-O_6 or Ti-O_6 bonding is ionic whilst that between Zr-O and Ti-O, the bonds are covalent. Silva confirmed with Density Functional Theory (DFT) modeling that any displacement by Ti or Zr will cause a decrease in E_g (by enlargement of the valence and conduction bands) and the creation of gap states. Therefore, both the bonding state of the Pb, Zr and Ti with O and their relative atomic positions can affect the optical band gap. For both DOE's, Jackson Amer parameter, $a_{s\text{-}g}$ is affected slightly by elemental content – an exponential increase with Pb content and decreasing exponential with O, Zr and Ti contents. Less oxygen vacancies can be expected to decrease localized defect states. According to Davis and Mott[20], the presence of high density of localized states in the band structure is responsible for lower values of the optical gap. We confirm that with the inverse relationship noticed between Jackson Amer parameter $a_{s\text{-}g}$ and optical band gap E_g. As per Watanabe[21], the refractive index and the square of the slope of the Tauc plot (known as B-parameter or B_{Tauc}) are inversely proportional to the width of the tail states and is a measure of the gradient of the density of states at the conduction band edge. The lower the product of the two, sharper is the conduction band edge. We observed a consistent correlation between $n*B_{Tauc}^2$ and band edge sharpness parameters, Urbach energy, E_u, and Jackson Amer parameter $a_{s\text{-}g}$. Moss's rule[22] states that n^4E_g is a constant (~95eV; slope in a plot of n^4 vs. $1/E_g$). For our films, the Moss's parameter ranges from 56-131 eV independent of elemental composition. Tauc optical gap, E_g, and Wemple-DiDomenico parameters, E_o and E_d, show compositional dependencies (Figure 3.5). These mixed results can be attributed to the fact that none of the prior optical theories (summarized in Table 3.5) provide a constitutive optical relationship that captures the effect of relative concentrations of elements in the material. Next, we reveal this missing link.

Table 3.5 Summary of Optical parameters derived from Ellipsometric data

Type of Plot	Calculated Parameter	Nomenclature	Computation
Tauc	Optical Band Gap	E_g	Intercept on x-axis of tangent line from $(aE)^2$ vs photon Energy (E)
Urbach	Urbach Width	E_u	Inverse slope of log of absorption 'a' vs. photon energy (E) where $E < E_g$
Jackson-Amer	Sub-gap absorption	a_{s-g}	Area under absorption 'a' vs. photon energy (E) where $E < E_g$
Wemple-DiDomenico	Dispersion energy and Single Oscillator energy	E_d and E_o	Computed from plot of $1/(n^2-1)$ vs E^2 using Eq. 12

Electronic and ionic polarizations are due to field induced dipole moments while orientational polarization is due to permanent dipole moments. These three are categorized as paraelectric polarization. There are 3 non-paraelectric polarizations – a) ferroelectric or spontaneous (non-centrosymmetric materials), b) space charge (due to trapped charges from mobile ions or charge carrier traps in amorphous material) and c) hopping (due to localized states in glasses and amorphous semiconductors). From these definitions[23], as deposited RF sputtered PZT films may have paraelectric along with space charge and hopping polarizations.

For multi-component absorbing films, like our amorphous PZT films, we need to expand beyond the above simple correlations. For this purpose, we will utilize the relationship between microscopic polarizability and macroscopic refractive index – the Lorentz-Lorenz equation [24]:

$$\alpha_m = \alpha_{m,r} - i\alpha_{m,i}$$

$$\alpha_{m,r} = \frac{(n^2 - k^2 - 1)(n^2 - k^2 + 2) + (2nk)^2}{(n^2 - k^2 + 2)^2 + (2nk)^2} \frac{3M}{4\pi\rho N_A}$$

$$If\ LL_{real} = \frac{(n^2-k^2-1)(n^2-k^2+2)+(2nk)^2}{(n^2-k^2+2)^2+(2nk)^2} \quad then, \alpha_{m,r} = LL_{real}\frac{3M}{4\pi\rho N_A}$$

$$\alpha_{m,i} = \frac{6nk}{(n^2-k^2+2)^2+(2nk)^2}\frac{3M}{4\pi\rho N_A} \tag{14}$$

The imaginary part of electronic polarizability is often a few orders of magnitude less than the real part. The above relationship also provides a method to measure the density of a sample based on its optical properties and polarizability. An empirical relationship for electronic polarizability has also been derived by Reddy et.al.[25] using band gap, E_g , and optical electronegativity of the material, $\Delta\chi$.

$$\alpha_{rrr} = 0.395e^{-24}\frac{4.027+K}{7.027+K}\frac{M}{\rho}\ where\ K = \ln\Delta\chi(\ln\Delta\chi - 4.564) \text{and } \Delta\chi = 0.2688E_g \tag{15}$$

Optical electronegativity of a material is indicative of the nature of bonding and is a measure of the strength of its ionicity and conversely, the lower it is, the higher the covalency. We had noticed that optical band gap E_g increases with Zr (consistent with reference [16]) and Ti content and decreases with Pb. Therefore, Reddy polarizability relationship will be ideal in capturing these dependencies.

If we apply volume mixing rules for density[26], ρ_i and atomic weights M_i, we get the following relationships for effective density ρ_e and effective molecular weight M_e vs. the volume fraction, v_i (related to the atomic or molar fraction, f_i) -

$$\rho_e = \sum_i v_i\rho_i \ ; \qquad M_e = \frac{\sum_i v_i\rho_i}{\sum_i \frac{v_i\rho_i}{M_i}} \ ; \quad v_i = \frac{\frac{N_iM_i}{\rho_i}}{\sum_i \frac{N_iM_i}{\rho_i}} = \frac{\frac{N_iM_i}{N_A\rho_i}}{\sum_i \frac{N_iM_i}{N_A\rho_i}} = \frac{\frac{f_iM_i}{\rho_i}}{\sum_i \frac{f_iM_i}{\rho_i}} \tag{16}$$

Thus, with the above mixing rules, the electronic polarizability relationships can incorporate the confounded effects of elemental composition. Using Eq. 16, effective density ρ_e and effective molecular weight M_e is computed for each sample and substituted in Eq. 14 and 15 to compute $\alpha_{m,r}$ and α_{rrr} for each sample. The equivalent effective electronic polarizability[26] is given by $\alpha_e = \sum_i f_i \alpha_i$ where f_i is atomic or molar fraction given as $f_i = \frac{N_i}{\sum_i N_i}$. For effective polarizability, electronic polarizabilities for Pb^{2+}, Zr^{4+}, Ti^{4+} and $O^{2-}$of 4.9, 0.37, 0.19 and 2.22 (x e^{-24}) are taken from literature[27]. Naturally, in amorphous films, one can expect other valencies of these constituent elements and therefore, α_e does not depict actuality well. The magnitudes of $\alpha_{m,r} > \alpha_{rrr} > \alpha_e$ across all samples. Figure 3.6 depicts each of these polarizabilities plotted against elemental content for the 1st DOE samples.

For perovskites ABO_3, like PZT, a tolerance factor (tf) has been proposed as a measure of perovskite structure formability. An additional factor called the octahedral factor (of) is combined to further improve predictability[28].

$$tf = \frac{r_A + r_O}{\sqrt{2}\,(r_B + r_O)} \text{ and } \quad of = \frac{r_B}{r_O} \tag{17}$$

To accommodate the atomic fractions in PZT, these factors were modified as follows,

$$tf_{PZT} = \frac{f_{Pb} r_{Pb} + f_O r_O}{\sqrt{2}\,(f_{Zr} r_{Zr} + f_{Ti} r_{Ti} + f_O r_O)} \text{ and } \; of_{PZT} = \frac{f_{Zr} r_{Zr} + f_{Ti} r_{Ti}}{f_O r_O} \tag{18}$$

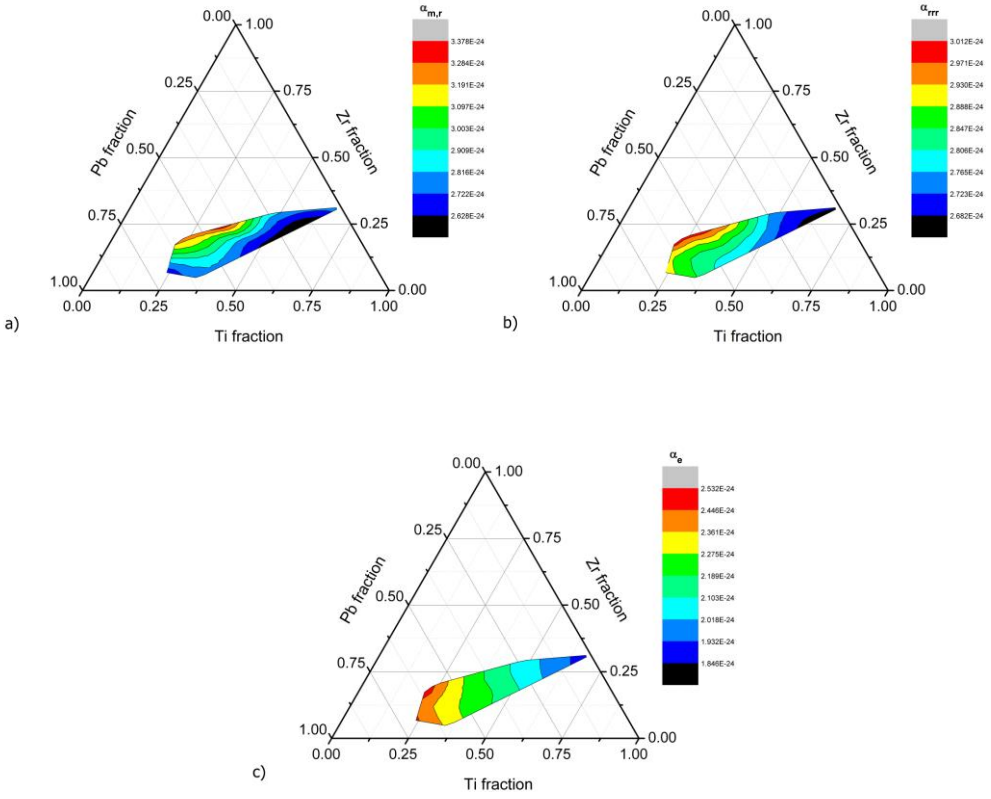

Figure 3.6 Electronic polarizabilities vs. Atomic fractions for the 1st DOE - a) αm,r b) αrrr and c) α_e.

Table 3.6 Comparison of Ionic Radii for Pb, Zr, Ti and O

Valency	Ionic Radii(A)			
	Pb	Zr	Ti	O
4+	0.84	*0.79*	*0.68*	
3+			0.76	
2+	*1.20*		0.94	
1+		1.09	0.96	
-1				1.76
-2				*1.32*

The ionic radii[29] of Pb, Zr, Ti and O is given in the Table 3.6 (radii for perovskite PZT is in italics). Therefore, for $Pb(Zr_{0.52}Ti_{0.48})O_3$, octahedral and tolerance factors can be calculated to be 0.186 and 0.777 respectively. We found that this group variable is highly correlated to polarizability. Clearly, from Figure 3.5, E_o shows the best correlation to elemental content and amongst the latter, Ti and Pb content is best correlated. Linear fits to E_o vs. elemental content were made as listed below. The numbers in square brackets are Rsquared (R^2) and Root Mean Square error (RMSE) of the regressions (as computed by JMP™ statistical software). The electronic polarizabilities are evidently correlated to each other as they all utilize atomic fractions in their calculations.

$$f_{Ti} = -0.132151 + 0.0375312 * E_o, [\mathrm{R}^2 = 0.832,\ \mathrm{RMSE} = 0.009]$$

$$f_{Zr} = -0.066168 + 0.0193297 * E_o, [0.768, 0.006]$$

$$f_{Pb} = 0.3855925 - 0.0586112 * E_o, [0.857, 0.013]$$

$$\alpha_e = -6.59e^{-25} + 4.01e^{-24} * tf\ , [0.999, 4.44\mathrm{e}^{-27}]$$

$$\alpha_{rrr} = 1.821e^{-24} + 0.452158 * \alpha_e, [0.973, 1.22\mathrm{e}^{-26}]$$

$$\alpha_{m,r} = 1.348e^{-24} + 0.7085994 * \alpha_e, [0.635, 8.63\mathrm{e}^{-26}] \qquad (19)$$

For prediction, we substituted the empirically derived (from n&k dispersion data) LL_{real}, E_o and E_g in the $\alpha_{m,r}$, α_{rrr} and α_e relationships and solved the above equations for the atomic fractions with the added constraint that $\sum_i f_i = 1$.The results of the prediction methodology are shown in Figure 3.7. The methodology has been summarized in the flow chart below (Figure 3.8).

Understandably, better the correlations between the optical and compositional variables in the initial model, the better the predictability of this methodology.

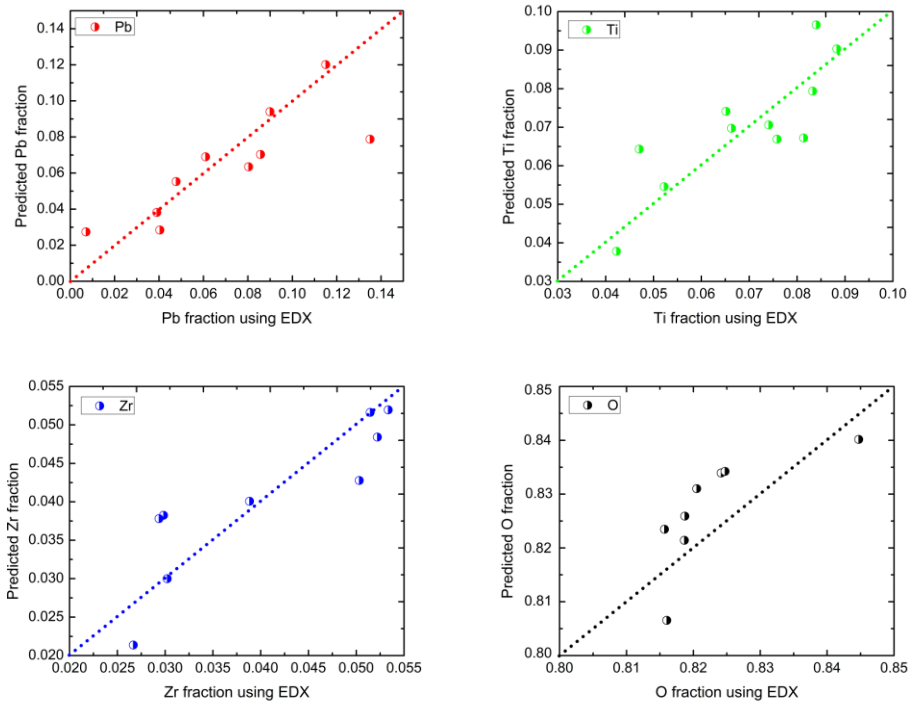

Figure 3.7 Predicted vs. Actual (EDX) Atomic fractions for the 1st DOE (dotted line depicts x=y)

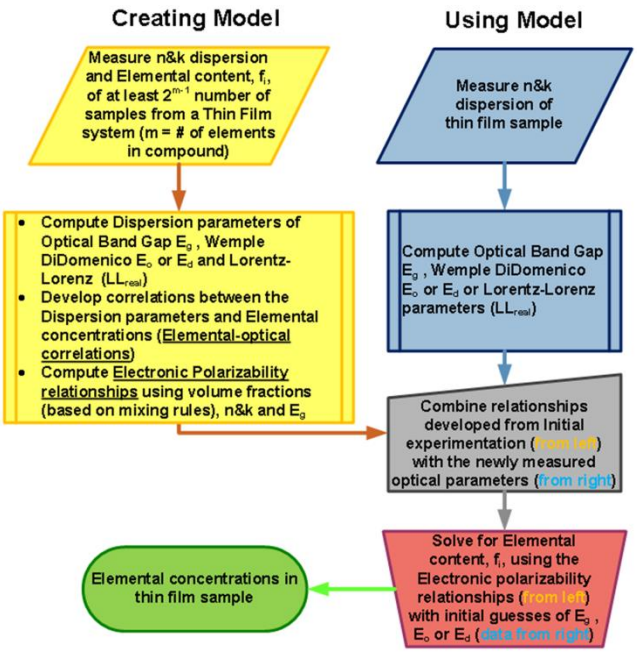

Figure 3.8 Flowchart of Proposed methodology

Validation of Prediction Methodology

For validation, we utilized the data from the 2nd DOE. The 2nd DOE's electronic polarizability plots also demonstrated a tighter distribution amongst samples (Figure 3.9). For prediction, from n&k dispersion data, we calculated 3 parameters LL_{real}, E_d and E_g for each sample and substituted these values in their relationships in Equation 20 and solved these equations for atomic fractions with the added constraint that $\sum_i f_i = 1$. The validation results show good match (as noted by the narrow spread from the diagonal line x = y) to measured as shown in Figure 3.10.

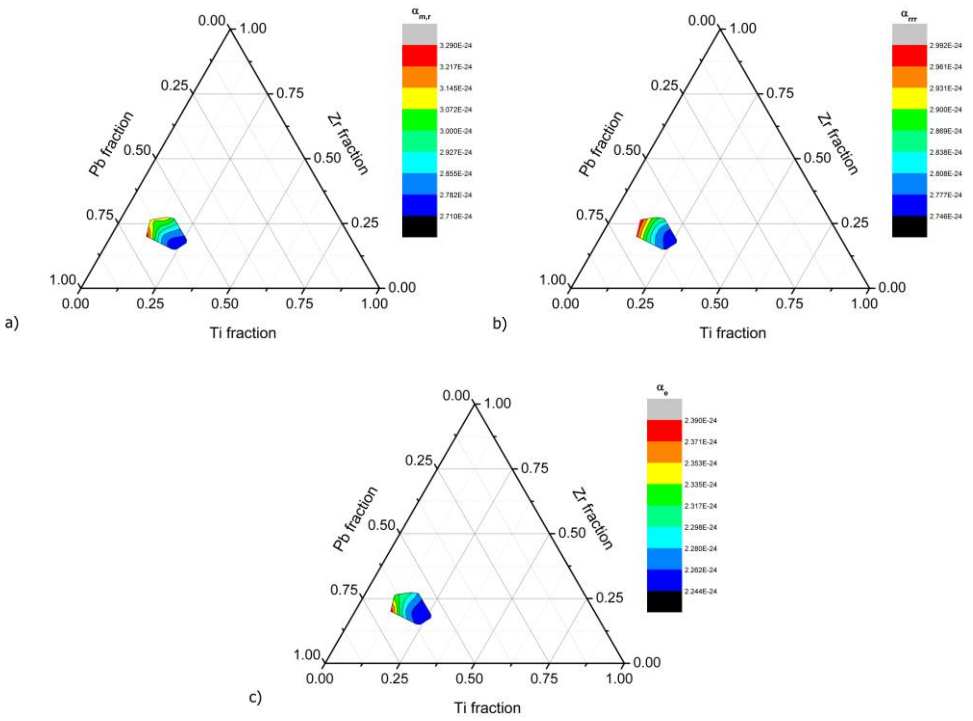

Figure 3.9 Electronic polarizabilities vs. Atomic fractions for the 2nd DOE - a) αm,r b) αrrr and c) α_e

$$f_O = 1.0784887 - 0.0095597 * E_d, [\mathrm{R}^2 = 0.751,\ \mathrm{RMSE} = 0.020]$$

$$f_{Ti} = -0.00194 + 0.0008824 * E_d, [0.785, 0.002]$$

$$f_{Zr} = -0.026912 + 0.0027377 * E_d, [0.812, 0.019]$$

$$\alpha_e = -2.61e^{-25} + 3.508e^{-24} * tf, [0.998, 2.41\mathrm{e}^{-27}]$$

$$\alpha_{rrr} = -9.96e^{-25} + 1.6814707 * \alpha_e, [0.797, 4.34\mathrm{e}^{-26}]$$

$$\alpha_{m,r} = -5.73e^{-24} + 3.7944908 * \alpha_e, [0.825, 8.96\mathrm{e}^{-26}] \quad (20)$$

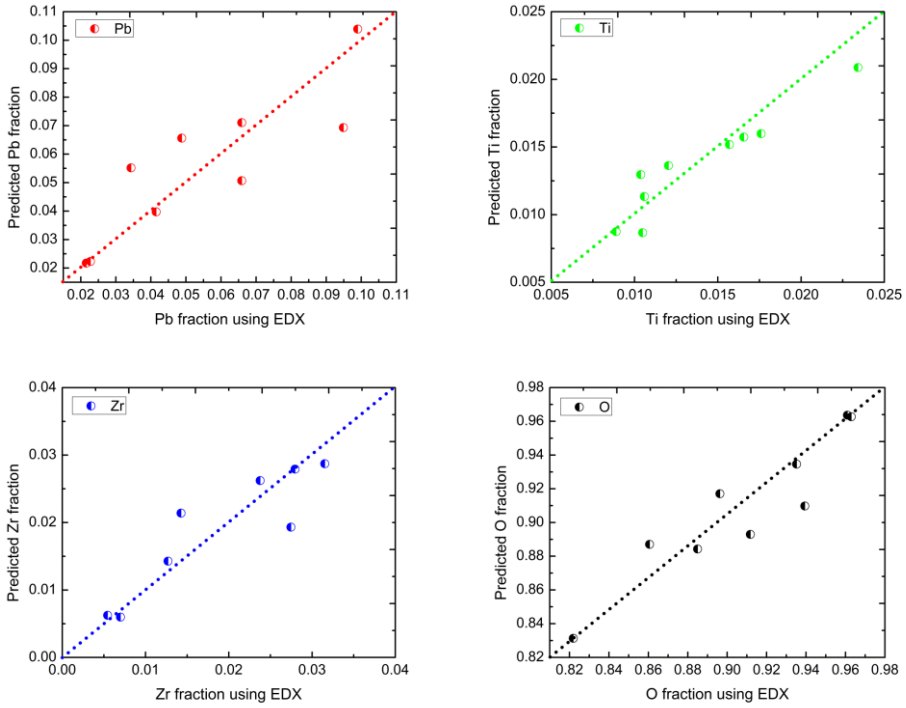

Figure 3.10 Predicted vs. Actual (EDX) Atomic fractions for the 2nd DOE (dotted line depicts x=y)

To quantify the effectiveness of this approach, in Table 3.7, we list the F-test and T-test of the predicted vs. actual atomic fractions for each of the two DOE's. F-test and T-test values > 5% (95% confidence interval) will prevent rejection of the null hypothesis for each pair (actual vs. predicted) of elemental content data sets. The null hypothesis for F-test is that the variance is equal between two samples and for T-test, the means of the two samples are statistically equal. The F-test null hypothesis is rejected for the Oxygen content in the 1st DOE because the error in predicted values of Oxygen is the sum of that for the other elements, Pb, Zr and Ti. Hence, better the n-1 correlations between the elemental content and optical parameters, less the error in prediction of the nth elemental content.

Table 3.7 Statistical comparison between the Actual and Predicted for each set of DOE samples

		f[Pb]	f[Zr]	f[Ti]	f[O]
1st DOE	F-test	29.91%	50.77%	48.19%	0.00%
	T-test	11.57%	64.80%	57.19%	15.60%
2nd DOE	F-test	78.70%	47.64%	58.18%	73.55%
	T-test	96.65%	84.34%	89.10%	96.10%

Conclusion

At the high frequencies of optical characterization, major contribution from the film composition to the optical performance comes from atomic and electronic polarizations. We postulated that by utilizing Kramer-Kronig consistent optical relationships and electronic polarizability calculations along with appropriate volume mixing rules, we can model elemental composition vs. optical properties. Such models may be reversed and used to predict atomic fractions from refractive index and extinction coefficient. For the case study, we used as-deposited amorphous RF sputtered Lead Zirconium Titanate (PZT) thin films. Statistical modeling of elemental concentrations vs. optical parameters (the latter condenses the spectroscopic n&k data into singular values) derived from Tauc and Wemple-DiDomenico plots was undertaken and the models thus derived were combined with optically derived electronic polarizability relationships to develop a methodology to predict atomic fractions. Efficacy of this methodology was validated with 2 PZT Elemental-optical datasets. This scheme has thus been employed effectively as a lab scale non-destructive compositional metrology technique for our piezoelectric thin films. The use of above and below band gap optical parameters in the modeling ensures the universality and versatility of the methodology. As part of this investigation, we also

have noticed some interesting trends in the sub-gap density of states, optical band gap and dispersion energy of PZT thin films.

Acknowledgements: The authors gratefully acknowledge the financial support from Air Force Office of Scientific Research (AFOSR) through Young Investigator Program. We are also greatly indebted to Clayton Loehn for the EPMA/WDS and EDX characterization work conducted at Department of Geosciences at Virginia Tech and to Matthew Williams of Department of Statistics at Virginia Tech for assistance with JMP™ statistical analysis.

References

[1] Gladstone JH. Researches on the refraction, dispersion, and sensitiveness of liquids. Philosophical transactions of the Royal Society of London 1863;153:317.
[2] Eggleton RA. Gladstone-Dale constants for the major elements in silicates: Coordination number, polarizability, and the Lorentz-Lorentz relation. Canadian Mineralogist 1991;29:525.
[3] Rocquefelte X. On the Volume-Dependence of the Index of Refraction from the Viewpoint of the Complex Dielectric Function and the Kramers−Kronig Relation. The journal of physical chemistry. B 2006;110:2511.
[4] Larsen ES. The microscopic determination of the nonopaque minerals: U.S. Geological Survey Bulletin, 1921.
[5] Teertstra DK. THE OPTICAL ANALYSIS OF MINERALS. Canadian Mineralogist 2005;43:543.
[6] Teertstra DK. Index-of-refraction and unit-cell constraints on cation valence and pattern of order in garnet-group minerals. Canadian Mineralogist 2006;44:341.
[7] Teertstra DK. Photon Refraction In Dielectric Crystals Using a Modified Gladstone-Dale Relation. The Journal of Physical Chemistry C 2008;112:7757.
[8] Yang S, Mo D, Tang X. Spectroscopic ellipsometry studies of amorphous PZT thin films with various Zr/Ti stoichiometries. Journal of Materials Science 2002;37:3841.
[9] Various. WVASE32 Manual. J.A. Woollam., Inc. .
[10] Fujiwara H. Spectroscopic Ellipsometry Principles and Applications: John Wiley & Sons, 2007.
[11] Capper P, Kasap S, Koughia C. Springer Handbook of Electronic and Photonic Materials. Berlin: Springer US, 2006.
[12] Stenzel O. The Physics of Thin Film Optical Spectra: Springer, 2005.

[13] Jackson W, Amer N. Direct measurement of gap-state absorption in hydrogenated amorphous silicon by photothermal deflection spectroscopy. Physical review. B, Condensed matter 1982;25:5559.
[14] Wemple SH, DiDomenico M. Behavior of the Electronic Dielectric Constant in Covalent and Ionic Materials. Physical review. B, Solid state 1971;3:1338.
[15] Moret MP, Devillers MAC, Worhoff K, Larsen PK. Optical properties of PbTiO[sub 3], PbZr[sub x]Ti[sub 1−x]O[sub 3], and PbZrO[sub 3] films deposited by metalorganic chemical vapor on SrTiO[sub 3]. Journal of Applied Physics 2002;92:468.
[16] Robertson J, Warren WL, Tuttle BA. Band states and shallow hole traps in Pb(Zr,Ti)O3 ferroelectrics. Journal of Applied Physics 1995;77:3975.
[17] Robertson J. Band structures and band offsets of high K dielectrics on Si. Applied Surface Science 2002;190:2.
[18] Silva MS, Cilense M, Orhan E, Góes MS, Machado MAC, Santos LPS, Paiva-Santos CO, Longo E, Varela JA, Zaghete MA, Pizani PS. The nature of the photoluminescence in amorphized PZT. Journal of Luminescence 2005;111:205.
[19] Robertson J, Warren WL, Tuttle BA, Dimos D, Smyth DM. Shallow Pb3 hole traps in lead zirconate titanate ferroelectrics. Applied Physics Letters 1993;63:1519.
[20] Davis EA, Mott NF. Conduction in non-crystalline systems V. Conductivity, optical absorption and photoconductivity in amorphous semiconductors. Philosophical magazine (London, England : 1945) 1970;22:0903.
[21] Watanabe T, Kazufumi A, Nakatani M, Suzuki K, Sonobe T, Shimada T. Chemical Vapor Deposition of a-Si:H Films Utilizing a Microwave Excited Ar Plasma Stream. Japanese journal of applied physics 1986;25:1805.
[22] Sahoo NK, Thakur, S., Tokas, R. B. Achieving superior band gap, refractive index and morphology in composite oxide thin film systems violating the Moss rule. Journal of physics. D, Applied physics 2006;39:2571.
[23] Kao KC. Dielectric Phenomena in Solids: Elsevier Academic Press, 2004.
[24] Khawaja EE, Bouamrane F, Al-Adel F, Hallak AB, Daous MA, Salim MA. Study of the Lorentz-Lorenz law and the energy loss of 4He ions in titanium oxide films. Thin Solid Films 1994;240:121.
[25] Reddy RR, Nazeer Ahammed Y, Rama Gopal K, Abdul Azeem P, Sasikala Devi B, Rao TVR, Behere SH. On the equivalence between Clausius–Mossotti and optical electronegativity relations. Optical Materials 2003;22:7.
[26] Liu Y, Daum P. Relationship of refractive index to mass density and self-consistency of mixing rules for multicomponent mixtures like ambient aerosols. Journal of aerosol science 2008;39:974.
[27] Tessman J, Kahn AH. Electronic Polarizabilities of Ions in Crystals. Physical review 1953;92:890.
[28] Li C, Soh KCK, Wu P. Formability of ABO3 perovskites. Journal of alloys and compounds 2004;372:40.
[29] www.matweb.com.

Chapter 4

Thin Film Magnetostriction Measurement Using Laser Doppler Vibrometry

Ronnie Varghese,[1] Ravindranath Viswan,[2] Keyur Joshi,[1] Safoura Seifikar,[3] Yuan Zhou,[1] Justin Schwartz,[2] and Shashank Priya[1,*]

[1]Center for Energy Harvesting Materials and Systems (CEHMS), Bio-Inspired Materials and Devices Laboratory (BMDL), Virginia Tech, Blacksburg, VA 24061, USA
[2]Materials Science and Engineering Department, Virginia Tech, Blacksburg, VA 24061, USA
[3]Department of Materials Science and Engineering, North Carolina State University, Raleigh, North Carolina 27695, USA

Abstract

This paper reports laser doppler vibrometry based measurement technique for the magnetostriction in magnetic thin films. We have measured the strain induced by an AC magnetic field in the polycrystalline cobalt ferrite and nickel ferrite thin films on silicon and platinized silicon substrates under a DC magnetic bias. The experimental setup and the derivation of the magnetostriction constant from the experimentally measured deflection are discussed in detail. A comparative analysis was conducted with the Vibrating Sample Magnetometer (VSM) measurement and the value derived from the bending theory calculations of magnetically induced torque. At high DC magnetic field bias, the magnetization values calculated from the measured magnetostriction values match with the actual magnetization measured by VSM.

Keywords: thin films; doppler effect; magnetostriction; strain

Introduction

Magnetic thin films are used in magnetic storage media, generators, and magnetoelectric sensors. The strain induced in such films by a magnetic field, namely, magnetostriction is a fundamental property of the magnetic materials used in these applications. If the magnetostriction is positive, the sample elongates in the direction of the applied field irrespective of the direction of rotation of the magnetic moments and the thickness perpendicular to the applied field reduces such that the volume remains constant. If the magnetostriction is negative, the sample length decreases and the deformation in thickness direction increase. Under a varying magnetic field, magnetic thin films, deposited on substrates, impose a change in curvature of the substrate because of differences in the elastic moduli of the film and the substrate.

Magnetostriction measurement techniques can be broadly classified as either direct or indirect, depending on whether the strain is measured directly or the magnetostriction is deduced from a measurement of some other property dependent upon the strain. Measurements using strain gauges, capacitance transducers or optical techniques are considered direct[1]. In bulk applications, strain gauges (sensitivity 10^{-6}) are commonly used whilst the most sensitive is the capacitance method (sensitivity 10^{-6})[2]. However the major disadvantage of these two methods is the complex sample preparation and the inability to measure saturation magnetostriction respectively. Strain gauges are easy to handle but have limited sensitivity typically on the order of ~ 1ppm. Additionally, the saturation magnetostriction constant has to be determined from measurements conducted in the parallel and perpendicular direction to the applied external field. However, for unobtrusive (no damage to sample) non-contact strain metrology of thin films, the best approach appears to be optical means.

Prior studies reported in literature have conducted magnetostriction measurement in thin films using optical technique [1, 3-11]. The sample was rectangular shaped and clamped like a

cantilever. Such a setup requires the clamping of a thin film system inside a DC Helmholtz coil whilst also being under a fixed DC magnetic field of an electromagnet. The alignment of the clamp, sample, coil and electromagnet places limitations on the sample shape and size and mounting configuration. In this study, instead of using a cantilevered film-substrate system, we have placed the thin film sample directly on a non-magnetic stage inside a Helmholtz coil that applied an AC magnetic field parallel to the sample. In doing so, we have obviated the need of a clamp, reduced the noise contribution arising due to the vibrations coupling into a cantilever and achieved more freedom with respect to the sample shape and dimensions. Instead of using a rotating DC magnetic field from 3 Helmholtz coils in x, y and z directions [7-9] or directionally switched DC field in a single Helmholtz coil [10, 11], we use a 1kHz AC field in a single Helmholtz coil surrounding our sample. We then used laser doppler vibrometry (LDV) to measure the induced displacement at 1kHz in the unclamped sample. Vibrometry based on Doppler Effect is often used in the modal analysis of vibrating structures [12] and has been utilized for magnetostriction measurements of steel sheets (required attaching 2 mirrors on to the mm-scale sheets) [13]. The accuracy and resolution of such systems have improved to the picometer (1pm = 10^{-12} m; <0.4 pm/√Hz) range [14] and therefore opened the possibility of using such equipment for micro strains expected in magnetically stressed thin films.

Experimental Procedures

The schematic diagram of a typical laser doppler vibrometry equipment is shown below:

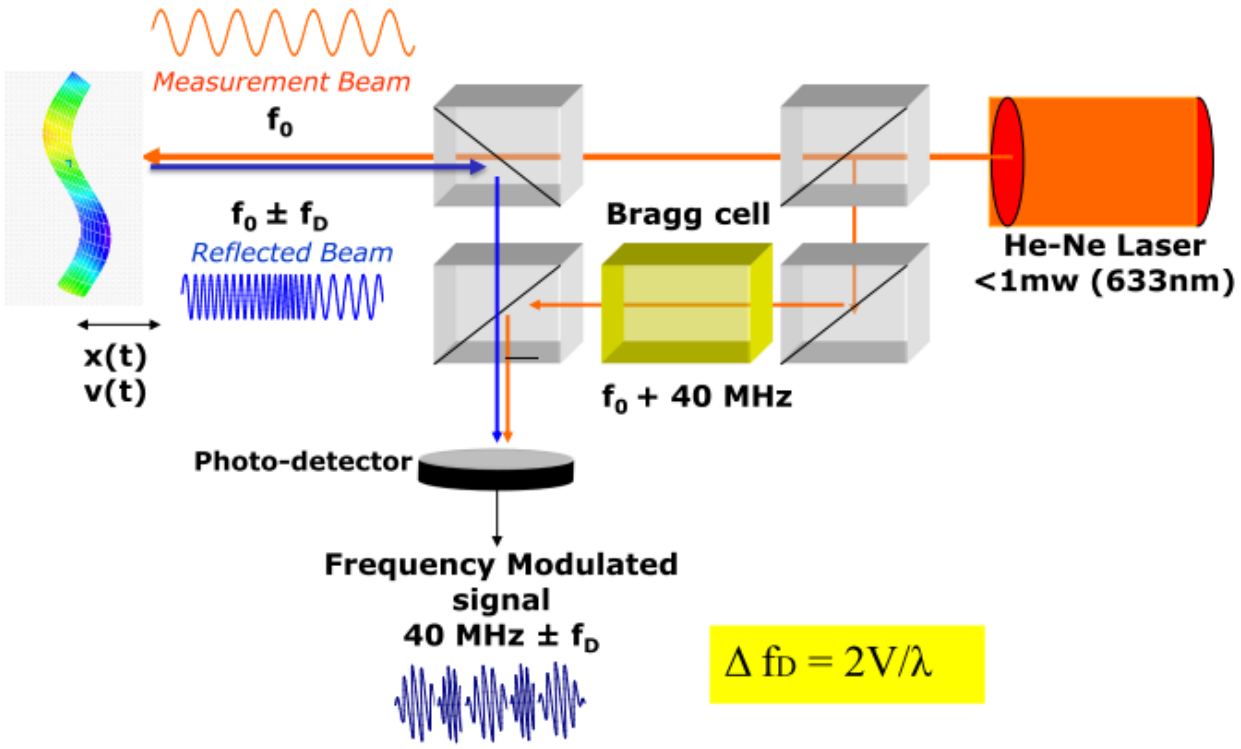

Figure 4.1 Laser Doppler Vibrometry technique [14].

We utilized Polytec LDV connected to a Polytec 5000 controller to measure the deflection (Δ) of a magnetostrictive film under two different applied AC magnetic fields of 1kHz, 1Oe and 1.45 Oe with varying DC magnetic bias from 0 to 6000 Oe. The AC field was applied parallel to the DC bias (longitudinal or parallel mode). The samples were <10mm on their sides and were square shaped. The thin film samples consisted of pulsed laser deposited cobalt ferrite ($CoFe_2O_4$; CFO) and RF sputter deposited nickel ferrite ($NiFe_2O_4$; NFO). The CFO films were deposited at 800 ^oC on platinized Si (150nm Pt/10nm Ti/300nm SiO_2/0.5mm Si; Inostek, Korea) substrates whilst NFO films were deposited on both platinized Si and 0.5mm Si substrates. The room temperature sputtered NFO films were post annealed at 650 ^oC, 700 ^oC and 750 ^oC in an atmospheric vertical furnace. The film thickness was measured by Variable Angle Spectroscopic

Ellipsometry. Squid (Superconducting QUantum Interference Device) measurements on a Quantum Design MPMS 3 system provided M-H data on the thin film samples.

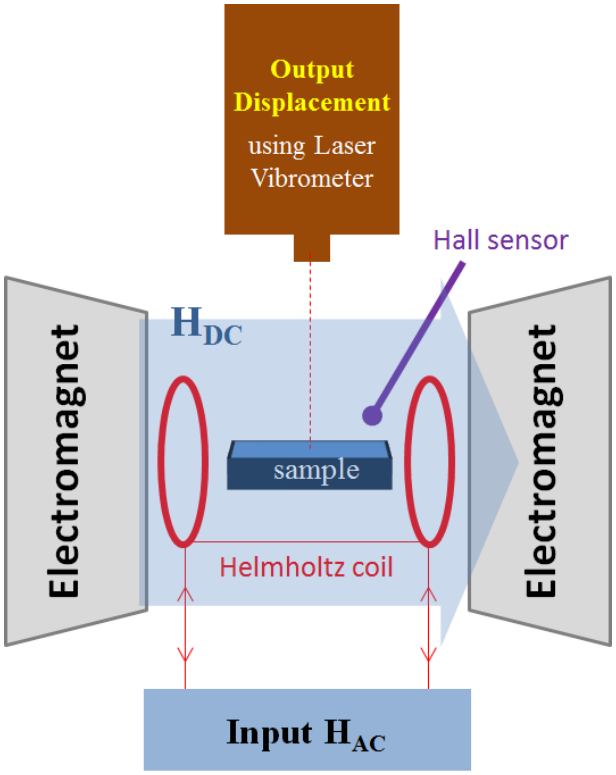

a)

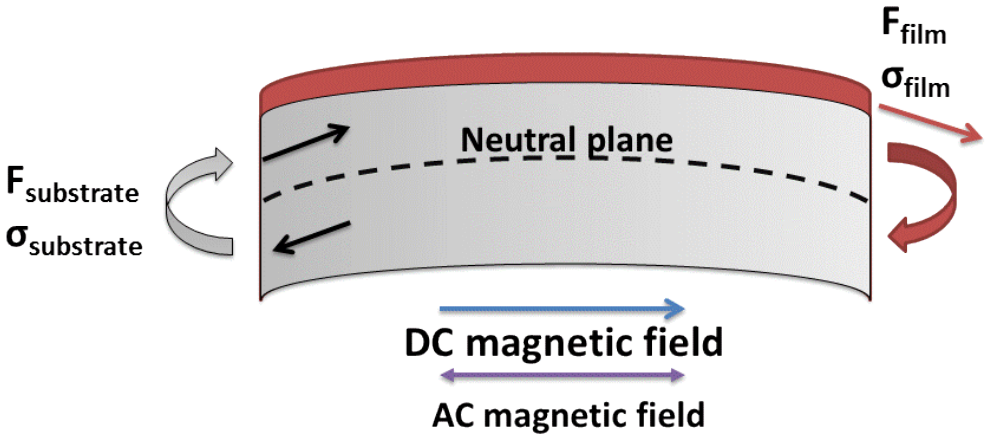

b)

Figure 4.2 a) \ Magnetostriction measurement setup and b) the schematic of the field and force vectors

The samples were directly placed inside a Helmholtz coil of dimension 34mm width x 57mm diameter with 28Ω coil resistance. The Helmholtz coil was placed between the poles of a GMW Associates 3470 dipole electromagnet driven by a Kepco Model BOP 100-4M power supply. Initially, a Polytec MSA 500 laser head was utilized but the displacement data with applied magnetic field was noisy. The issue was found to be related to the effect of the magnetic fields on the optomechanical mechanism inside the laser head. Polytec OFC 353 laser head which has a depth of field of 450mm was next utilized but still presented challenges. It was found that a minimum gap of 28" is required between the magnetic field systems (for a DC field of 6000 Oe and 1.45Oe 1 kHz AC, the gap varies with strength of the fields) and the laser head of the vibrometer. Despite this solution, it was noticed that nonmagnetic samples like Si substrate or a platinized Si substrate showed finite displacement at 1kHz AC field. Further investigations led to the finding that the laser vibrometer head, sample holder and magnetic Helmholtz coil plus electromagnet system are coupled structurally and thus any mechanical displacement in one system is propagated to the other influencing the magnetostriction measurement. Coils under an AC current are known to vibrate commonly known as coil noise or coil hissing [15, 16]. Each of the three components of the measurement setup, the coils, sample holder and the vibrometer had to be mechanically isolated from each other in order to avoid the mechanical coupling. The sample was loaded onto a 16" wooden spatula that was clamped to a shaker (with shorted coils) capable of providing needed vibration isolation. The Helmholtz coil plus DC electromagnet system was placed on an inflated inner tube and the laser was mounted on a tripod with rubber feet.

a)  b) 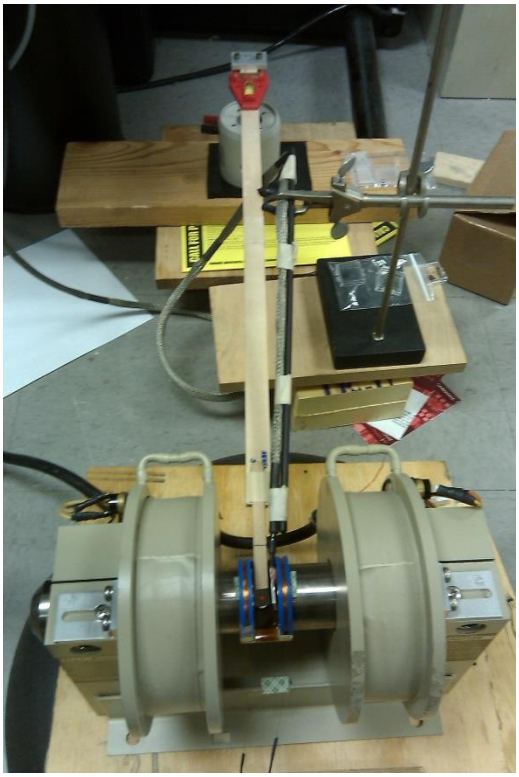

Figure 4.3 a) Side-view and b) Top-view of the magnetostriction measurement setup

In response to the applied magnetic field, magnetostrictive thin film extends in the direction of applied magnetic field and shortens in perpendicular directions developing an anisotropic biaxial stress system (thickness being very small compared to other dimensions, stress in thickness direction can be safely ignored) in the unclamped sample causing net deflection which will be maximum at the center of the sample. In longitudinal direction, due to applied magnetic field magnetic film tries to extend, which is resisted by the nonmagnetic substrate. Force balance requires that compression force exerted by the substrate be of exactly the same value but of opposite nature compared to extension force exerted by the magnetic film. This force couple acting on different locations creates a pure bending moment to which the sample (beam) is

subjected. Pure bending moment acting on a beam of uniform cross-section area beam deforms it in a circular arc. Radius of curvature of such an arc is given as:

$$R = \frac{\left(\frac{l}{2}\right)^2 + s^2}{2s} \quad (1)$$

where ‘l’ is the chord length (sample length) and ‘s’ is the sagitta (the distance from the center of the arc to the center of its base or chord) of the arc. The net vertical deflection Δ of the sample on application of the AC varying magnetic field is assessed as the sagitta ‘s’. The deflection Δ of the sample is calculated as the difference between the displacement ‘d’ measured by the LDV at 1Oe and 1.45Oe AC magnetic field at each DC bias magnetic field condition per unit AC field. We employed two AC field displacements for each DC magnetic bias so as to a) have a reference at each DC bias level and b) reduce noise in the data.

$$\Delta = 2s = \frac{\left(d_{AC_2} - d_{AC_1}\right)}{\left(AC_2 - AC_1\right)} \times AC_1 \quad (2)$$

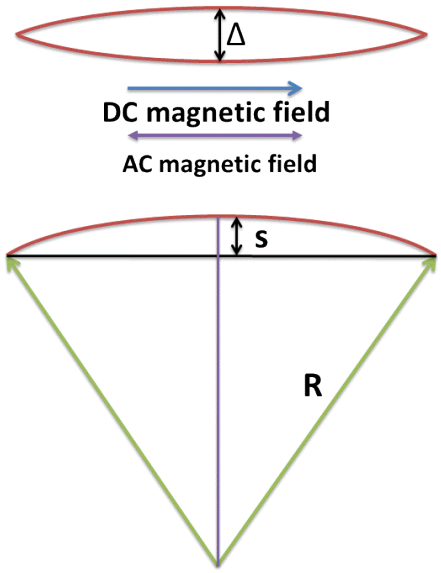

Figure 4.4 Schematic of the induced curvature in sample due to applied magnetic force

Substituting Eqn. (2) in (1) provides the radius of curvature which is then used to calculate the stress in the sample using force and bending moment balances [17]:

$$\sigma = \frac{1}{6Rt_f\left(t_f + t_s\right)}\left(\frac{Y_f t_f^3}{\left(1-\nu_f\right)} + \frac{Y_s t_s^3}{\left(1-\nu_s\right)}\right) \qquad (3)$$

where Y is the Young's modulus ($1.5\text{x}10^{11}$ N/m^2 for CFO, $1.6\text{x}10^{11}$ N/m^2 for NFO and $1.12\text{x}10^{11}$ N/m^2 for Si and platinized Si), ν is the Poisson's ratio (0.2 for CFO, 0.3 for NFO and 0.28 for Si and 0.29 for platinized Si) and t is the thickness. From the above stress calculation, we can then compute the magnetostriction in parallel or longitudinal mode (magnetic field and strain in parallel) as:

$$\lambda_{ll} = \frac{\sigma\left(1-\nu_f^2\right)}{Y_f} \qquad (4)$$

For comparison, we use the magnetostriction relationship derived for substrate deflections created by an anisotropic thin film stress generated in a magnetic field. This relationship was derived for the specific case of magnetostriction of thin films[18]:

$$\lambda_{ll} = \Delta \frac{Y_s t_s^2}{Y_f t_f} \frac{2}{9l^2} \frac{1+\nu_f}{1+\nu_s} \qquad (5)$$

Results

The vertical displacements of the samples at 1 kHz AC magnetic fields of 1Oe and 1.45Oe are shown in the table below:

Table 4.1: Displacement (in picometers) measured on NFO and CFO thin film samples by LDV at two different AC fields and various DC magnetic fields.

DC Bias (Oe)	1kHz AC(Oe)	90nm NFO/Pt+ 700C	90nm NFO/Si + 700C	100nm NFO/Si	100nm NFO/Si + 650C	100nm NFO/Si + 750C	23nm CFO/Pt	35nm CFO/Pt	66nm CFO/Pt
0	1	1.13	1.04	0.26	0.73	1.05	0.90	0.94	1.05
0	1.45	0.91	1.90	0.25	0.94	0.86	1.26	1.04	0.96
400	1	8.34	8.23	3.35	10.13	13.52	5.86	8.83	4.42
400	1.45	12.07	12.54	4.93	14.50	19.51	8.10	11.84	6.08
800	1	16.69	18.32	6.76	20.51	26.67	11.53	16.18	8.17
800	1.45	24.01	27.13	10.04	30.24	39.55	17.27	23.03	11.63
1200	1	25.07	28.35	10.31	30.73	41.16	18.30	26.74	12.10
1200	1.45	36.01	41.44	15.04	45.64	59.45	27.27	42.00	17.62
1600	1	32.86	38.74	13.91	41.36	55.32	26.28	37.28	16.17
1600	1.45	48.02	56.68	20.36	60.16	80.55	39.87	53.96	23.33
2000	1	40.79	48.75	17.49	51.91	70.15	35.78	45.50	20.03
2000	1.45	60.50	72.05	25.42	76.28	102.15	52.81	64.08	28.92
2400	1	46.92	58.98	20.97	62.91	85.94	44.52	53.63	23.08
2400	1.45	68.32	87.31	30.84	91.67	122.23	67.08	73.90	32.29
2800	1	54.53	70.16	24.59	73.06	101.34	54.22	61.85	24.95
2800	1.45	79.90	105.45	36.16	106.57	145.64	82.71	84.03	37.12
3200	1	60.60	80.85	27.67	81.40	108.56	64.45	67.54	27.90
3200	1.45	89.11	119.62	40.92	119.38	167.09	97.07	90.98	41.98
3600	1	67.06	91.28	31.44	91.45	124.38	75.57	74.84	32.30
3600	1.45	99.93	138.91	46.41	135.33	190.46	117.14	100.34	48.31
4000	1	74.48	102.78	35.07	102.45	138.17	88.51	82.37	36.30
4000	1.45	112.36	158.23	52.05	151.22	212.07	133.83	109.69	55.05
4400	1	81.66	116.41	38.97	113.48	153.31	103.19	90.06	40.96
4400	1.45	124.35	180.87	57.85	168.30	228.87	152.31	118.70	62.08
4800	1	90.70	131.82	42.84	124.72	174.02	116.96	98.40	46.19
4800	1.45	139.91	200.17	63.84	186.92	252.41	169.56	128.93	72.58
5200	1	99.24	150.11	46.67	136.58	192.00	132.44	105.14	51.37
5200	1.45	157.12	216.97	70.78	207.06	276.94	188.55	139.17	85.26
5600	1	109.61	163.69	51.09	147.47	214.00	148.46	114.44	55.56
5600	1.45	175.23	240.71	72.73	231.44	295.94	215.72	149.13	91.60
6000	1	120.12	188.95	55.94	159.32	233.73	161.66	121.59	59.94
6000	1.45	190.21	262.00	76.31	241.13	320.28	228.36	159.57	98.57

Pictorially, the displacement for one of the samples, 66nm CFO on platinized Si, is shown below for 1Oe (AC1) and 1.45Oe (AC2) AC magnetic excitation at 1kHz in 4 sets of 4 DC magnetic biases.

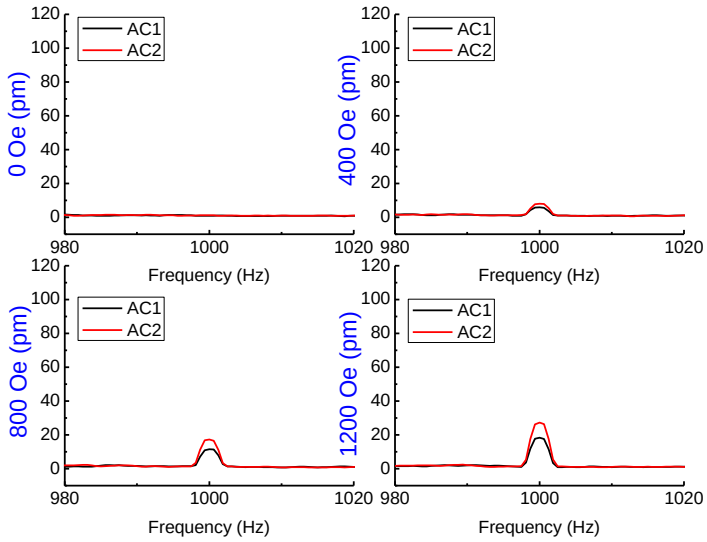

a)

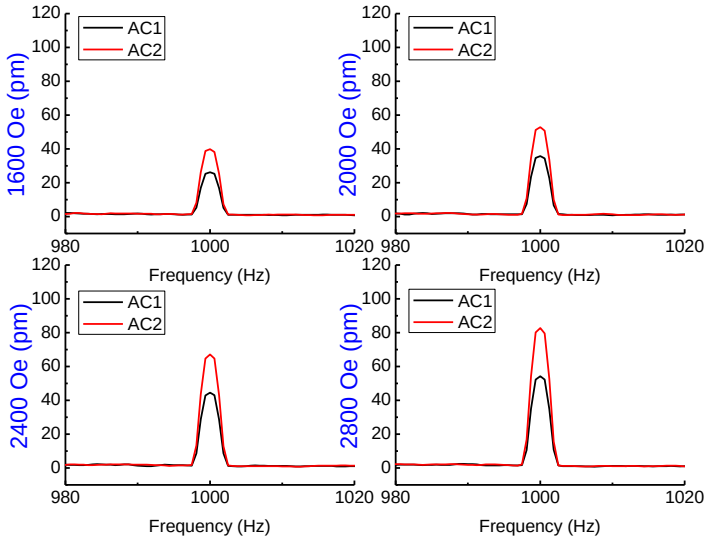

b)

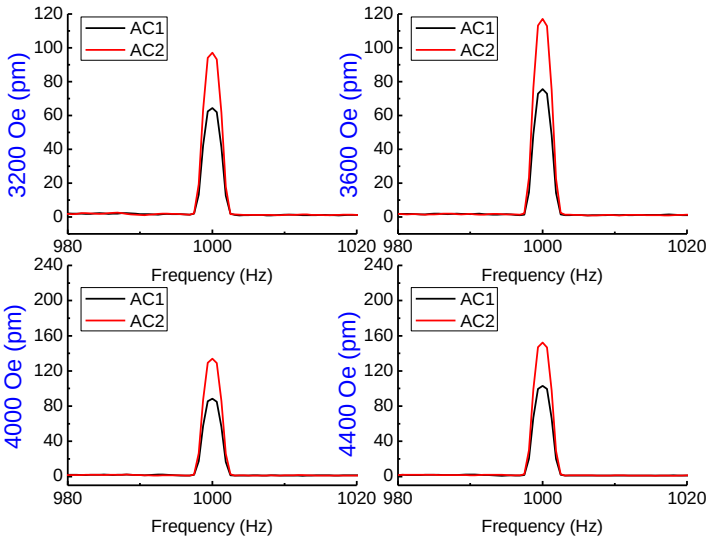

c)

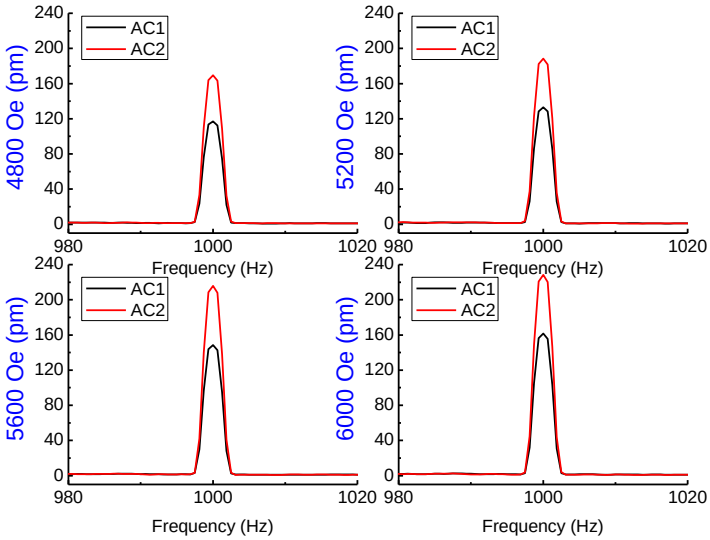

d)

Figure 4.5 Displacement vs. frequency for 1Oe (AC1) and 1.45Oe (AC2) for the 66nm CFO thin film on platinized Si at DC bias of a) 0-1200 Oe b) 1600-2800 Oe c) 3200-4400 Oe and d) 4800-6000 Oe.

The data in Table 4.1 was processed by using Eqns. (1)-(5) to generate the magnetostriction results shown below:

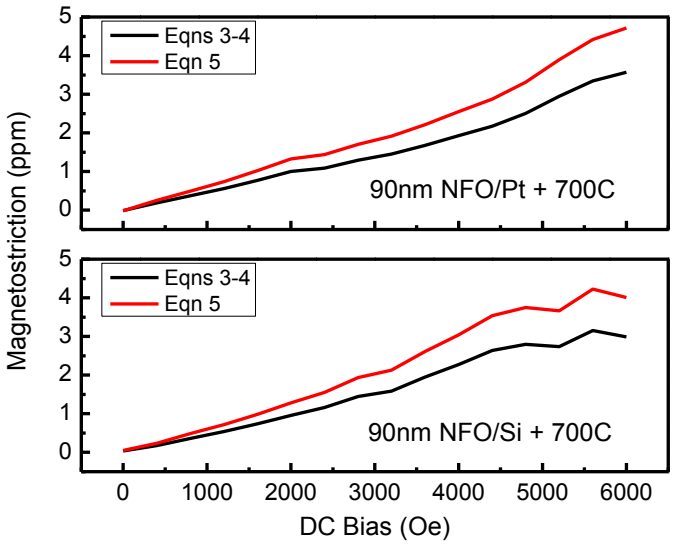
Eqns 3-4
Eqn 5
90nm NFO/Pt + 700C
Eqns 3-4
Eqn 5
90nm NFO/Si + 700C
Magnetostriction (ppm)
DC Bias (Oe)

a)

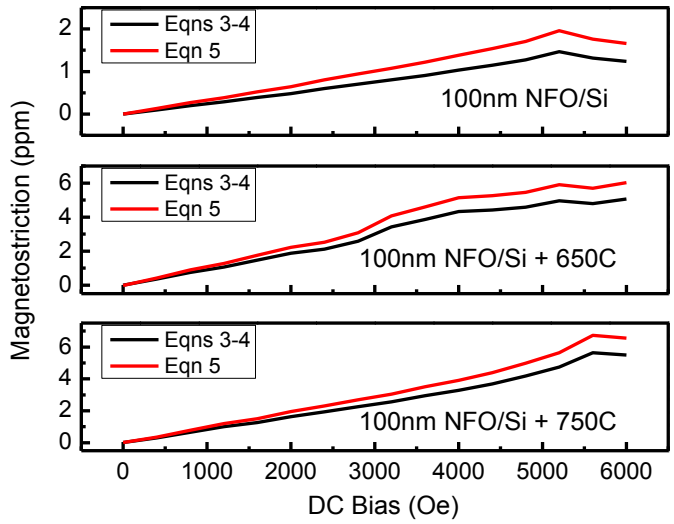
Eqns 3-4
Eqn 5
100nm NFO/Si
Eqns 3-4
Eqn 5
100nm NFO/Si + 650C
Eqns 3-4
Eqn 5
100nm NFO/Si + 750C
Magnetostriction (ppm)
DC Bias (Oe)

b)

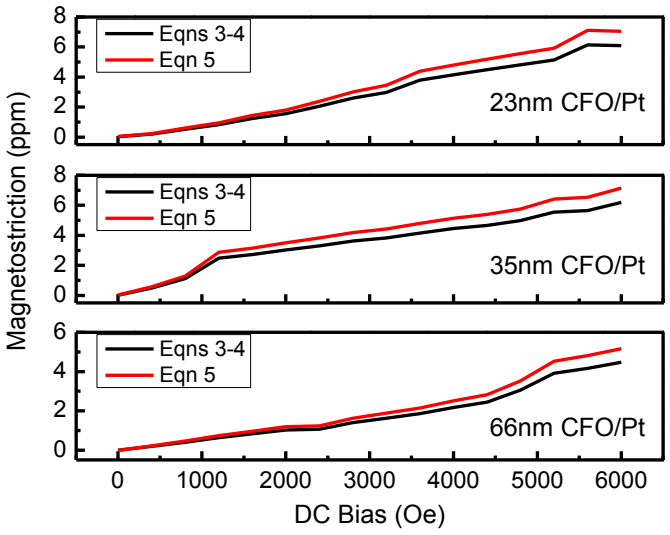

c)

Figure 4.6 Magnetostriction (λ) calculated using equations 3-4 and 5 for a) NFO on Si vs.Platinized Si b) NFO on Si as-deposited, after 650C and 750C anneal and c) CFO on Platinized Si

Discussion

The Magnetostriction data calculated using equations 3-4 and 5 are almost similar with that from the latter predicting slightly higher values. Magnetization (M) – Magnetic Field(H) hysteresis loops were measured in the longitudinal direction using VSM (Table 4.3) to determine the remnant magnetization (M_r), coercive magnetic field (H_c), saturation magnetic field (H_{sat}) and saturation magnetization (M_{sat}). The applied DC bias, H_{DC}, of 0-6000 Oe during λ measurement, did not cause the thin films to reach saturation magnetization. Single crystal Si is considered diamagnetic whilst Pt thin film is paramagnetic. For the soft magnetic NFO films deposited on Si and platinized Si respectively, the M_r and H_c is higher on Si whilst H_{sat} and M_{sat} is lower. The magnitude of parameters M_r , H_{sat} and M_{sat} increases slightly with annealing

temperature due to higher degree of crystallization and grain growth. In the case of hard magnetic CFO thin films, the parameters M_r , H_c , H_{sat} and M_{sat} increase with CFO thickness.

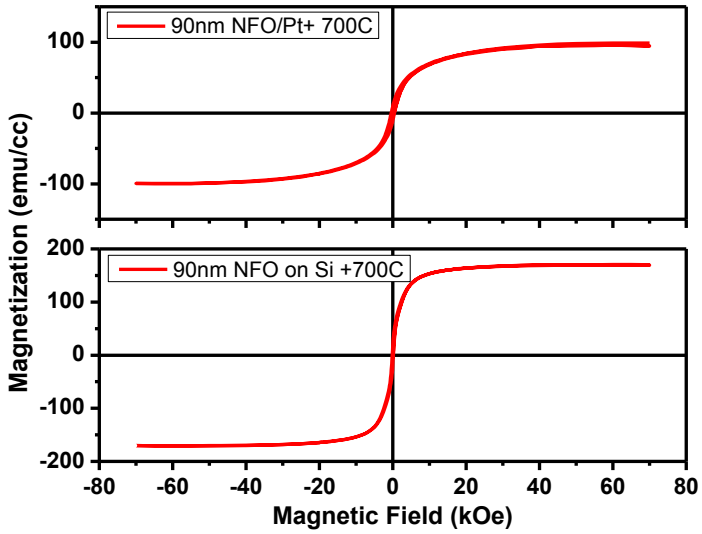

a)

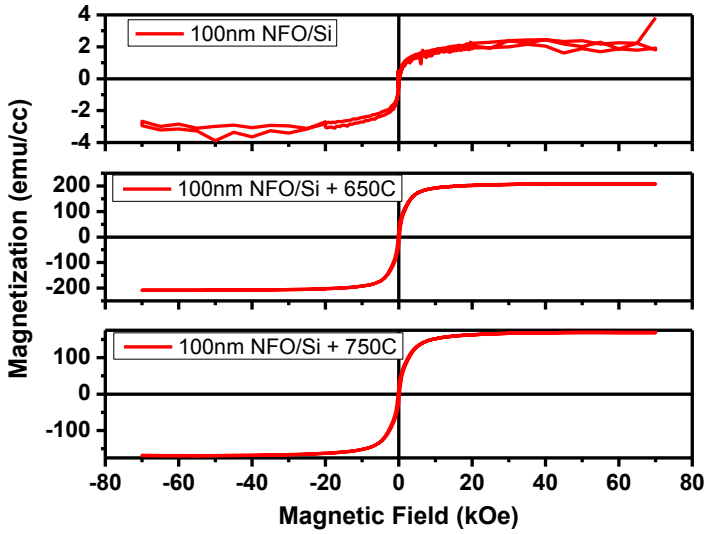

b)

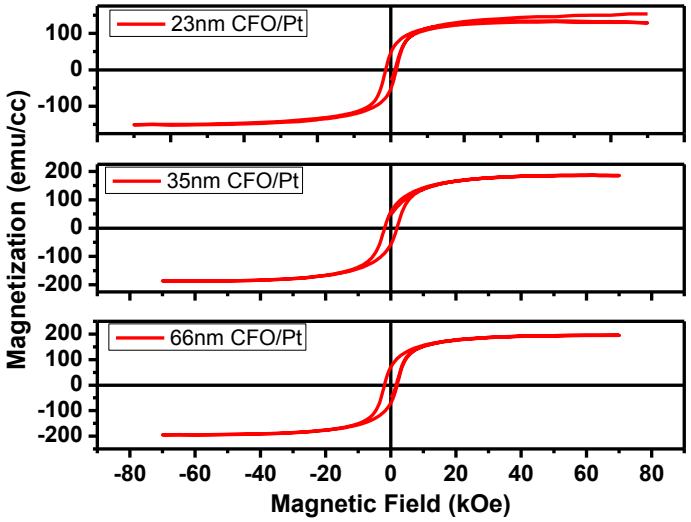

c)

Figure 4.7 M-H hysteresis loops for a) NFO on Si vs.Platinized Si b) NFO on Si as-deposited, after 650C and 750C anneal and c) CFO on Platinized Si

Table 4.2 Hysteresis loop data obtained from VSM measurement for NFO and CFO thin film samples.

	M_r (emu/cc)	H_c(Oe)	H_{sat}(kOe)	M_{sat} (emu/cc)
90nm NFO/Pt + 700C	10.54	463.00	55.32	96.19
90nm NFO/Si + 700C	19.70	165.50	39.74	33.95
100nm NFO/Si	-	-	38.74	4.952
100nm NFO/Si + 650C	18.79	189.50	42.13	33.728
100nm NFO/Si + 750C	28.55	187.50	49.76	41.694
23nm CFO/Pt	49.47	1453.00	44.40	134.14
35nm CFO/Pt	57.05	1911.00	54.67	185.75
66nm CFO/Pt	70.24	1944.50	69.50	195.70

NFO magnetostriction data mostly match the trends observed in its M-H data. NFO films on Platinized Si have higher λ (and high M_{sat}) whilst for films on Si, the annealing temperature in the range of 650-750 °C causes a small proportional increase in magnetostriction and magnetization properties. Magnetostriction λ of CFO decreases with thickness but M-H properties as measured by VSM increase (as shown in table above). CFO has been known to

possess both large magnetic anisotropy and large anisotropic magnetostriction [19]. Saturation magnetization should be a constant because it is the property of a material. If it is changing for different thickness it might be that the saturation fields are different. This may occur due to film defects and substrate clamping of domains. However remnant magnetization can change with total magnetic anisotropy. From X-ray diffraction studies (shown below), it was found that the NFO films are slightly textured on Si and platinized Si but NFO texturing improves by 50% with annealing temperature. For CFO, the texturing improves with thickness, where films with >35nm were found to reach same degree of 20% texturing with annealing. So the λ values in the films studied here are expected to be lower than that for fully textured or epitaxial films. Prior results on CFO have shown a λ_{sat} of 110ppm [20] whilst that for NFO the magnitude reaches up to 26ppm [21].

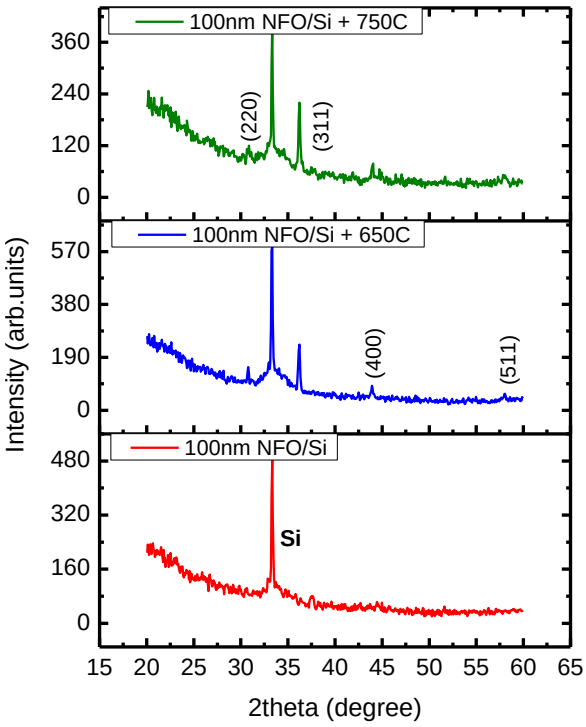

a)

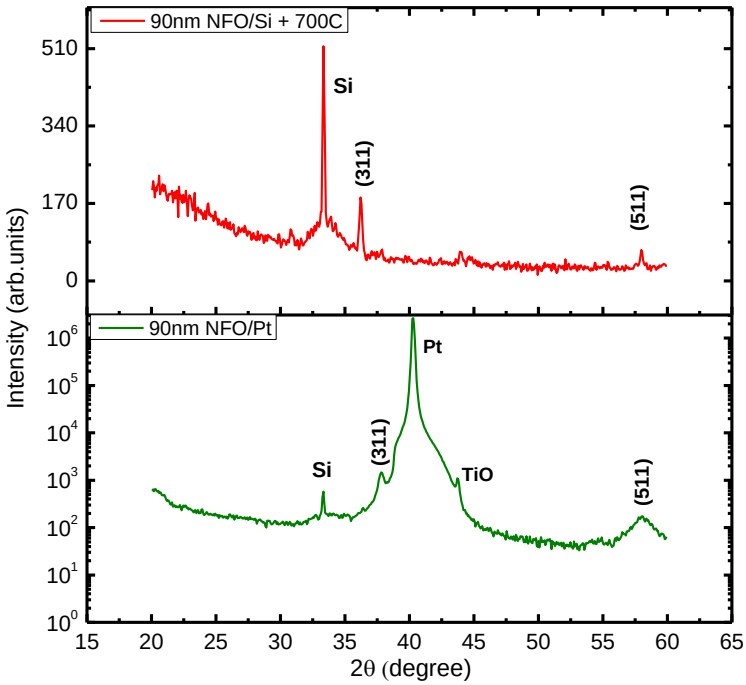

b)

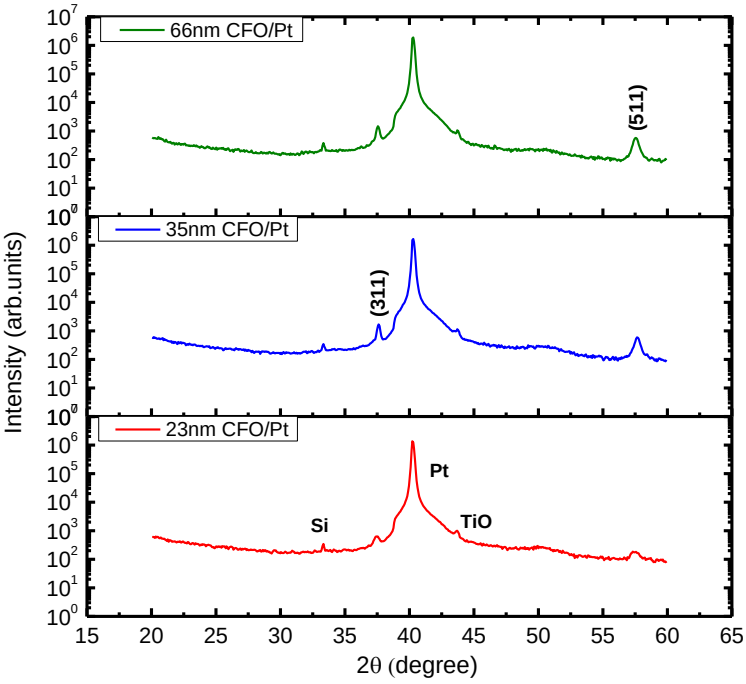

c)

Figure 4.8 XRD plots for a) NFO on Si vs. annealing temperature b) NFO on Si vs. Platinized Si c) CFO on Platinized Si vs. Thickness

The magnetostriction measurement technique presented here is highly dependent on the mechanical constants for the film and substrate utilized in equations (3-4). The Young's modulus of silicon can vary in the range of 1.25-2.02 $x10^{11}$ N/m^2 based on the crystalline orientation of wafer and doping [22]. In the calculations reported here, the modulus value of $1.69x10^{11}$ N/m^2 for a silicon (100) wafer was used with the axis of bending along [110] direction [23]. The magnetization of a magnetostrictive thin film can be derived from the radius of curvature induced by the magnetic moment (magnetization x volume) applied by a magnetic field [5, 7] as:

$$m = \frac{Y_s t_s^3 b}{12RB} \qquad (6)$$

Substituting the radius of curvature calculated using Eqn. (1) in the above equation and comparing the resultant magnetic moment values to the M-H VSM data a baseline can be established However, the above equation was derived for the torque created due to an AC field perpendicular to a DC magnetic field (perpendicular mode). For the parallel mode configuration, as both the ac and dc fields are applied parallel to the length of the sample, there will be equal and opposite torques at the ends of the sample in a direction perpendicular to the sample and along its width.

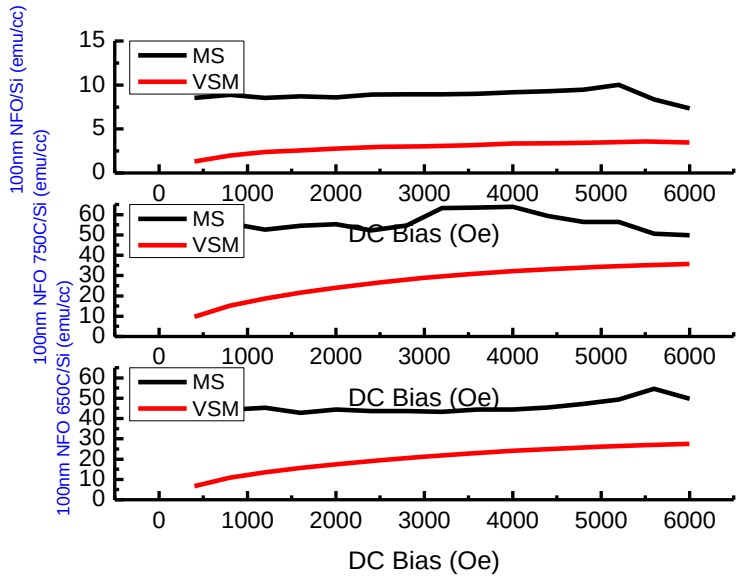
100nm NFO/Si (emu/cc)
MS
VSM
100nm NFO 750C/Si (emu/cc)
DC Bias (Oe)
100nm NFO 650C/Si (emu/cc)
DC Bias (Oe)

a)

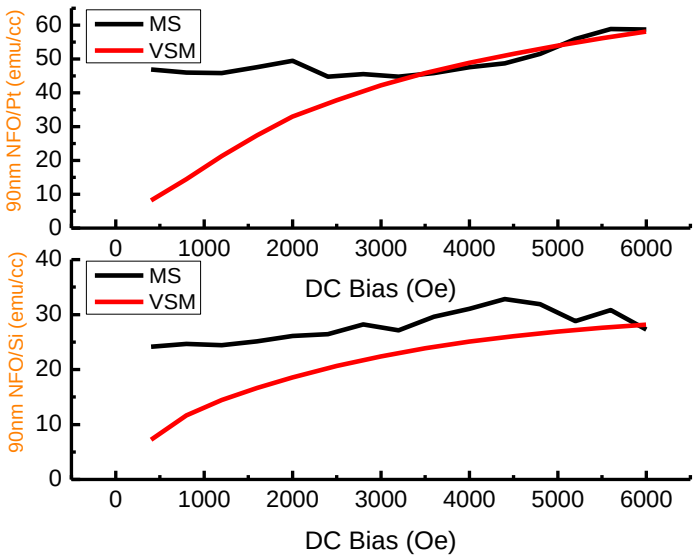
90nm NFO/Pt (emu/cc)
MS
VSM
90nm NFO/Si (emu/cc)
DC Bias (Oe)

b)

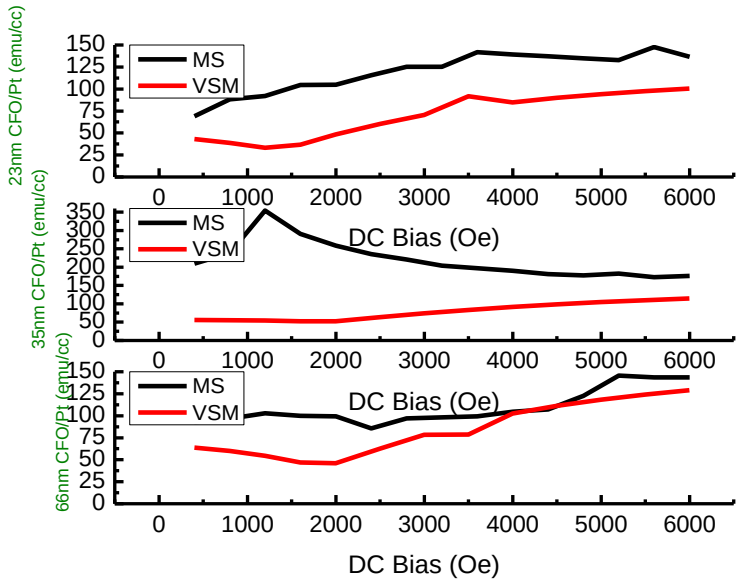

c)

Figure 4.9 Magnetization vs. magnetic field plot showing the comparison between the calculated values using Eqn. (6) and that determined from M-H loop: a) NFO on Si vs. annealing temperature b) NFO on Si vs. Pt c) CFO on Pt vs. Thickness

Evidently, in almost all cases, the magnetization calculated using Equation (6) is over predicting that measured using VSM. Nonetheless, the curves seem to be converging or are closer to each other with increase in DC bias. In parallel mode, the magnetic field applied to the sample can be considered as a DC field that varies between DC-AC, DC and DC+AC magnitudes. Therefore with higher DC bias, the thin film magnetic domains, which are constrained into out-of-plane anisotropy, align better at fields much greater than their coercive fields leading to the higher magnetic moment. Thereby, at high DC bias fields, torque derived magnetic moment trends closer to that from VSM measurements.

Conclusion

Magnetostriction of magnetic thin films cannot be accurately measured using same methods as that utilized for bulk magnetic material. We have developed laser doppler vibrometry based

technique to measure the picometer level deflections occurring in square-shaped magnetostrictive thin films deposited on Si and platinized Si substrates. We disclose the precautions necessary to make such delicate measurements especially the isolation required between the 3 components of the measurements setup, namely, sample, laser and magnetic coils. We corroborate our approach by comparing the magnetization calculated from the radius of curvature induced by the magnetically induced torque on the sample vs. that measured by a VSM system. This non-contact technique can provide advantages in routine optimization of the magnetostrictive composition.

Acknowledgements: The authors gratefully acknowledge the financial support from ***Air Force Office of Scientific Research (AFOSR)*** *through Young Investigator Program.* We would like to thank Greg Pribil of J. A. Woollam Inc. for help with modeling of the thin film VASE data. We are also greatly indebted to CEHMS colleagues Justin Farmer and SuChul Yang for assistance with the experimental setup.

References

[1] Ekreem NB, Olabi AG, Prescott T, Rafferty A, Hashmi MSJ. An overview of magnetostriction, its use and methods to measure these properties. Journal of Materials Processing Technology 2007;191:96.
[2] Grössinger R, Sassik H, Holzer D, Pillmayr N. Accurate measurement of the magnetostriction of soft magnetic material. Proc. 1&2—Dimensional Magnetic Measurement and Testing 2000:35.
[3] Raghunathan A, Snyder JE, Jiles DC. Comparison of Alternative Techniques for Characterizing Magnetostriction and Inverse Magnetostriction in Magnetic Thin Films. Magnetics, IEEE Transactions on 2009;45:3269.
[4] Marcus PM. Magnetostrictive bending of a cantilevered film-substrate system. Journal of Magnetism and Magnetic Materials 1997;168:18.
[5] Sander D, Enders A, Kirschner J. Magnetization, magnetostriction and film stress of Fe monolayers on W(100). Magnetics, IEEE Transactions on 1998;34:2015.

[6] du Trémolet de Lacheisserie E, Peuzin JC. Magnetostriction and internal stresses in thin films: the cantilever method revisited. Journal of Magnetism and Magnetic Materials 1994;136:189.
[7] Weber M, Koch R, Rieder KH. UHV Cantilever Beam Technique for Quantitative Measurements of Magnetization, Magnetostriction, and Intrinsic Stress of Ultrathin Magnetic Films. Physical Review Letters 1994;73:1166.
[8] Bellesis GH, Harlee PS, III, Renema A, II, Lambeth DN. Magnetostriction measurement by interferometry. Magnetics, IEEE Transactions on 1993;29:2989.
[9] Tam AC, Schroeder H. A new high-precision optical technique to measure magnetostriction of a thin magnetic film deposited on a substrate. Magnetics, IEEE Transactions on 1989;25:2629.
[10] Adhikari R, Kaundal R, Sarkar A, Rana P, K. Das A. The cantilever beam magnetometer: A simple teaching tool for magnetic characterization. American Journal of Physics 2012;80:225.
[11] Adhikari R, Sarkar A, Das AK. A versatile cantilever beam magnetometer for ex situ characterization of magnetic materials. Review of Scientific Instruments 2012;83:013903.
[12] Castellini P, Martarelli M, Tomasini EP. Laser Doppler Vibrometry: Development of advanced solutions answering to technology's needs. Mechanical Systems and Signal Processing 2006;20:1265.
[13] Nakata T, Takahashi N, Nakano M, Muramatsu K, Miyake P. Magnetostriction measurements with a laser Doppler velocimeter. Magnetics, IEEE Transactions on 1994;30:4563.
[14] www.polytec.com.
[15] Roozen NB, Koevoets AH, den Hamer AJ. Active Vibration Control of Gradient Coils to Reduce Acoustic Noise of MRI Systems. Mechatronics, IEEE/ASME Transactions on 2008;13:325.
[16] http://en.wikipedia.org/wiki/Coil_noise.
[17] Ohring M. Materials science of thin films : deposition and structure. San Diego, CA: Academic Press, 2002.
[18] van de Riet E. Deflection of a substrate induced by an anisotropic thin-film stress. Journal of Applied Physics 1994;76:584.
[19] Hu G. Structural tuning of the magnetic behavior in spinel-structure ferrite thin films. Physical review. B, Condensed matter 2000;62:R779.
[20] O'Handley RC. Magnetostrictive Materials and Magnetic Shape Memory Materials. Handbook of Magnetism and Advanced Magnetic Materials. John Wiley & Sons, Ltd, 2007.
[21] Cullity BD, Graham CD. Soft Magnetic Materials. Introduction to Magnetic Materials. John Wiley & Sons, Inc., 2008. p.439.
[22] p.http://www.memsnet.org/material/siliconsibulk/.
[23] Fang H-B, Liu J-Q, Xu Z-Y, Dong L, Wang L, Chen D, Cai B-C, Liu Y. Fabrication and performance of MEMS-based piezoelectric power generator for vibration energy harvesting. Microelectronics Journal 2006;37:1280.

Chapter 5

Thermal Transport in Textured Lead Zirconate Titanate Thin Films

Ronnie Varghese[a], Hari Harikrishna[b], Scott T. Huxtable[c], W. T. Reynolds Jr.[a] and Shashank Priya[d]

[a] *Department of Materials Science, Virginia Tech, Blacksburg, Virginia, 24061, USA*

[b] *Department of Engineering Science and Mechanics, Virginia Tech, Blacksburg, Virginia, 24061, USA*

[c] *Department of Mechanical Engineering, Virginia Tech, Blacksburg, Virginia, 24061, USA*

[d] *Center for Energy Harvesting Materials and Systems (CEHMS), Bio-inspired Materials and Devices Laboratory (BMDL), Virginia Tech, Blacksburg, Virginia, 24061, USA*

Abstract

We use Time Domain Thermoreflectance (TDTR) to characterize a series of textured $Pb(Zr,Ti)O_3$ (PZT) thin films grown by a sol gel process on platinized silicon substrates. These PZT films have preferred crystallographic orientations of (100), (110), and (111) which we control by manipulating the heterogeneous nucleation and growth characteristics at the interface between the film and the underlying Pt layer on the substrate. TDTR was used to measure both the PZT film thermal conductivity and the interface thermal conductance between the PZT and Pt as well as that between the PZT and an Al thermoreflectance layer evaporated on the PZT surface. We find that thermal conductivity and interface thermal conductance have a slight dependence on crystal orientation. Thus with our nanoscale thermal measurements we can discriminate between PZT samples of different crystallographic orientations.. The thermal conductivities of the PZT films with different crystal orientations are in the range of 1.45 - 1.70

W m^{-1} K^{-1}. The interface thermal conductance between the PZT and Pt layer ranges from 40 - 65 MW m^{-2} K^{-1}, while the conductance between the Al thermoreflectance layer and PZT is ~100 MW m^{-2} K^{-1}.

Keywords: Thin films; thermal conductivity; thermal conductance; Interface properties; texturing

Introduction

Crystallographic texturing of $Pb(Zr,Ti)O_3$ (PZT) thin films on platinized Si substrates ($Pt/Ti/SiO_2/Si$) has been studied extensively and various mechanisms related to the origin of the preferred orientation have been proposed in the literature [1-9]. The single most important factor for the nucleation and growth of a preferentially oriented PZT film is the interaction of the PZT precursors with the top layer of the substrate, namely Pt in case of a platinized silicon substrate. The boundary conditions at the PZT-Pt interface determine the overall degree of texturing that can be achieved in the PZT films. Prior research has investigated the role of interfacial transient phases of an intermetallic Pt-Pb [1, 3, 5], pyrochlore $Pb_2(Zr,Ti)_2O_6$ [5-7], permanent buffer or seed layers of $PbTiO_3$ [2, 4, 8], TiO_2 [9], ZrO_2 [9], and PbO [1] concentration gradients on the evolution of texture. However, the deterministic criterion controlling the magnitude of texture degree remains a debatable subject.

In a prior study, we characterized the phase and orientation of sol-gel derived $Pb(Zr_{0.6}Ti_{0.4})O_3$ thin films and developed the Temperature-Time-Transformation (TTT) diagrams illustrating the correlation between the synthesis parameters and Lotgering factor. Analytical models were developed to utilize the TTT diagrams effectively [10]. However, the earlier study's focus was not the investigation of the interfacial heterogeneity in the PZT films that could shed

light on the mechanism responsible for development of texture. Various characterization techniques with increasing sensitivity including optical (Ellipsometry and Raman) characterization, high resolution binding energy X-ray photoelectron spectroscopy depth profile scans, and High Resolution Transmission Electron Microscopy (HR-TEM) were utilized to study the interface between PZT and Pt, but nothing significant was found. Building upon the prior work, here we use an optical technique called Time Domain Thermoreflectance (TDTR) to measure the interface thermal conductance, *G*, between the textured PZT films and the underlying Pt layer, along with the interface thermal conductance between the PZT and an Al layer that is evaporated on the PZT films. We also use TDTR to simultaneously extract the thermal conductivity, *k*, of the textured PZT films. The variation in the magnitude of thermal conductance could be utilized for inferring the structural changes occurring at the interface.

Hopkins et al. [11] used TDTR to examine the thermal conductance at Al/Si and Al/sapphire interfaces with different Si and sapphire substrate orientations. They found that the interface thermal conductance for the sapphire samples (trigonal unit cell) showed a strong dependence on the crystal orientation while that was not the case with silicon samples (diamond cubic unit cell). The interface thermal conductance dependence on the crystal orientation in the Al/sapphire samples was attributed to the anisotropy in the Brillouin zone and subsequent changes in the phonon velocities with crystallographic direction in the sapphire. Costescu et al. [12] also used TDTR to measure the interface thermal conductance of TiN:MgO (001) and TiN:MgO (111), and they found no dependence on crystallographic orientation. More recently, Duda et al. [13] used classical molecular dynamics simulations to study the influence of crystallographic orientation on interface thermal conductance. They found that the thermal conductance at interfaces between two cubic materials was independent of crystallographic

orientation, while the conductance between a face centered cubic material and a tetragonal material had a dependence on orientation.

With TDTR we find a slight dependence on the thermal conductivity with the crystallographic orientation of the PZT films and observe differences in the interface thermal conductance between the PZT and Pt for varying degree of preferred orientations (100), (110), and (111). However, we do not observe a strong correlation between the interface thermal conductance and the preferred orientation.

Sample Preparation and Characterization

The PZT thin film (Zr/Ti = 60/40) samples were synthesized by sol-gel processing as described in detail elsewhere [10]. With this technique, a series of films were synthesized and crystallized to achieve varying percentages of crystallographic orientations (111), (110), and (100). The crystallographic orientation and thickness of the samples was determined by X-ray diffraction (Phillips Xpert Pro) and Variable Angle Spectroscopic Ellipsometry (J.A. Woollam), respectively. All of the samples had a rhombohedral crystal structure at room temperature. Transmission electron microscopy (TEM) was performed with an FEI Titan 300. Samples for TEM were prepared using a focused ion beam from an FEI Helios 600 NanoLab. Raman spectra was collected using a Jobin-Yvon T6400 Triplemate with 514.5 nm radiation. GI-XRD data was collected on a Bruker D8 Advance system with an incident Goebel mirror having a 4 degree Soller slit and 0.6mm exit slit. The diffracted beam side of the diffractometer was equipped with an equatorial Soller slit (0.2 degree divergence) and LynxEye detector in 0d mode. Data was collected using 2 theta scans with fixed grazing incidence (either 4 or 6 degree incident angle).

The measurement parameters were 0.04 degree steps and either 10 sec per step (4 hours scans) or 2 sec per step (50 minute scans for confirmation).

Experimental Measurements with TDTR

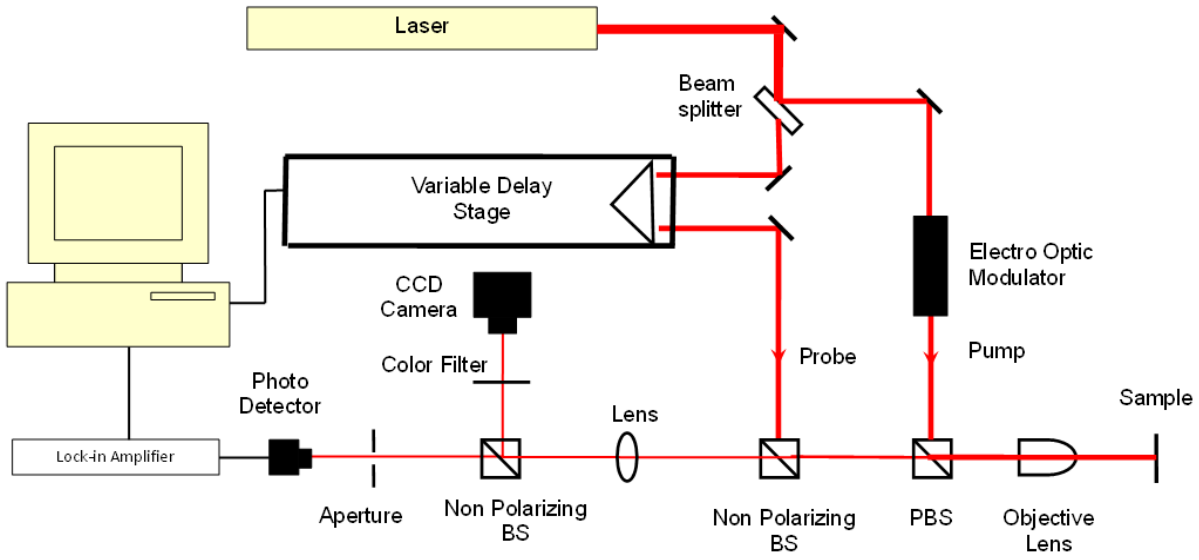

Figure 5.1 Schematic diagram of the TDTR system. The pump beam heats the surface of the sample and the time-delayed probe beam monitors changes in temperature at the sample surface. Thermal conductivity and interface thermal conductance are extracted by comparing the experimental data with an analytical thermal model.

Time-Domain Thermoreflectance (TDTR) [14-16], as shown in Figure 5.1, relies on the fact that the reflectivity of some metals has a small, but measurable, dependence on the temperature. We use a Ti:Sapphire mode-locked to produce a series of ~100 fs optical pulses with a wavelength of 800 nm at a repetition rate of 80 MHz. These laser pulses are then split into two separate beams, which are referred to as the "pump" and "probe" beams. The pump beam is modulated at 10 MHz using an electro-optic modulator and this beam is used to heat the sample. The surface of the sample is coated with a thin layer of aluminum, as Al exhibits a relatively

large change in reflectivity with temperature at 800 nm.[17] The probe beam is focused to the same location on the sample as the pump, and the reflected probe beam is directed to the photo detector. Thus the intensity of the reflected probe beam is proportional to the surface temperature. A lock-in-amplifier then records the in-phase (V_{in}) and out-of-phase voltages (V_{out}) from the photo detector. The arrival time of the probe beam at the sample is controlled with a mechanical delay stage. The system can measure the thermal decay of a sample with picosecond time resolution for delay times up to 3 ns. The $1/e^2$ diameters of the pump and probe beam are ~ 25 μm. Since the penetration depth of the thermal wave is much smaller than the diameters of the pump and probe beams, the heat flow is predominantly one-dimensional and the measured thermal conductivity is in the direction normal to the sample surface.

Table 5.1: Composition, orientation and dimension information for the synthesized samples.

Al	*Thickness (nm)*	30
PZT	*Sample*	$PbZr_{0.6}Ti_{0.4}O_3$
	Orientation	(100), (110), (111)
	Thickness (nm)	60-80
Pt	*Orientation*	(111)
	Thickness (nm)	150
Ti	*Thickness (nm)*	10
SiO2	*Thickness (nm)*	300
Si	*Thickness (mm)*	0.5

We use the ratio of the in-phase and out-of-phase voltages to account for non-idealities such as the change in the pump-probe overlap or defocusing of the probe beam. Our experimentally measured ratio is then compared with an analytical thermal model of the layered sample structure.[18, 19] In short, the thermal model involves the solution to the heat diffusion

equation for the surface temperature of the sample under periodic heating. The unknown parameters (*k* and/or *G*) are adjusted until satisfactory matching is found between the model and the thermoreflectance measurements. The model requires the thickness, heat capacity, and thermal conductivity of each layer of the sample, and the details of the sample structure as given in Table 5.1. The thermal conductivities of the aluminum and platinum films were measured using the Wiedemann-Franz law and were found to be 180 W m^{-1} K^{-1} and 70 W $m^{-1}K^{-1}$, respectively. These values are reduced slightly from their bulk values, since the films are thin. The thermal conductivities of the titanium and oxide layers, and the heat capacities of all layers except PZT were taken to be the same as bulk values. The heat capacity of the PZT layer is assumed to be 2.4 MJ/(m^3-K) from our measurements of density and using specific heat measurements on similar PZT materials by Lang et al. [20]

With this sample configuration, we are initially left with five unknowns in the thermal model: the interface thermal conductance between aluminum and PZT, *G1*, the thermal conductivity of the PZT layer, k_{PZT}, the interface thermal conductance between PZT and platinum, *G2*, the interface thermal conductance between platinum and titanium, *G3*, and the interface thermal conductance between Ti and the oxide layer, *G4*. The interface thermal conductance at metal-metal interfaces is on the order of several hundred MW m^{-2} K^{-1}, beyond the range of the sensitivity of our measurements, thus we can ignore *G3* in our analysis.[21] To further reduce the number of unknowns, we examined a reference sample without the PZT layer and found the interface thermal conductance between titanium and the oxide layer, *G4*, to be ~110 MW m^{-2} K^{-1}. The remaining three remaining unknowns, *G1*, k_{PZT}, and *G2*, each affect the data in a unique manner. In the model, *G1* changes the radius of curvature below delay times of ~0.5 ns, while *G2* offsets the amplitude of the signal by an approximately constant value, and

k_{PZT} causes an offset at short delay times and changes the radius of curvature at longer delay times (~3 ns). This independence between the effects allows us to find a unique best fit even when we have multiple unknowns. Thus we find there is a unique combination of the three parameters that give the best fit between the model and the experimental data, as shown in Fig. 5.2. For each sample, we measured at least three different locations, and find agreement within 3% across each individual sample.

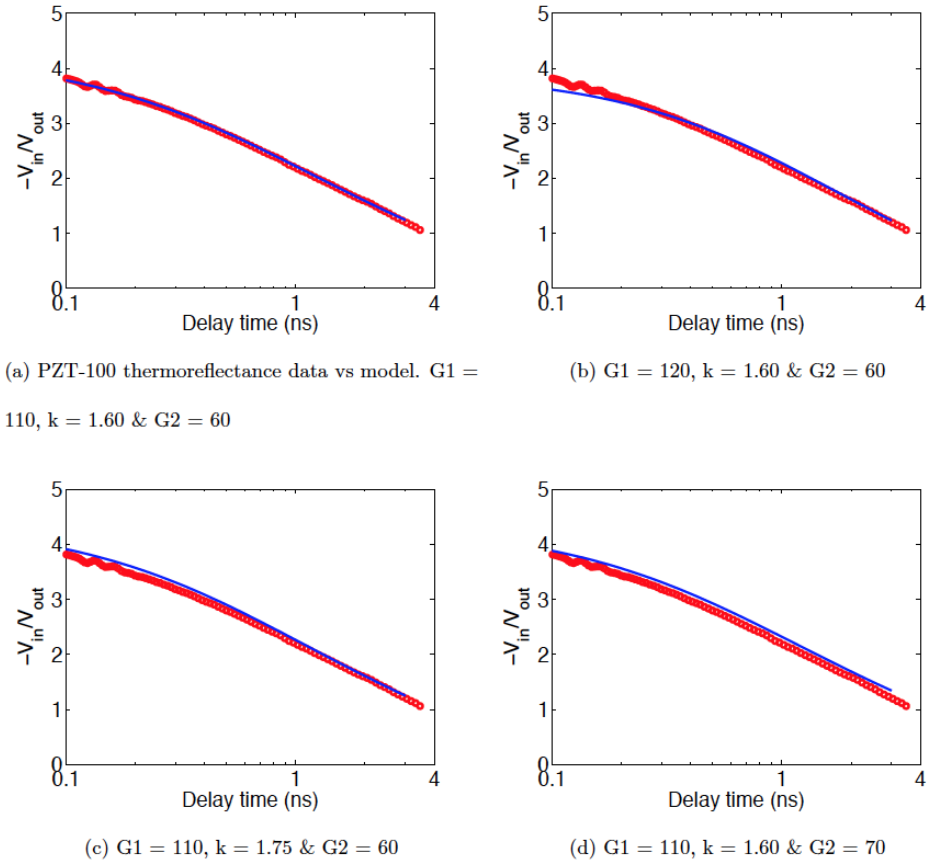

(a) PZT-100 thermoreflectance data vs model. G1 = 110, k = 1.60 & G2 = 60

(b) G1 = 120, k = 1.60 & G2 = 60

(c) G1 = 110, k = 1.75 & G2 = 60

(d) G1 = 110, k = 1.60 & G2 = 70

Figure 5.2 Sensitivity analysis. (a) The best fit with all three unknown parameters. (b) If *G1* is increased by less than 10% the fit is clearly poor at short delay times. (c) if *k* is increased by ~10%, the fit is clearly poor at short and intermediate times. (d) if *G2* is increased by ~15%, the fit is poor for all delay times.

Experimental Results

The pyrolysis and annealing temperatures and times along with the resulting texturing, i.e. the relative crystallographic orientations, of the sol-gel PZT thin films are summarized in Table 5.2.

Table 5.2 X-ray diffraction analysis results for the PZT samples

Sample No.	Pyrolysis Temperature (°C)	Pyrolysis Time (min)	Annealing Temperature (°C)	Annealing Time (min)	Orientation (100)	(110)	(111)
4D	250	1.5	625	60	**72%**	28%	0%
64	300	3	675	45	**77%**	23%	0%
67	300	3	725	30	**97%**	3%	0%
6A	300	3	775	15	**93%**	7%	0%
62	250	1.5	675	15	0%	9%	**91%**
72	250	1.5	800	60	0%	3 %	**97%**
76	250	1.5	750	60	0%	4%	**96 %**
4F	0	0	675	20	8%	**92%**	0%
7B	0	0	650	45	6%	**94%**	0%
81	0	0	800	45	0%	**100%**	0%
68	300	3	775	45	39%	20%	41%
7D	0	0	700	45	49%	1%	50%

An XPS depth profile showed decreasing amounts of Pb, Zr, Ti and O with depth whilst Pt increases with depth. Interestingly, because of surface roughness of the sputter crater created by the Argon sputter gas's unequal sputtering rate of elements in PZT, the Pt is detected at the surface and masks the Ti detection. Therefore the detection of an interfacial seeding layer was ruled out by this technique.

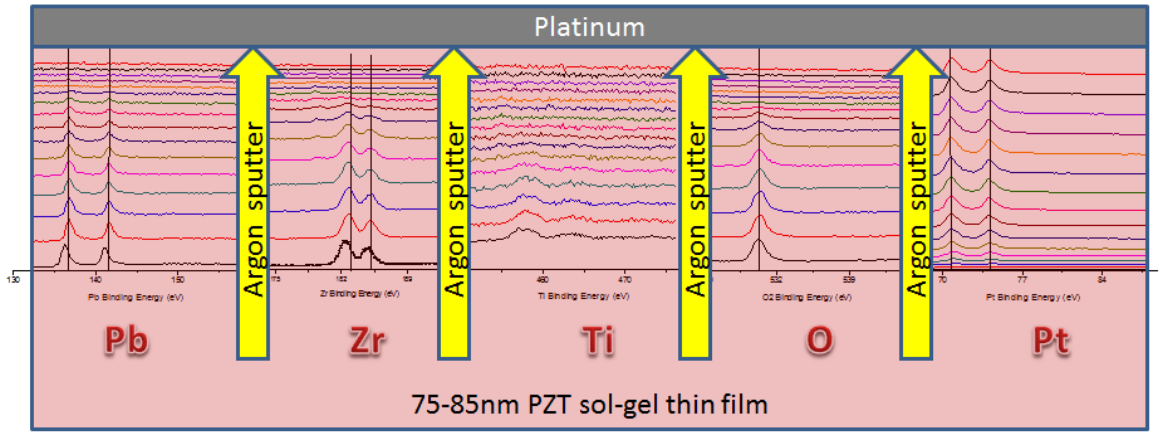

Figure 5.4 High Resolution Binding energy XPS depth profiling of a PZT sol-gel thin film

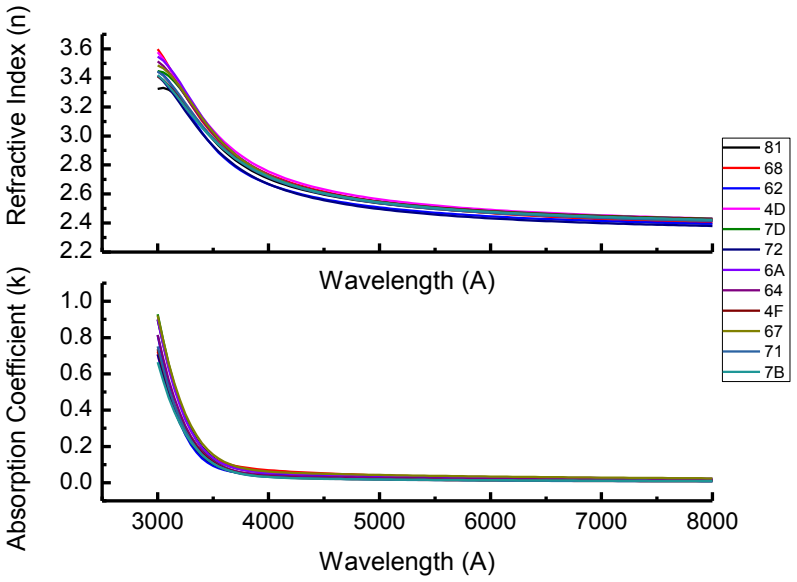

Figure 5.5 Optical dispersion data for all PZT samples used in this analysis

Variable Angle Spectroscopic Ellipsometry (VASE) provided the refractive index (n) and absorption coefficient (k) dispersion across a large range of spectrum 300-800 nm. As shown in Fig. 5.5, n & k does not discriminate much across the whole set of samples. Thus, optically we cannot detect an interfacial layer or discriminate with respect to crystallographic orientation.

Raman spectral analysis of three highly textured samples show minor differences only in A_1(2TO) mode which cannot be attributed to the crystallographic orientations[22]. Souza Filho et al. [22] observed that Raman spectra for rhombohedral compositions Zr = 0.54-0.6 were unchanged and had no distinguishing features.

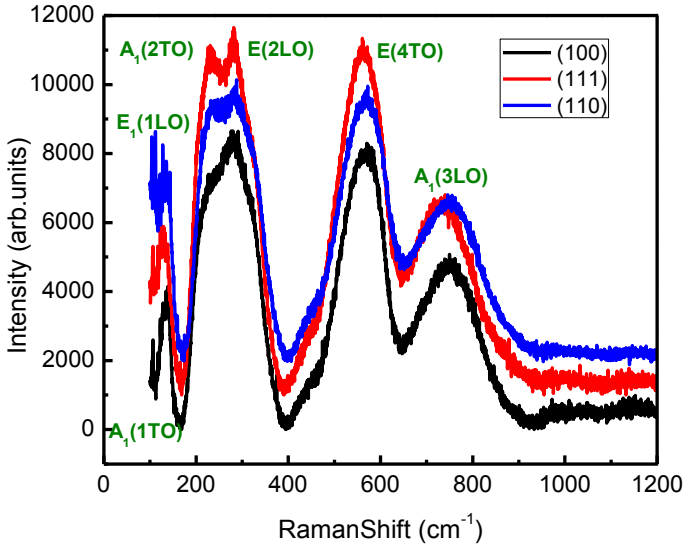

Figure 5.6 Raman shift data for the 3 highly textured PZT sol-gel thin films

Next, a highly textured (111) sample was used for high resolution TEM analysis. In the cross-sectional TEM micrograph shown in Fig. 5.7, an abrupt transition from Pt to PZT is evident but there is no discernible interfacial phase. No evidence was found for a seeding or intermetallic layer between Pt and PZT that could affect the evolution of texture in PZT films. However, the Energy Dispersive Spectroscopy (EDS) maps show that the interface between the PZT and Pt appears to be Ti rich and slightly Zr deficient.

a)

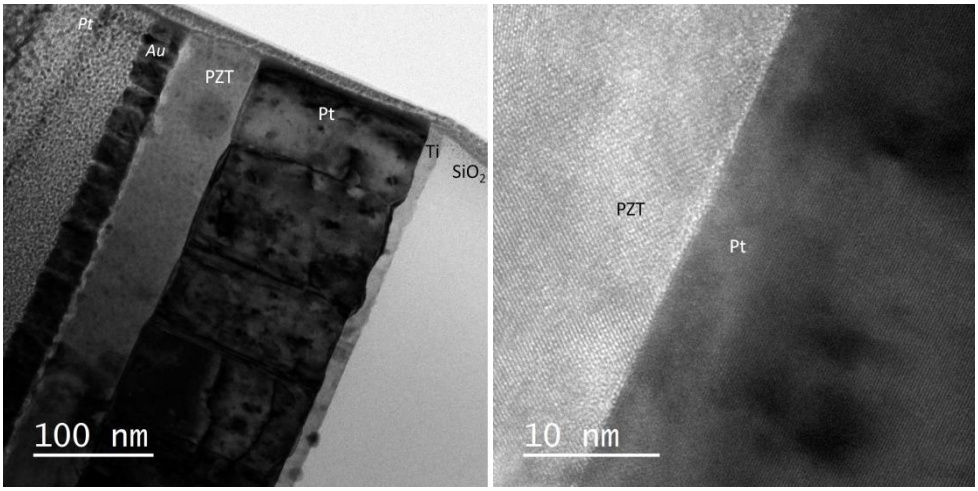

b)

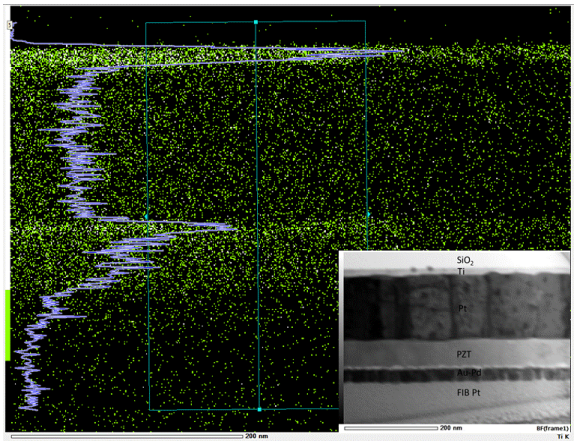

c)

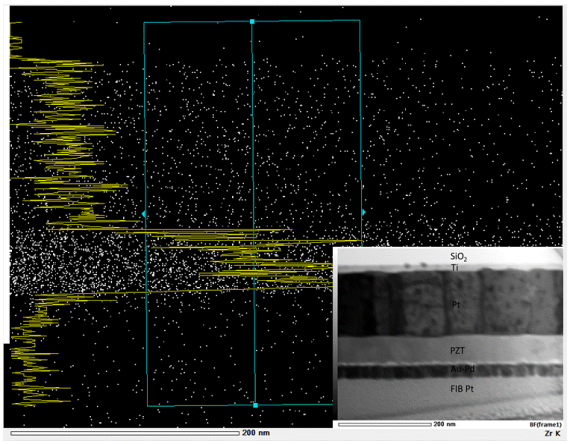

Figure 5.7 a) High resolution TEM of a highly textured PZT sol-gel thin film. The Au and Pt on the left side of the left panel were added to the sample during the lift-out process in preparation for the TEM. EDS maps showing b) Ti distribution and c) Zr distribution across the PZT-Pt interface.

TDTR measurements from the textured PZT samples listed in Table 5.2 were modeled as mentioned in last section to provide the results in Table 5.3.

Table 5.3 TDTR results from the PZT samples

Sample No.	Orientation (100)	(110)	(111)	$G_{Al\text{-}PZT}$ (MW/m^2-K)	k_{PZT} (W/m-K)	$G_{PZT\text{-}Pt}$ (MW/m^2-K)	G1/k	G2/k
4D	**72%**	28%	0%	110	1.60	50	68.75	31.25
64	**77%**	23%	0%	110	1.60	60	68.75	37.50
67	**97%**	3%	0%	110	1.65	60	66.67	36.36
6A	**93%**	7%	0%	110	1.65	60	66.67	36.36
62	0%	9%	**91%**	100	1.70	60	58.82	35.29
72	0%	3 %	**97%**	100	1.70	50	58.82	29.41
76	0%	4%	**96 %**	100	1.70	50	58.82	29.41
4F	8%	**92%**	0%	90	1.50	40	60.00	26.67
7B	6%	**94%**	0%	90	1.50	50	60.00	33.33
81	0%	**100%**	0%	100	1.45	45	68.97	31.03
68	39%	20%	41%	120	1.65	65	72.73	39.39
7D	49%	1%	50%	110	1.65	65	66.67	39.39

Discussion

Thermal conductivity, *k*, describes the ability of a material to transport heat, while the ability to transfer heat across an interface can be quantified in terms of an interface thermal conductance, *G*, which is simply the ratio of heat flux to the temperature drop across the interface. Typical values for *G* at metal/non-metal interfaces in intimate contact are often on the order of 10-100 MW $m^{-2} K^{-1}$, while metal-metal interfaces can have *G* approaching 1 GW $m^{-2} K^{-1}$ [21, 23] Electron transport dominates heat conduction in metals, while quantized lattice vibrations called phonons control heat conduction in non-metals.

Metal/metal interfaces have large interface thermal conductance due to good coupling of electrons across the interface, whereas, the weaker coupling between the electrons in a metal and

the phonons in a non-metal lead to lower interface thermal conductance at metal/non-metal interfaces. In the latter case, thermal energy can be transferred either by direct coupling between electrons in the metal and the phonons in the non-metal or via electron-phonon coupling within the metal followed by phonon-phonon coupling at the metal/non-metal interface.[24]

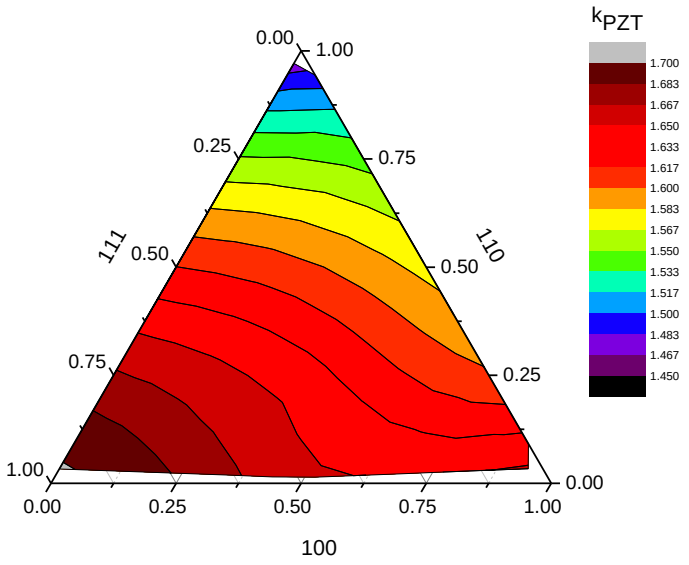

Figure 5.8 Ternary contour plot of thermal conductivity of PZT vs. crystallographic orientation

From the data in Table 5.2 and the ternary thermal conductivity plot shown in Fig. 5.8, we find that the thermal conductivity of all of the PZT samples fall within the range of 1.45 to 1.70 W m^{-1} K^{-1}. These thermal conductivity values are in line with other measurements on similar PZT materials in the literature. Kallaev et al. examined two types of PZT ceramics and found k ~ 1.35 for PKR-8 and k ~ 1.77 W/m-K for PKR-7M at 300 K. [25] Rivera-Ruedas et al. [26] prepared a series of PZT samples by mechanochemical activation of powder mixtures followed by thermal treatment. They found a larger range of thermal conductivity values with k

between 0.55 and 2.1 W/m-K at room temperature, and they observed no obvious trends in thermal conductivity with the composition of the PZT or Pb oxide source, and they attributed the range of thermal conductivity values to differences in microstructure and porosity. A variety of other crystalline perovskite ferroelectric materials, including $NaNbO_3$ and $Pb(Mg_{0.33}Nb_{0.67})O_3$ exhibit similar low thermal conductivity values in the 1 – 3 W/m-K range, while others (e.g. $BaTiO_3$, $KNbO_3$, $PbTiO_3$, and $KTaO_3$) have slightly larger conductivity in the range of 3-15 W/m-K at room temperature. [27, 28]

While the absolute error in the thermal conductivity values is estimated to be ~15%, the relative uncertainty between the samples should be considerably less. For example, much of the absolute error is a result of uncertainties in the Al and Pt film properties, and any errors in these values will affect all of the samples in the same manner (the Al films were evaporated on all of the samples simultaneously in one run, so we expect that the Al films on different samples will have nearly identical thickness). Finally, the small spread in results we obtain on samples with similar crystal orientations indicates the precision of our measurements.

However, we do observe that there is a ranking of the thermal conductivity with respect to the crystal orientation. The thermal conductivities of the samples that predominantly contain (111) are slightly greater than for the samples containing (100), which in turn, are greater than the (110) samples. The origin of this trend in thermal conductivity is unclear. One possible reason is the anisotropy of the rhombohedral lattice. If the thermal conductivity is significantly greater in a particular crystallographic direction, it could cause films of different textures to exhibit different average thermal conductivities. To confirm this hypothesis, it is necessary to infer the principal thermal conductivities from the textured films and show they conform to the rhombohedral symmetry constraint, $k11 \sim k22 < k33$. To do this, we assumed that the measured

thermal conductivity of each sample can be expressed as a weighted average of contributions from the three observed types of texture designated as k111, k100, and k110. That is, $k_{(PZT,\ sample)} = w_{111}\ k_{111},+ w_{100}\ k_{100} + w_{110}\ k_{110}$ where the 'w_{ijk}' represents the fractions of the corresponding crystal orientation in each sample. From the measured w_{ijk} values for all of the samples, best fit values were obtained for the thermal conductivities at end points, $k_{111} = 1.71$, $k_{100} = 1.65$ and $k_{110} = 1.48$. These values can be transformed to the principal coordinate system of the thermal conductivity (a second rank tensor property) to yield k_{11}, k_{22}, and k_{33}. The principal values of the thermal conductivities are k_{11}=1.82, k_{22}=1.01, and k_{33}=1.71. The point group symmetry requires the first two to be identical. The difference suggests the observed variation in the thermal conductivity with film texture is caused by factors other than simply crystal anisotropy.

Table 5.4 Surface density of the crystallographic planes for rhombohedral PZT.

Atoms/cm^2	(100)	(110)	(111)
Pb Atoms/Area	6.157E+14	4.367E+14	3.601E+14
Ti Atoms/Area		1.747E+14	2.881E+14
Zr Atoms/Area		2.620E+14	4.321E+14
O Atoms/Area	6.157E+14	4.367E+14	1.080E+15

The surface density for the rhombohedral unit cell vs. crystallographic orientation are tabulated above and trends are as (111) >> (110) > (100). From an electroneutrality point of view, from the surface density data, (111) and (100) planes are charge neutral (summation of the products of the surface density with the valence of each element in table 5.4) whilst (110) is not.

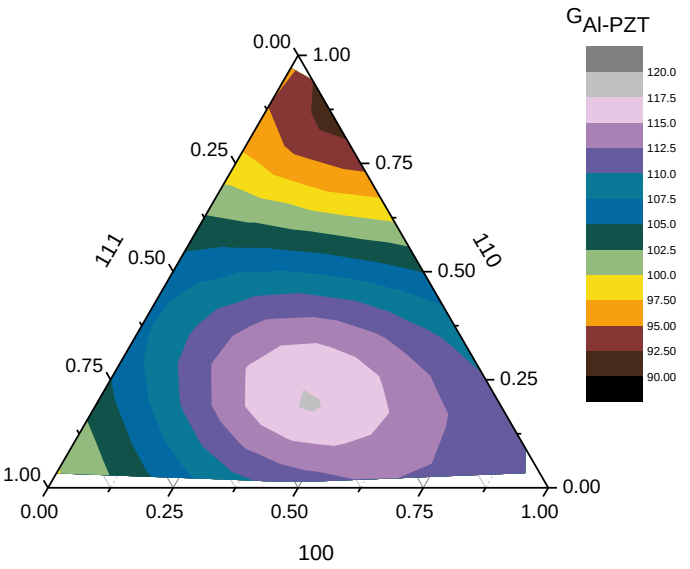

a)

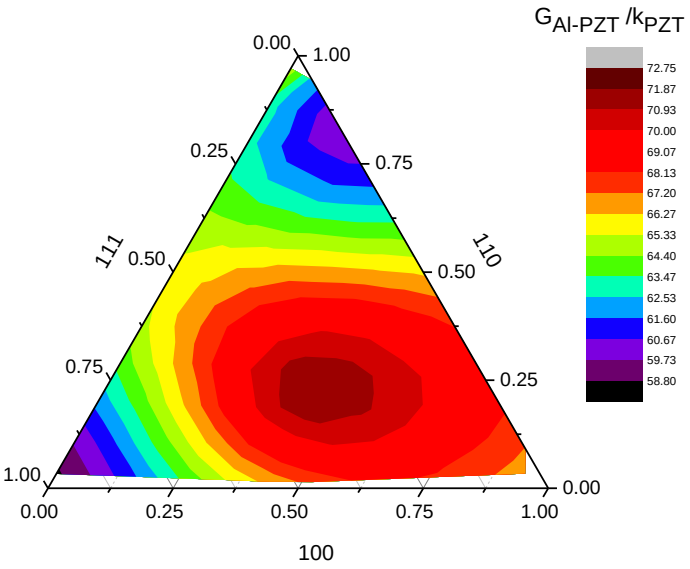

b)

Figure 5.9 Ternary contour plot of interfacial thermal conductance a) G1 or $G_{Al\text{-}PZT}$ b) G1/k or $G_{Al\text{-}PZT}$ /k_{PZT} vs. crystallographic orientation.

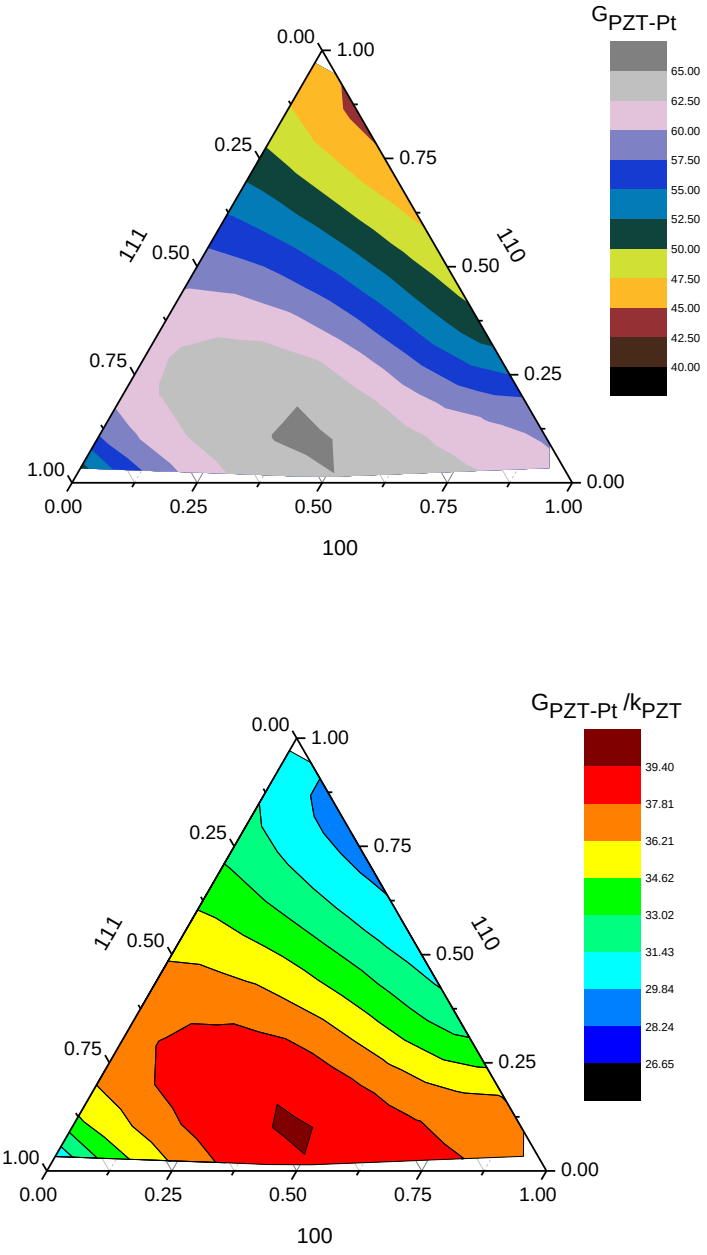

Figure 5.10 Ternary contour plot of interfacial thermal conductance a) G2 or $G_{PZT\text{-}Pt}$ b) G2/k or $G_{PZT\text{-}Pt}/k_{PZT}$ vs. crystallographic orientation.

Figs. 9 and 10 show the ternary plots of the interface thermal conductance for *G1* and *G2* along with each conductance normalized to the thermal conductivity of the PZT layer (*G*/*k*).

From the *G1* ternary plot, all measurements fall within a range of 90-120 MW m^{-2} K^{-1}, with nine of the twelve samples having magnitudes between 100 and 110 MW m^{-2} K^{-1}. The largest conductance values, albeit by a small yet consistent margin, are for samples with significant fraction of (100), with the largest measurement for a roughly 40/20/40 mixture of (100), (110), and (111) orientations. The smallest *G1* values are for samples with large fractions of (111). For the *G2* ternary plot, roughly even mixtures of (111) and (100) give the largest conductances, while samples with large fractions of (100) are also high, and samples containing over 90% fractions of (110) have the lowest conductances. Thus *G1* and *G2* trend slightly as (100) > (111) > (110); while *G1/k* and *G2/k* trend as (100) > (110) ~ (111).

If PbO [1, 9], Ti-rich PZT (~$PbTiO_3$) [4, 8] and ZrO_2 [9] are seeding the (100) texture, then *G2* should decrease with an increase in (100), however, this decrease in *G2* would be small because any oxide layer here would be thin. The thermal conductivity of the elements at the PZT-Pt interface trend as: Pt > Pb >> Zr > Ti >>> O. From surface density calculations, (100) have a higher Pb surface density than (111) and (110) and this may enhance *G2*. The segregation of Ti at the PZT-Pt interface, as seen in the (111) sample's EDS results, has been observed earlier[29] where it was attributed to the Ti flow (and Zr flow away) to the growth interface where heterogeneous nucleation and growth of the crystalline PZT phase occurs. As per binary phase diagrams of Pt-Pb, Pt-Zr and Pt-Ti[30], only Ti and Zr can dissolve in Pt whilst all three, Pb, Ti and Zr, will form intermetallics.

GI-XRD results confirmed standard XRD results for all textured films except for the texturing mixture films 64, 4D, 68 and 7D. All of these films have some pyrochlore $Pb_2(Zr,Ti)_2O_6$ (JCPDS 26-0142). However, samples 68 and 7D are mixtures of 40-50% of (100) with (111) with also show the presence of Pt-Ti alloy (JCPDS 27-1310). These samples also

have the largest interface conductances. Sample 4D has a lower *G2* than 64, and that may be due to higher amount of pyrochlore in the former. With regards to both *G1* and *G2* having similar general trends, this could suggest that the anisotropy within the PZT films may be the reason for the slight dependence of *G* on the crystallographic orientation.

In addition to the textured PZT films, we also examined a 1 micron thick amorphous sample. In this thick sample, the heat pulses from the laser do not penetrate beyond the PZT layer and therefore there are only two unknown parameters, *G1* and k_{PZT}. As one would expect, the thermal conductivity of this amorphous sample is considerably smaller than the conductivity for the crystalline films, as *k* is 0.53 W m^{-1} K^{-1}. Interestingly, despite the significant change in the crystal structure of the PZT film, and, subsequently, the film thermal conductivity, the interface thermal conductance, *G1*, was found to be similar to previous measurements at 100 MW m^{-2} K^{-1}. One possible reason for the lack of change in *G1* with the large change in PZT film structure could be that this interface thermal conductance is controlled by the electron-phonon coupling within the aluminum.

Conclusion

In this article, we report the use of a non-contact optical technique called Time-Domain Thermoreflectance to examine the thermal conductivity and interface thermal conductance for a series of textured PZT samples grown by a sol-gel process. We find that the thermal conductivity of the PZT films ranges from 1.45 to 1.70 W m^{-1} K^{-1} and has a slight dependence on film texture. The interface thermal conductance at Al/PZT and Pt/PZT interfaces also show a similar dependence on crystal orientation. While the origin of these trends is not clear, one possible

explanation is that the anisotropy within the PZT films is responsible for the observed dependence of thermal conductivity and interface thermal conductance.

Acknowledgements: The authors gratefully acknowledge the financial support from ***Air Force Office of Scientific Research (AFOSR)*** through the *Young Investigator Program* and Office of Naval Research through CEHMS seed program. We are also greatly indebted to Reema Gupta for assistance with GI-XRD indexing, Shashank Gupta for valuable discussions, Charles Farley for the FTIR characterization work conducted at Department of Geosciences at Virginia Tech, Holger Cordes of Bruker-AXS for GI-XRD, Ashok Kumar for the Raman work conducted at University of Puerto Rico's Speclab, Deepam Maurya and Chris Winkler for the TEM micrographs and Jerry Hunter of Nanoscale Characterization and Fabrication Lab at Virginia Tech for the XPS analysis.

References

[1] Chen S-Y, Chen IW. Temperature–Time Texture Transition of Pb(Zr1−xTix)O3 Thin Films: II, Heat Treatment and Compositional Effects. Journal of the American Ceramic Society 1994;77:2337.
[2] Daniel M. Potrepka GRF, Luz M. Sanchez and Ronald G. Polcawich. Pt/TiO2 Growth Templates for Enhanced PZT films and MEMS Devices. MRS Proceedings 2011.;1299:s02.
[3] Huang Z, Zhang Q, Whatmore RW. The Role of an Intermetallic Phase on the Crystallization of Lead Zirconate Titanate in Sol–gel Process. Journal of Materials Science Letters 1998;17:1157.
[4] L.M. Sanchez DMP, G.R. Fox, I. Takeuchi and R.G. Polcawich. Improving PZT Thin Film Texture Through Pt Metallization and Seed Layers. MRS Proceedings 2011;1299:s04.
[5] Nittala K, Mhin S, Dunnigan KM, Robinson DS, Ihlefeld JF, Kotula PG, Brennecka GL, Jones JL. Phase and texture evolution in solution deposited lead zirconate titanate thin films:

Formation and role of the Pt[sub 3]Pb intermetallic phase. Journal of Applied Physics 2013;113:244101.
[6] Norga GJ, Fé L, Vasiliu F, Fompeyrine J, Locquet JP, Van der Biest O. Orientation selection in functional oxide thin films. Journal of the European Ceramic Society 2004;24:969.
[7] Reaney I, Taylor D, Brooks K. Ferroelectric PZT Thin Films by Sol-Gel Deposition. Journal of Sol-Gel Science and Technology 1998;13:813.
[8] Tyholdt F, Calame F, Prume K, Ræder H, Muralt P. Chemically derived seeding layer for {100}-textured PZT thin films. J Electroceram 2007;19:311.
[9] Zhu C, Chentao Y, Sheng W, Bangchao Y. The effects of the PbO content and seeding layers upon the microstructure and orientation of sol-gel derived PZT films. J Mater Sci: Mater Electron 2006;17:51.
[10] Varghese R, Williams M, Gupta S, Priya S. Temperature-time transformation diagram for Pb(Zr,Ti)O[sub 3] thin films. Journal of Applied Physics 2011;110:014109.
[11] Hopkins PE, Beechem T, Duda JC, Hattar K, Ihlefeld JF, Rodriguez MA, Piekos ES. Influence of anisotropy on thermal boundary conductance at solid interfaces. Physical Review B 2011;84.
[12] Costescu RM, Wall MA, Cahill DG. Thermal conductance of epitaxial interfaces. Physical Review B 2003;67:054302.
[13] Duda JC, Kimmer CJ, Soffa WA, Zhou XW, Jones RE, Hopkins PE. Influence of crystallographic orientation and anisotropy on Kapitza conductance via classical molecular dynamics simulations. Journal of Applied Physics 2012;112.
[14] Cahill DG, Ford WK, Goodson KE, Mahan GD, Majumdar A, Maris HJ, Merlin R, Phillpot SR. Nanoscale thermal transport. Journal of Applied Physics 2003;93:793.
[15] Cahill DG, Goodson K, Majumdar A. Thermometry and thermal transport in micro/nanoscale solid-state devices and structures. Journal of Heat Transfer-Transactions of the Asme 2002;124:223.
[16] Huxtable S. Time-Domain Thermoreflectance Measurements for Thermal Property Characterization of Nanostructures. In: Haight R, Ross FM, Hannon JB, editors. Handbook of Instrumentation and Techniques for Semiconductor Nanostructure Characterization, vol. 2. Hackensack, NJ: World Scientific Publishing Co. , 2012. p.587.
[17] Wang Y, Park J, Koh YK, Cahill DG. Thermoreflectance of metal transducers for time-domain thermoreflectance. Journal of Applied Physics 2010;108:043507.
[18] Cahill DG. Analysis of heat flow in layered structures for time-domain thermoreflectance. Rev. Sci. Instrum. 2004;75:5119.
[19] Feldman A. Algorithm for solutions of the thermal diffusion equation in a stratified medium with a modulated heating source. High Temp.-High Press. 1999;31:293.
[20] Lang SB, Zhu WM, Ye ZG. Specific heat of ferroelectric Pb(Zr1-xTix)O-3 ceramics across the morphotropic phase boundary. Journal of Applied Physics 2012;111.
[21] Gundrum BC, Cahill DG, Averback RS. Thermal conductance of metal-metal interfaces. Physical Review B 2005;72:245426.
[22] Souza Filho AG, Lima KCV, Ayala AP, Guedes I, Freire PTC, Melo FEA, Mendes Filho J, Araújo EB, Eiras JA. Raman scattering study of the PbZr_{1-x}Ti_{x}O_{3} system: Rhombohedral-monoclinic-tetragonal phase transitions. Physical Review B 2002;66:132107.
[23] Lyeo HK, Cahill DG. Thermal conductance of interfaces between highly dissimilar materials. Physical Review B 2006;73:144301.

[24] Majumdar A, Reddy P. Role of electron-phonon coupling in thermal conductance of metal-nonmetal interfaces. Applied Physics Letters 2004;84:4768.
[25] Kallaev SN, Gadzhiev GG, Kamilov IK, Ornarov ZM, Sadykov SA, Reznichenko LA. Thermal properties of PZT-based ferroelectric ceramics. Physics of the Solid State 2006;48:1169.
[26] Rivera-Ruedas G, Ramirez-Lopez LM, de Jesus FS, Bolarin-Miro A, Munoz-Saldana J, Yanez-Limon JM. Thermal Characterization of PZT Ceramics Obtained by Mechanically Activated Mixed Oxides Using Different Pb Sources. International Journal of Thermophysics 2012;33:2366.
[27] Zhu DM, Han PD. Thermal conductivity and electromechanical property of single-crystal lead magnesium niobate titanate. Applied Physics Letters 1999;75:3868.
[28] Tachibana M, Kolodiazhnyi T, Takayama-Muromachi E. Thermal conductivity of perovskite ferroelectrics. Applied Physics Letters 2008;93.
[29] Muralt P. Recent Progress in Materials Issues for Piezoelectric MEMS. Journal of the American Ceramic Society 2008;91:1385.
[30] Massalski TBOHASMI. Binary alloy phase diagrams. Materials Park, Ohio: ASM International, 1990.

Chapter 6

Piezocap: a MEMS Scalable Non Dimensional Decoupled Vibration Energy Harvester

R. Varghese[1], Justin Farmer[1], Mohan Sanghadasa[2], and Shashank Priya[1]

[1]Center for Energy Harvesting Materials and Systems (CEHMS), Bio-inspired Materials and Devices Laboratory (BMDL), Virginia Tech, Blacksburg, VA 24061

[2]Weapons Sciences Directorate, U.S. Army Research, Development, and Engineering Command, Redstone Arsenal, AL 35898

Abstract

We describe a novel concept towards the development of a MEMS scalable low frequency non-cantilever type broadband piezoelectric energy harvester with active tunability. This structure decouples the energy harvesting component of the device from the resonant vibration component. In doing so, each component can be tailored for maximum efficiency, better scalability and versatility. We did so by using a levitated magnet between two magnets which are in turn attached to two peripherally clamped piezoelectric macro fiber composite strips. The center magnet transfers the source vibration into the device and the outer magnets flex the macro fiber composites. The device incorporates commercial d_{33}-mode P1 type macro fiber composite on one side and a d_{31}-mode P2 type macro fiber composite on the other. We obtained 1.259 μW (1.01 V_{oc}) @ matching load of 225 kΩ and 1.309 μW (0.210V_{oc}) @ 15kΩ for P1 and P2 type harvesters respectively at 460Hz and 1g acceleration. To demonstrate active tunability, we moved to a 2 magnet system with each magnet on the two piezoelectric harvesters and we analyzed the performance against the distance between the magnet + piezo harvester pairs. We

discovered that at a certain threshold distance, the natural frequency of the 2 piezomagnetoelastic systems equal that of a single piezoelectric harvester with an inertial mass equivalent to that of the magnet. Below that threshold distance, the 2 piezoelectric harvesters also are observed to be in synch. We obtained 0.133 μW (0.014 V_{oc}) and 0.559 μW (0.029 V_{oc}) from Top and Bottom harvesters and 3.717 μW (0.119 V_{oc}) and 2.027 μW (0.080 V_{oc}) from Top and Bottom harvesters bonded to Nickel @ matching load of 1500Ω at 626Hz and 1647Hz respectively and 0.3g acceleration. With this work, we therefore demonstrate that with the use of magnets, the dimensionality of harvester's resonant frequency is eliminated and tunability of such of system is purely based on the magnetic force between the magnets.

Keywords: Nonlinear energy harvesting, Piezoelectric, Piezomagnetoelastic, magnetic stiffness, piezo stiffness, linear stiffness, non linear stiffness

Introduction

At the MEMS scale, piezoelectric transduction is the preferred approach in vibration energy harvesting[1]. Traditionally, MEMS based vibrational harvesters utilize a piezoelectric layer over a cantilever structure with tip mass (fixed-free beam configuration). The vibration from the external source is transferred to the cantilever which in turns strains the piezoelectric layer and generates an electric charge. Therefore, the energy harvesting capability is limited by the cantilever area where non-zero strain is present and optimum performance is limited to the narrow region in the vicinity of resonance frequency.

Optimal performance of vibration energy harvesters occurs when their resonance frequency is tuned to that of the source resonance frequency. Resonance frequency of such vibration energy

harvesters is controlled by the dimensions of the device – that is, the mass, length, width and thickness of the vibrating structure. Tunability of this resonance frequency by dimensional variation is complex and usually inconvenient but nondimensional approaches using magnets, load, electrical bias, etc. have been integrated successfully[2]. But what if there is an approach that is nondimensional whilst also decoupling the resonant condition from harvester's natural frequency. That is, can we create an energy harvester which performs best at a frequency away from the resonant frequency of its piezoelectric elements?

We demonstrate here a new MEMS scalable device, termed as PiezoCap, which separates the vibration transfer component from the energy harvesting component. That is, one section of this device, a central magnet, will transfer the source vibration into the device and then that vibration is transferred to piezoelectric transducer element. In doing so, the resonance of the transfer element can be tuned to the source frequency and the transducer element can be designed for maximum energy harvesting capability. Such separation of duties in an energy harvester will lead to realization of low frequency micro scale vibrational devices with maximum piezoelectric area. Unlike cantilever based MEMS devices, the resonance of the device is easily modified by changing the magnetic stiffness without changing the dimensions of the piezoelectric transducer element. We are also able to combine both d33 and d31 mode energy harvesting on the same footprint. For proof of concept, we built a magnetically levitated transfer element coupled to piezoelectric macro fiber composites (MFC) for transduction. Mann et.al[3] measured the spring force of a 3 magnet system similar to our 1st prototype and arrived at a least squares fitted spring force relationship that related the displacement of a center magnet 'x' (analogous to the displacement of our piezo harvesters) with the spacing between magnets 'D'.

$$F(x) = (2\alpha_1 + 4D\alpha_2 + 6D^2\alpha_3)x + 2\alpha_3 x^3 = kx + k_3 x^3 \quad \text{where } \alpha_i \text{ are coefficients of the fit} \qquad (1)$$

We extended this decoupled harvester concept for active tunability and nondimensionality of the resonant frequency by using a simpler 2 magnet+piezoelectric pair, that is, a dual piezomagnetoelastic system. Unlike, the tuning magnet on a fixed support approach by Challa et.al[4], this system is closer to the magnetic oscillator configuration by Tang et.al[5]. Stanton et.al[6] used a piezo cantilever with a magnetic inertial mass with 2 perpendicular fixed magnets that moved along the length of the cantilever to induce hardening and softening stiffness. However, we are using a fixed-fixed beam piezoelectric actuator as the oscillating support for the magnets and the magnets are always in repulsion. Repulsion mode has been found by Tang et.al. to have the best harvesting voltage and bandwidth performance especially when operated near the monostable-bistable transition zone of the intermagnetic spacing[7]. They also show that in attractive mode, the resonance increases and in repulsion mode, the resonance decreases in comparison to a linear non-magnetic piezo actuator configuration.

As can be determined from the name, PiezoCap is designed to be utilized as an encapsulating package for microelectronics chips. In the MEMS scale, unlike traditional cantilever based piezo methodologies[8], the PiezoCap based harvesters will provide larger piezo area as the latter has been moved off the mechanically resonant beam. In doing so, we are not limited to deposited films and their related limitations of throughput and film stress, but can utilize ceramic or single crystal piezoelectric elements.

Experimental Details

Prototype 1

Piezoelectric macro fiber composites (MFC's), M-2814-P1 (d33 mode) and M-2814-P2 (d31

mode) were procured from Smart Materials Inc. Three 3/8" dia. x 1/32" thick Neodymium–Iron-Boron NdFeB Grade N52 magnets from K&J magnetics were configured with their polarity in repulsion with each other. Two of magnets were glued to the MFC's. The third was levitated between the other two in a rigid ABS plastic base (Fig.6.1). The MFC's were glued along its edges to the ABS and therefore were clamped identical to a rectangular diaphragm.

a)

b)

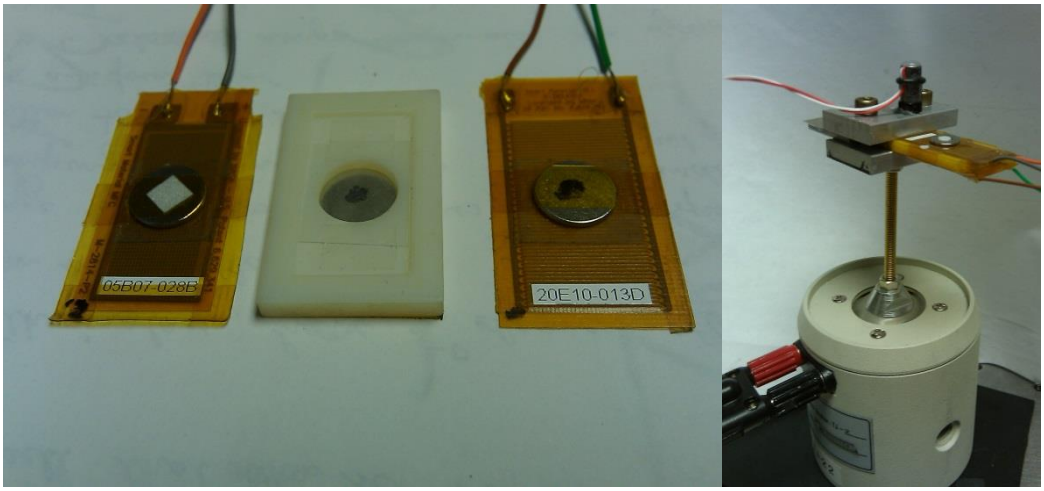

Figure 6.1 a) Schematic and b) Components of PiezoCap Prototype 1 device (left to right) – d31 mode piezo MFC, ABS housing, d33 mode piezo MFC – and the device test setup

We utilized a cantilever type (the harvester is clamped in free-clamped mode) Aluminum clamp mounted onto a TMC Solution TJ-2 electromagnetic shaker which was powered by an HP 6825A power supply/amplifier operating as a fixed gain amplifier. SigLab 20-42 data acquisition system

with four input channels and two output channels is used for the Voltage frequency response function (FRF) measurements. The reference acceleration was measured at the clamp using a accelerometer (Piezotronics Inc. model # U352C67). Voltage generated by the harvester and the power loading curves were generated by placing a digital IET Labs load resistor in series with the harvesters. The output signal from the accelerometer was conditioned using a charge amplifier (Piezotronics Inc.). The velocity at the tip of cantilever beam was measured using a digital vibrometer (Polytec OFV 353). Polytec 5000 controller was used to generate input signals to the seismic shaker to create vibration and also to capture the output signals from accelerometer and vibrometer. The velocity FRF's for each piezomagnetoelastic harvester was measured by clamping each of them facing the laser head.

Prototype 2

Rectangular d31 mode piezoelectric actuators, called Quikpaks, model # QP16n from Midé were cut to the square shape at the piezo end. ABS plastic base of 25mm height was 3D printed and used as the housing to levitate the center magnet and clamp the piezo harvesters by their corners on opposing faces. A new clamp in line with shaker motion eliminated the cantilever clamping induced resonant peaks of Prototype 1. 2 NdFeB magnets of 1/8" diameter x 1/32" height was placed on each piezo actuator as shown below. The dual magnet configuration was chosen to improve the strain capability of each PiezoCap. The center NdFeB magnet was a 1/4" diameter x 1/8" height.

a)

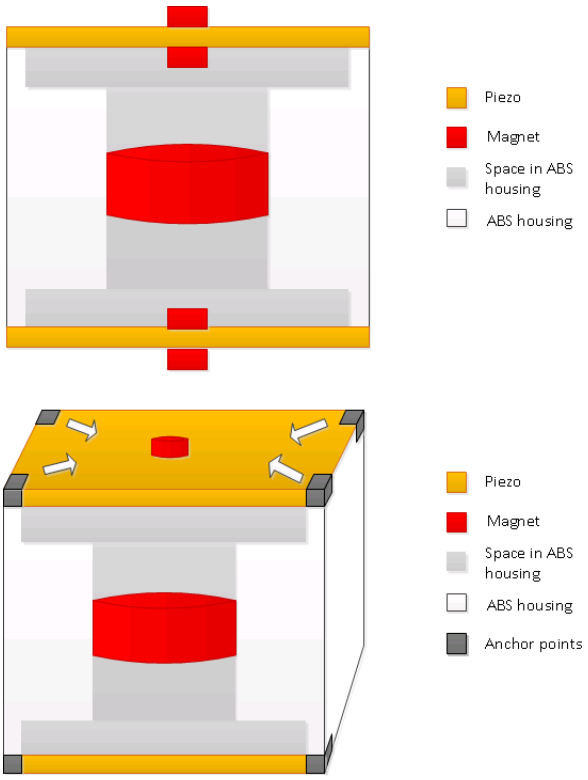

b)

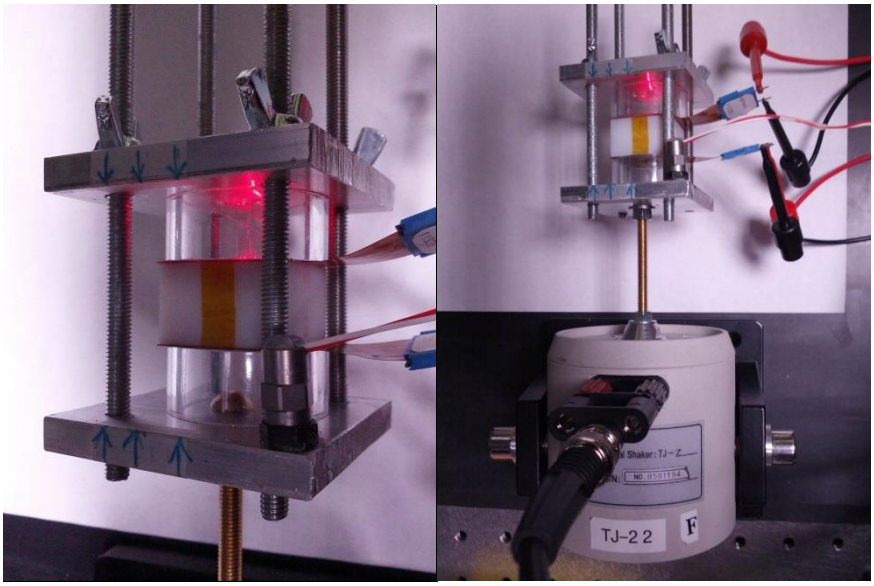

Figure 6.2 a) Schematic and b) Components of PiezoCap Prototype 2 – 2 Quikpaks spaced apart by ABS housing and held by clear plastic cylinders and the device test setup

Prototype 3

Quikpaks from Prototype 2 was reused for this prototype. The resonance frequency was

measured by laser Doppler Vibrometry of the topmost Quikpak in the device. Understandably, due to the clamp and shaker, the velocity FRF's of only the top piezomagnetoelastic harvester could only be measured. However, generated voltage was collected from both top and bottom harvesters.

a)

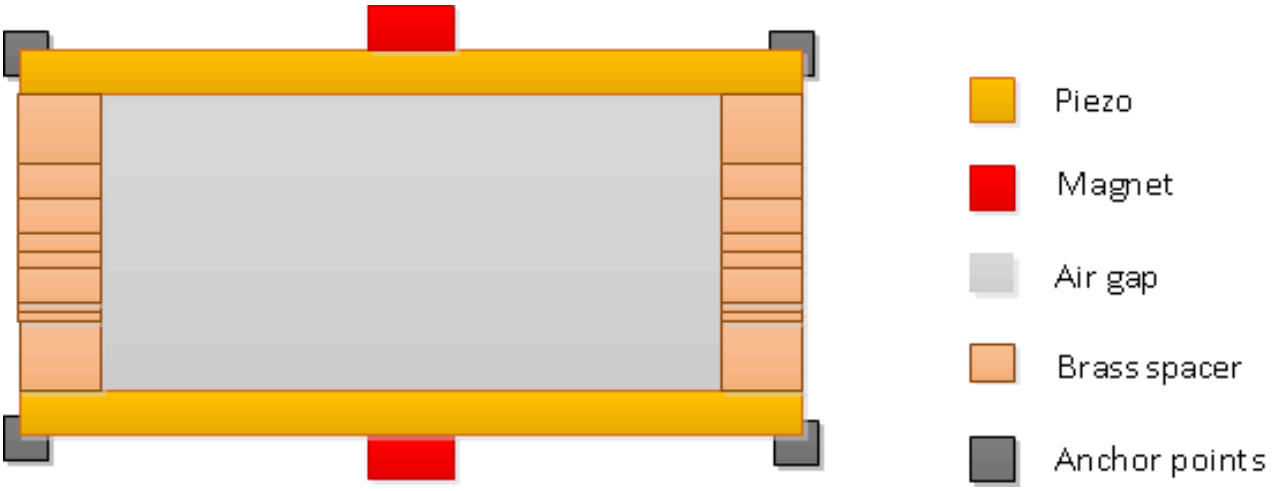

b)

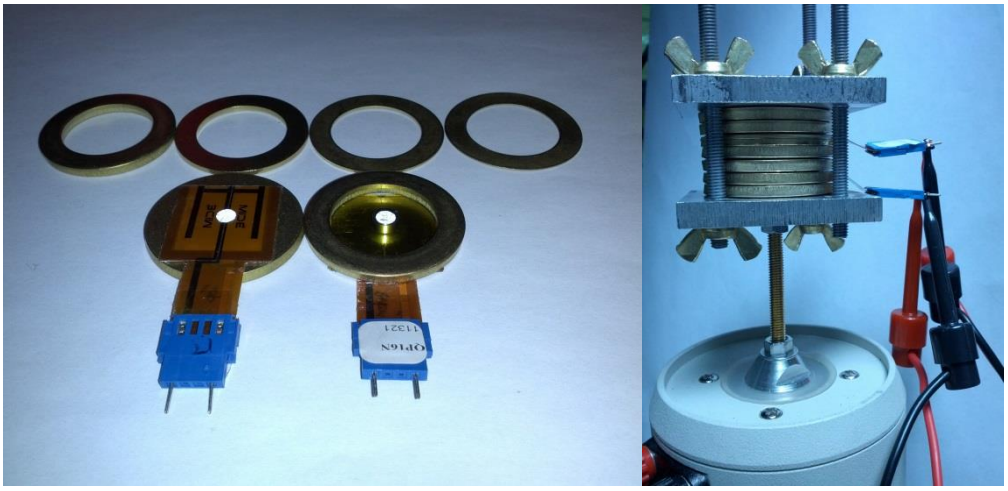

Figure 6.3 a) Schematic and b) Components of PiezoCap Prototype 3 – 2 Quikpaks spaced apart by and held by Brass washers and the device test setup

0.125", 0.063". 0.032" and 0.016" thickness brass washers were used in varying combinations to achieve the variable spacing between the 2 magnet + harvesters pairs. Velocity and Voltage FRF

data was collected for 3 device configurations: a) with 2 different sizes of NdFeB magnets - ¼" diameter x 1/8" thickness and ¼" x 3/16" – and b) with ¼''x1/8''magnets with a 5mils Nickel 201 shim bonded to the Quikpaks. The ¼''x1/8'' and ¼" x 3/16" magnets when used as an inertial mass weighed in at 0.75gms and 1.13gms respectively. The Nickel is a neutral axis modifier in that it moves the neutral axis of the composite structure into the nickel. Doing so will ensure that the stresses generated across the piezo thickness are of the same sign for both upward and downward displacement and therefore do not cancel each other out.

Results and Discussion

Prototype 1

The clamping in a cantilever fashion produces stray resonance peaks from clamp[9] and the cantilever bending of the device. The Velocity and Voltage FRF's demonstrate that the fundamental resonance of the system is due to the piezomagnetoelastic transduction. As the Smart Materials macro fiber composite harvesters were used as-is (neutral axis in piezo layer), their energy harvesting performance was limited to 1.259 μW (1.01 V_{oc}) @ matching load of 225 kΩ and 1.309 μW (0.210V_{oc}) @ 15 kΩ for P1 and P2 type harvesters respectively at 460Hz and 1g acceleration.

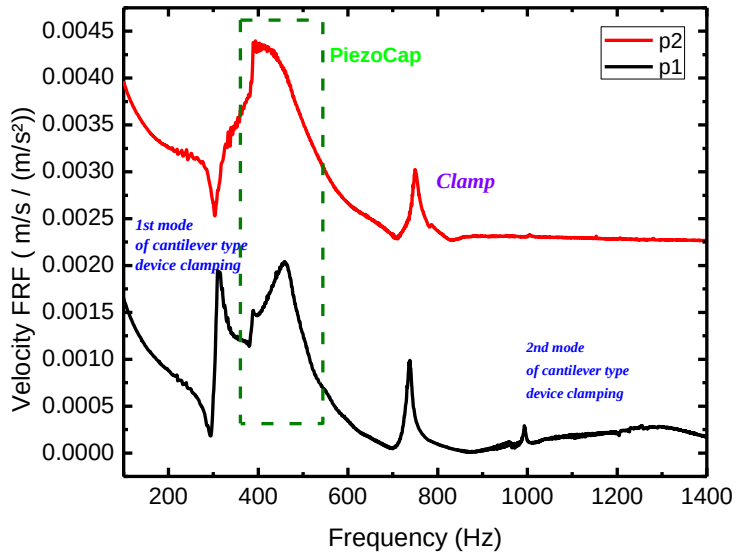

a)

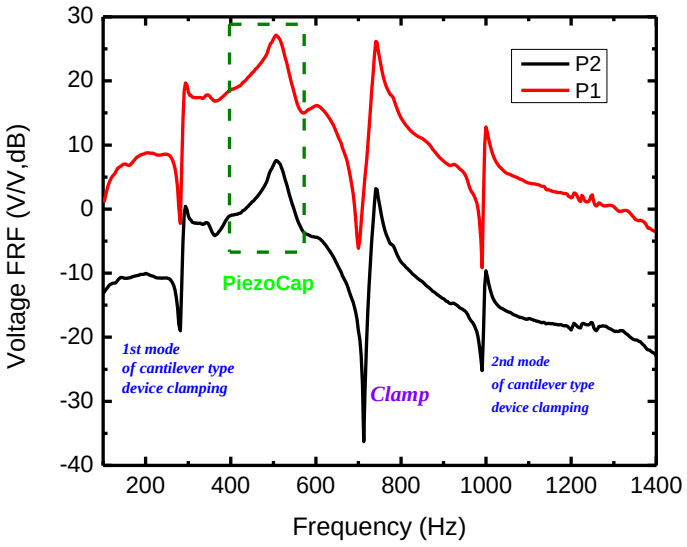

b)

Figure 6.4 a) Velocity FRF and b) Voltage FRF for Prototype 1

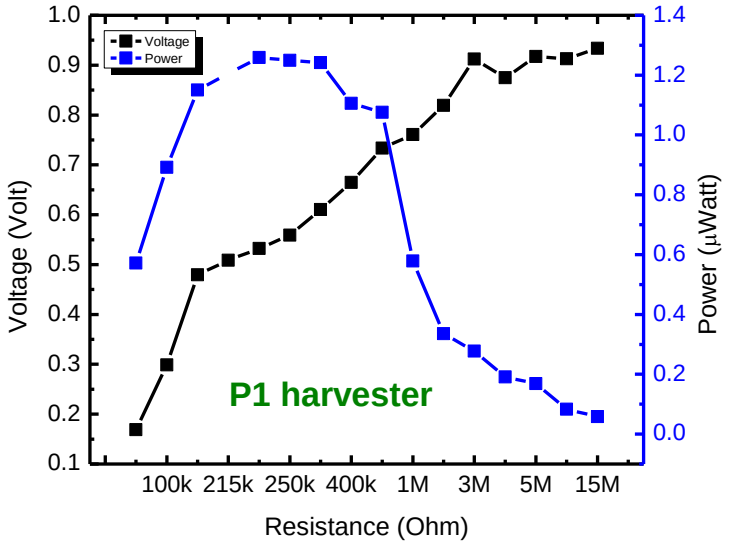

a)

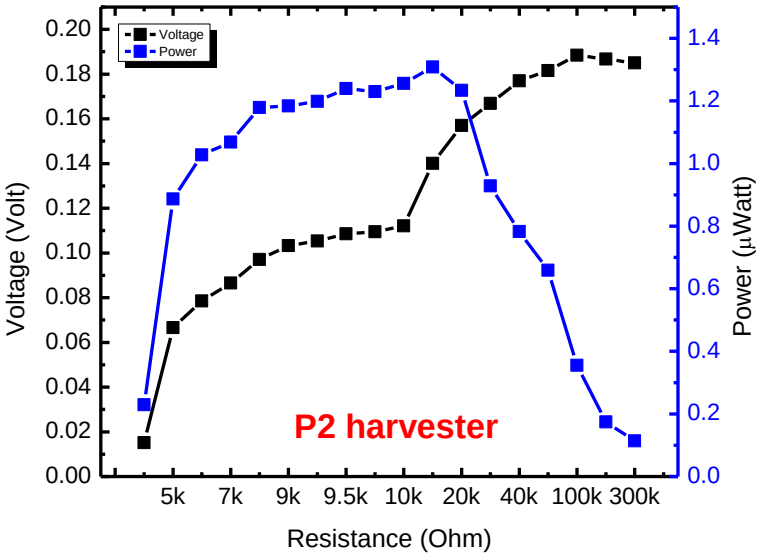

b)

Figure 6.5 Voltage and Power loading curves for a) P1 d33 MFC and b) P2 d31 MFC

Prototype 2

We used edge clamping to increase area under strain in the piezo harvesters. To obtain low

resonant frequency, we used a taller ABS housing that provided a 15mm gap between the magnets. However, we could not obtain a single resonant frequency for the piezomagnetoelastic transduction. However, the resonances of the levitated 3 magnet system and the Quikpak are separately visible. Therefore, we realized that we need larger magnets in proximity to achieve high piezomagnetoelastic performance.

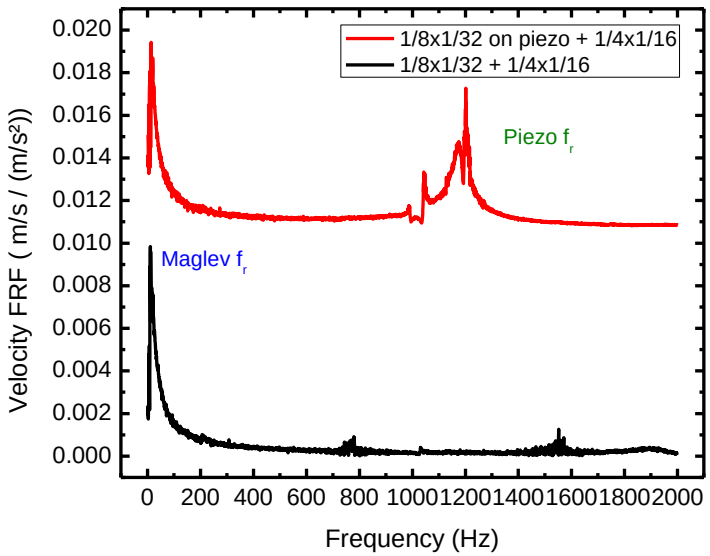

Figure 6.6 Separation of fundamental resonances in Prototype 2: bottom curve with magnets without piezo and top with magnets on piezo

Prototype 3

The change in resonance frequency vs. the gap between the 2 piezomagnetoelastic harvesters using brass washers are shown below. The fundamental resonance is observed to follow a bowl profile with spacing between the magnets for all the 3 harvester configurations of 0.75gm magnets, 1.13magnets and Ni+0.75gm magnets. The minimum occurs expectedly at different

threshold spacing for each of these configurations. This minimum resonant frequency matches that of a Quikpak with a single magnet as inertial mass. The frequency shift from this minimum follows a zigzag pattern. When the two piezomagnetoelastic harvesters are brought closer from the tens of mm's distance, the repulsion magnetic fields will increase the stiffness of the system and then as the magnetic forces balances out the piezo stiffness force, the resonance reaches the minimum.

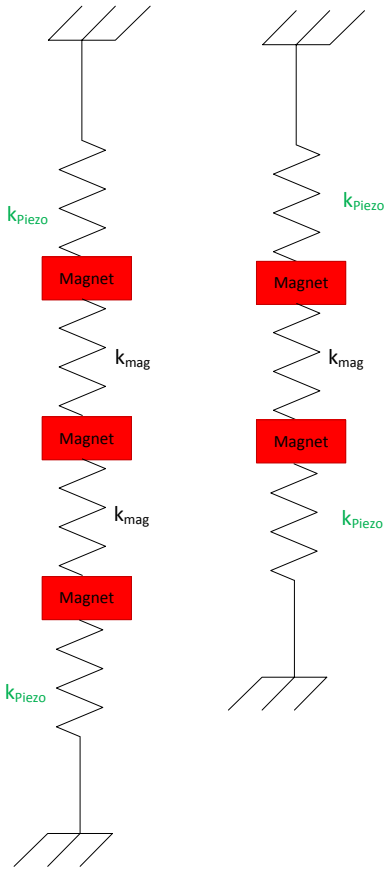

Figure 6.7 The spring force diagrams for Prototype 1 on left and 2 on right

This phenomenon can be explained by the effective spring constant for springs in series (as shown in above figure for Prototype 1 and 3):

$$k_{eff} = \frac{1}{\frac{1}{k_{piezo}} + \frac{1}{k_{mag}} + \frac{1}{k_{piezo}}} = \frac{k_{piezo}k_{mag}}{2k_{mag} + k_{piezo}}$$

$$\text{when } k_{piezo} = -k_{mag} \text{ then } k_{eff} \to k_{piezo} \qquad (2)$$

$$\text{and } \omega_n = \frac{1}{2\pi}\sqrt{\frac{k_{eff}}{m_{eff}}}$$

Further decrease at this minimum resonance or threshold distance, the magnetic fields increase the stiffness back again.

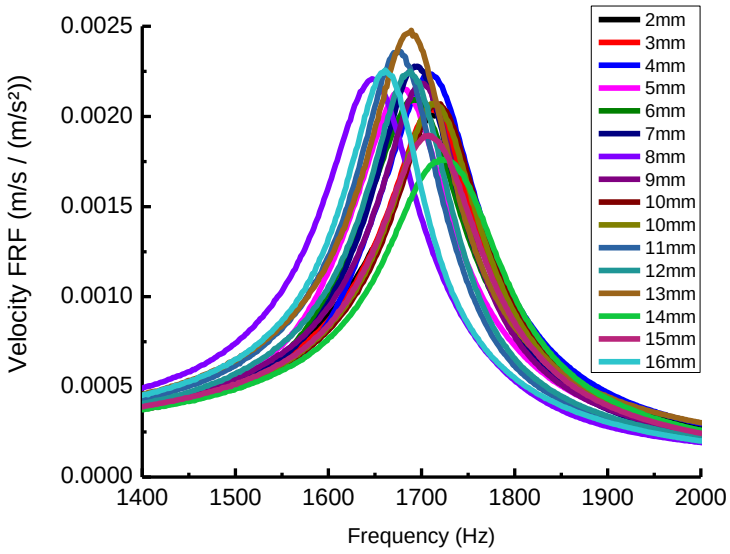

Figure 6.8 The resonant frequency variation with spacing between the magnets for the Nickel neutral axis modified harvester

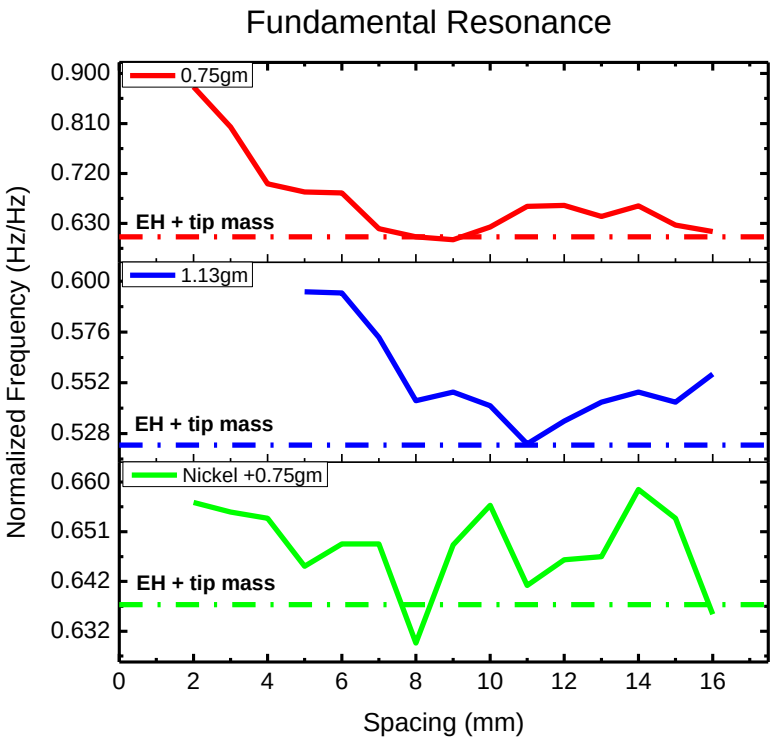
Fundamental Resonance
0.75gm
EH + tip mass
1.13gm
EH + tip mass
Nickel +0.75gm
EH + tip mass
Normalized Frequency (Hz/Hz)
0.900
0.810
0.720
0.630
0.600
0.576
0.552
0.528
0.660
0.651
0.642
0.632
0
2
4
6
8
10
12
14
16
Spacing (mm)

a)

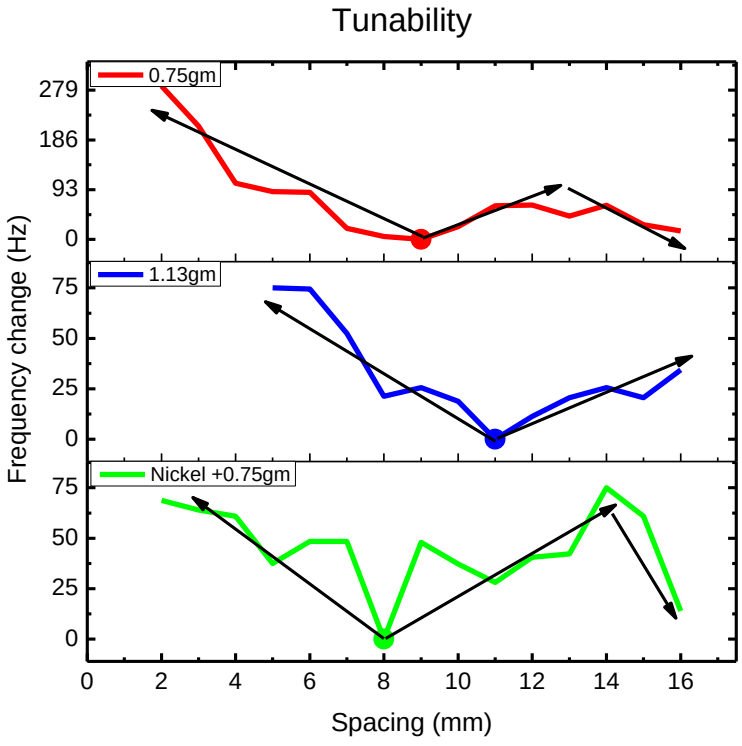
Tunability
0.75gm
1.13gm
Nickel +0.75gm
Frequency change (Hz)
279
186
93
0
75
50
25
0
75
50
25
0
0
2
4
6
8
10
12
14
16
Spacing (mm)

b)

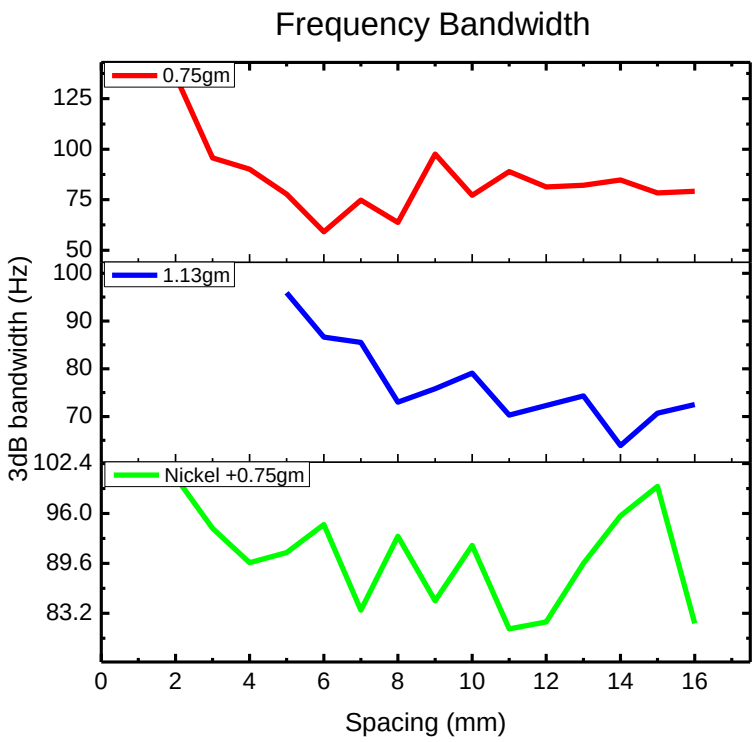

c)

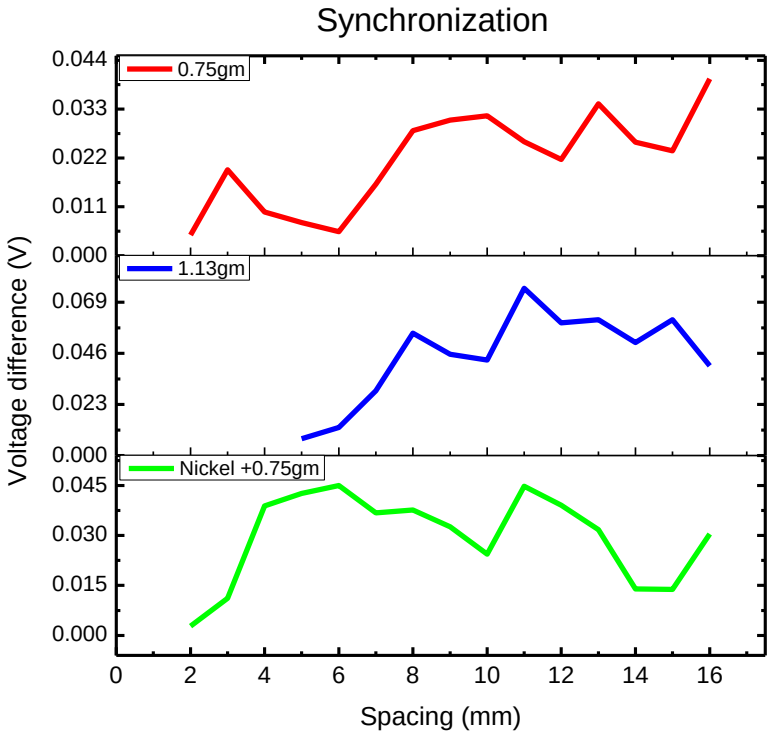

d)

Figure 6.9 Variation in a) normalized resonance b) frequency shift c) 3dB bandwidth and d) generated voltage difference for Prototype 3

Interestingly, the 3dB bandwidth decreases linearly with spacing and may be due to increased non linearity and transition from monostable to bistable potential energy state of the repulsive magnetic system. The Q (=fr/Δf) ranged from 17-21, 6-9 and 6-12 for the Nickel modified + 0.75gm, 1.13gm and 0.75gm magnet systems respectively. The heavier magnet system had the least Q factor and the largest bandwidth for operation. Also, as the 2 piezomagnetoelastic harvesters are brought closer, their generated voltages become closer in value and demonstrate a possible methodology for synchronization of multiple vibration harvesters. This is especially true because there is no alignment guide or rod to center 2 magnets directly over each other. With smaller intermagnetic spacing below a threshold distance, the magnets are now in bistable configuration and can easily find their mutual potential energy minimum by jumping across the energy barrier across the 2 potential energy wells[7].

Tang et.al[7] states that the threshold distance is when the spring forces for the repulsive magnets equates the spring force due to the piezo stiffness. The spring force in the system for 'x' amount of deflection of the piezo harvester is

$$F(x) \approx \left(k_{piezo} + k_{linear,mag}\right)x + k_{nonlinear,mag}x^3 \qquad (4)$$

The linear magnetic stiffness term is negative for magnets in repulsion and so the linear term will eliminate itself by equaling that of the piezo at a certain magnetic spacing 'D'. When equating the linear terms to zero, we can get the threshold distance 'D' between the magnets as

$$D = \left(\frac{3d\mu_o m^2}{2\pi k_{piezo}}\right)^{1/5} \qquad (5)$$

where d is a geometrical factor related to the distance between the measurement point and the harvester free end, μ_o is the permeability constant 4π x 10^{-7} N/A^2, and m is the magnetic moment. From the equation, we can see that higher piezo stiffness requires higher magnetic

moment for the same D. Below this threshold distance, the magnets are in a bistable state (the potential energy of the system has a double well with respect to 'x') and in a monostable state above it. This phenomenon might explain the increase in bandwidth with decrease in spacing and the synchronization of the harvesters.

The linear and nonlinear spring constants for the magnets are proportional to D^{-5} and D^{-7} respectively[7]. Therefore with decrease in D, these spring constants will increase considerably and that too, in opposite directions with the nonlinear term increasing at a slower rate. The linear magnetic stiffness force is negative and the non-linear term is positive. With decease in D, the negative component has a softening effect whilst non-linear term has a hardening effect. This non-linear hardening explains the initial increase in resonance frequency with decrease in D followed by the linear softening then taking over and decreasing the resonance frequency. Further decrease in D causes the non-linear hardening force (proportional to x^3) overcome the negative linear softening force. In addition, a bistable state is achieved and the system has to transition across the energy barrier between the 2 potential wells. Herein lays the crux of the non-dimensionality aspect of this piezo vibration harvester. Near the threshold distance D, the magnetic stiffness force is predominant and therefore will determine resonance of the system. Since the mass of the system is unchanged, the resonance frequency will decrease as observed.

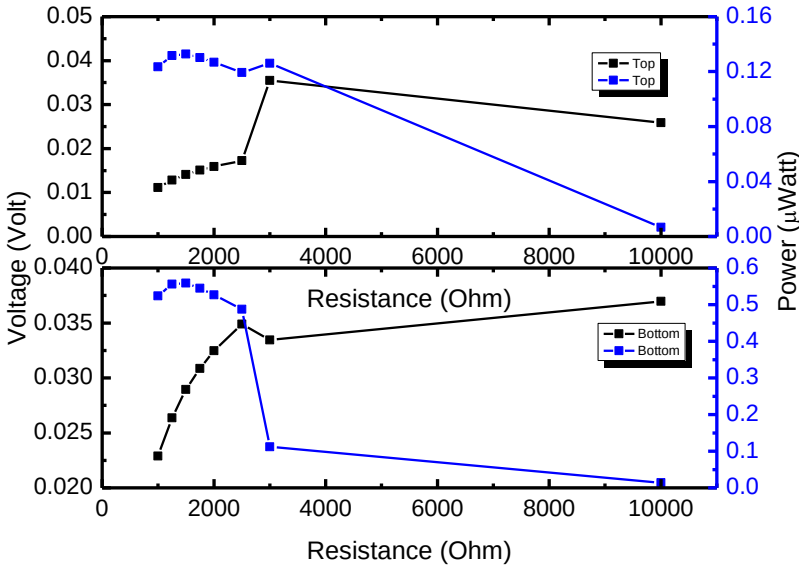

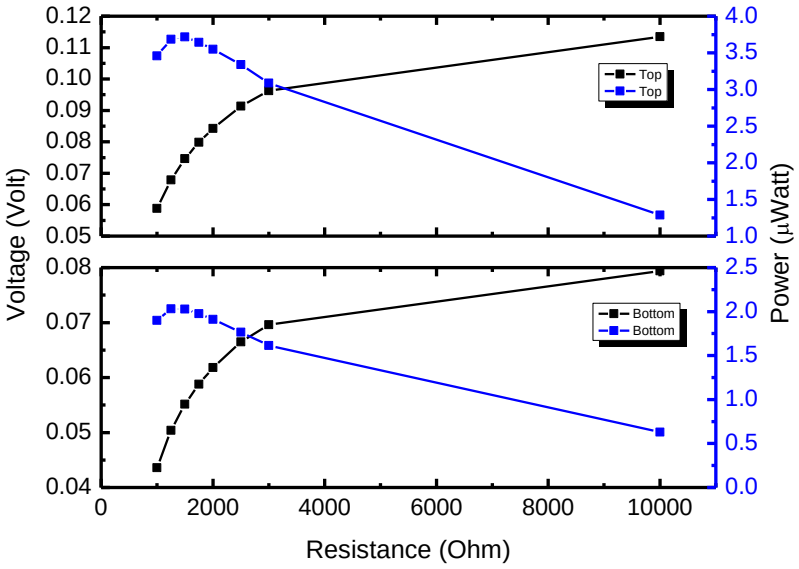

a)

Figure 6.10 Voltage and Power loading curves for Top and Bottom Quikpaks a) As is and b) with Nickel neutral axis modifier in Prototype 3

We obtained 0.133 μW (0.014 V_{oc}) and 0.559 μW (0.029 V_{oc}) from Top and Bottom harvesters and 3.717 μW (0.119 V_{oc}) and 2.027 μW (0.080 V_{oc}) from Top and Bottom harvesters bonded to

Nickel @ matching load of 1500Ω at 626Hz and 1647Hz respectively and 0.3g acceleration. With this piezomagnetoelastic system, we achieved 3.09x higher voltage than that of the piezo alone with an inertial mass, 4.18x on adding a neutral axis modifier to the piezo harvesters and finally 5.74x with the neutral axis modifier at the threshold distance.

To fabricate PiezoCap in the MEMS scale, Piezo thin films and electrode patterns will be first processed onto a Si wafer. This wafer will be thinned from the opposing side to make a 'micro' fiber composite – the PiezoCap component. The center magnet will be held in either a PDMS (made from Si master mold) or micro machined Si housing. After bonding the outer magnet to each PiezoCap, both PiezoCaps will be attached to the center magnet housing. This MEMS device will be more immune to air damping than cantilever based MEMS energy harvesters (which require vacuum packaging). When the source vibration is replaced with an AC magnetic field, this device can also operate as a Magnetoelectric MEMS harvester. We also envision PiezoCap as an active energy harvesting package for integrated circuits or other microelectronic components.

Conclusion

We have demonstrated a novel concept of nondimensionality of resonance of a piezoelectric vibration energy harvester using magnetic force. Varying the distance between the magnets in the resultant piezomagnetoelastic devices provide many advantages like active tunability, high bandwidth and the synchronization of multiple harvesters. At a certain threshold distance between magnets, the magnetic force balances that due to the piezo stiffness and the resonance frequency of the system is that of a piezo with an inertial mass equivalent to the mass of the

magnet. We have named this device, PiezoCap, as it can be used as an encapsulating energy harvester in electronic circuit packages. Finally, we have described the process flow to develop such a device in the MEMS scale.

Acknowledgements: The authors gratefully acknowledge the financial support from ***Center of Energy Harvesting and Material Systems (CEHMS)***.We are also greatly indebted to Anthony Marin, Eric Baldrighi, Daniel Apo and Nathan Sharpes, our colleagues in CEHMS for valuable discussions about the experimental setup.

References

[1] Mitcheson PD. Performance limits of the three MEMS inertial energy generator transduction types. Journal of Micromechanics and Microengineering 2007;17:S211.
[2] Twiefel J, Westermann H. Survey on broadband techniques for vibration energy harvesting. Journal of Intelligent Material Systems and Structures 2013.
[3] Mann BP, Sims ND. Energy harvesting from the nonlinear oscillations of magnetic levitation. Journal of Sound and Vibration 2009;319:515.
[4] Challa VR, Prasad M, Shi Y, Fisher FT. A vibration energy harvesting device with bidirectional resonance frequency tunability. Smart Materials and Structures 2008;17:015035.
[5] Tang L, Yang Y. A nonlinear piezoelectric energy harvester with magnetic oscillator. Applied Physics Letters 2012;101:094102.
[6] Stanton SC, McGehee CC, Mann BP. Reversible hysteresis for broadband magnetopiezoelastic energy harvesting. Applied Physics Letters 2009;95:174103.
[7] Tang L, Yang Y, Soh C-K. Improving functionality of vibration energy harvesters using magnets. Journal of Intelligent Material Systems and Structures 2012;23:1433.
[8] Andò B, Baglio S, Trigona C, Dumas N, Latorre L, Nouet P. Nonlinear mechanism in MEMS devices for energy harvesting applications. Journal of Micromechanics and Microengineering 2010;20:125020.
[9] Erturk A, Inman DJ. Piezoelectric Energy Harvesting: Wiley, 2011.

Chapter 7

Magnetoelectric Macro Fiber Composite

Ronnie Varghese,[1] Ravindranath Viswan,[2] Donald Leber,[3] Mingkai Mu,[3] Mohan Sanghadasa[4] and Shashank Priya[1,*]

[1]Center for Energy Harvesting Materials and Systems (CEHMS), Bio-Inspired Materials and Devices Laboratory (BMDL), Virginia Tech, Blacksburg, VA 24061, USA
[2]Materials Science and Engineering Department, Virginia Tech, Blacksburg, VA 24061, USA
[3]Electrical and Computer Engineering Department, Virginia Tech, Blacksburg, VA 24061, USA
[4]Weapons Sciences Directorate, U.S. Army Research, Development, and Engineering Command, Redstone Arsenal, AL 35898

Abstract

This paper describes the fabrication and performance results of a magnetoelectric macro fiber composite (ME MFC). The magnetoelectric composite was fabricated by bonding a magnetostrictive layer to a piezoelectric layer using novel approach of low temperature transient liquid phase (LTTLP) bonding. The composite was diced into 150 micron wide fibers and bonded to a custom designed copper flexible circuit using a spin coated low viscosity room temperature curing epoxy. ME MFC's with varying ferrite thicknesses of 0.6mm and 0.5mm were fabricated and characterized for energy harvesting. The composite with 0.6mm ferrite thickness achieved an open circuit voltage of 101mV (ME voltage coefficient of 1667 mV/cmOe) and peak power of 1.9nW across 356kΩ matching load at 264Hz .

Keywords: macro fiber composite; low temperature bonding; magnetoelectric composite

Introduction

Magnetoelectric (ME) composites have been found promising for sensors, phase shifters, filters, and tunable transformers. Such devices usually consist of a composite structure that includes a magnetostrictive phase in contact with a piezoelectric phase. The efficiency of the elastic coupling between the two phases depends upon the strain transfer occurring at the interface. The magnetoelectric response can be maximized by improving the interfacial properties in terms of matching the mechanical impedance between the magnetostrictive and piezoelectric layers[1],[2]. Epoxy bonding has been found to perform better than both a Ag-Si alloy with 600 ^{o}C working temperature and a thin borosilicate with 500-600 ^{o}C bonding layers[3]. In ME thin film composites, the addition of a Pt layer between the piezoelectric film and the magnetostrictive film has been shown to double the magnitude of ME coefficient [4]. In the case of bulk ME composites, the addition of an embedded metallic layer has also resulted in improved ME performance by suppressing interdiffusion between the cofired piezoelectric and magnetostrictive layers[5]. Building upon these prior findings, we demonstrate here a metallic bonding process for attaching the piezoelectric and magnetostrictive layer in ME laminate composites. The constraints on the bonding process included thin dimensions of the interface and process temperature below the Curie temperature of the magnetostrictive and piezoelectric layers.

Transient liquid phase (TLP) bonding has been in use for centuries but has recently come to prominence in aerospace and semiconductor industries for the joining of two metallic surfaces[6]. The process entails a thin interlayer metal containing a melting point depressant that melts and fills the voids of the two metal surfaces in contact. This depressant metal diffuses into

the parent metal, undergoes isothermal solidification and then upon cooling, the joint becomes homogeneous. Another variant of TLP bonding that employs a low temperature melting solder is low temperature transient liquid phase bonding (LTTLP)[7]. In this latter case, ceramic or metal surfaces are bonded by utilizing a base metal coating on each of the mating surfaces and then adding a low melting solder between the base metal layers on each bonding surface. At the solder melting point, some of the base metal dissolves in the solder and undergoes isothermal solidification. The resultant solder-base metal alloy has a higher eutectic point than the solder melting point and therefore, the resultant bond can withstand higher temperatures than the temperature at which bonding occurred.

Experimental Procedures

The ceramic raw materials were acquired from Piezo systems (5A4E 0.127mm sheet) and Electroscience (Type 40011 ferrite tape). The nickel coating of the piezo sheets were wet etched off using TFG nickel etchant from Transene at 60 ^{o}C. After that they were cut into 21mm squares. The ferrite tape was fired as recommended by the vendor. Indalloy 1E (In 52%, Sn 48%) with eutectic point 118 ^{o}C was chosen for the bonding due to the ease of availability and cost. Both ceramics were coated with 1000Å Au over a 1000Å Ti adhesion layer as Au forms a high eutectic point interlayer with In and Sn (Au-In eutectic point occurs at 465 ^{o}C whilst that for Au-Sn occurs at 280 ^{o}C). Solder alloy with 10μm was deposited using a high throughput ultrasonic jet vapor deposition process (Jet Process Corporation). These single side coated ferrite and piezo sheets were then pressed down with a 100gm weight at 125 ^{o}C for an hour in the forming gas environment of an alloying station.

a)

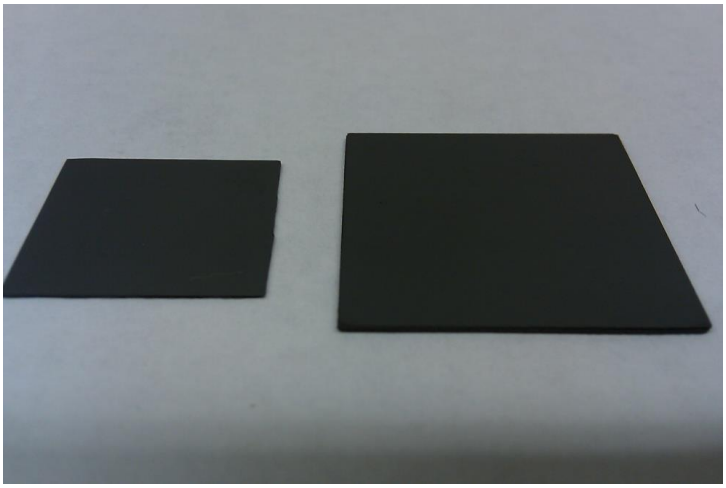

b)

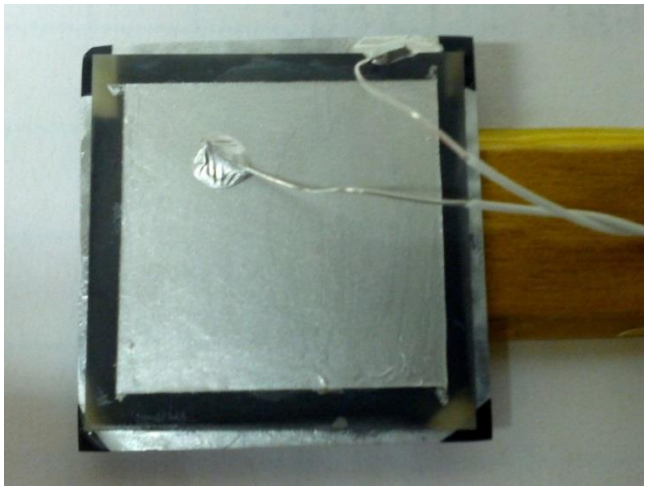

c)

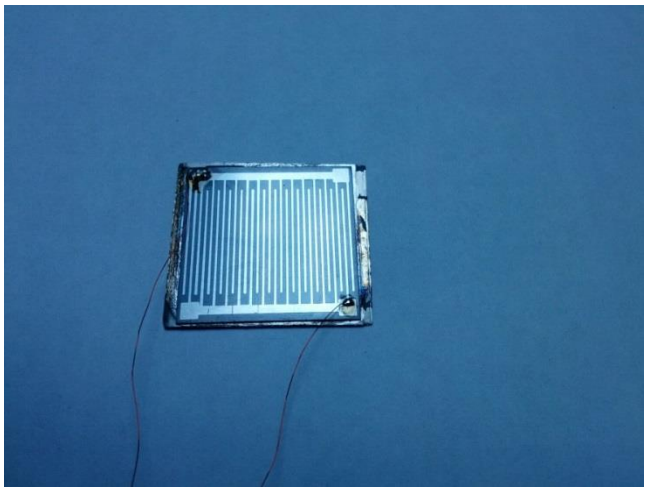

Figure 7.1 a) Ferrite 40011 fired sheet and ME soldered composite with b) d_{31} mode electroding using silver paste conductors and c) d_{33} mode electroding using Pt conductors.

The ME composite was then coated with room temperature silver paste on top of the piezo and tested for d_{31} mode ME performance. No poling was required as we used the piezo in vendor poled d_{31} mode. Next the Ag paste was removed in acetone and Pt was deposited through a shadow mask with 200 μm line width and 500 μm spacing. The piezo was repoled at 4000V/mm (vendor recommended 50-100V/mil) condition. The Pt IDE coated ME composite was then tested for d_{33} mode ME performance. After testing, the Pt was polished off using fine grit sand paper.

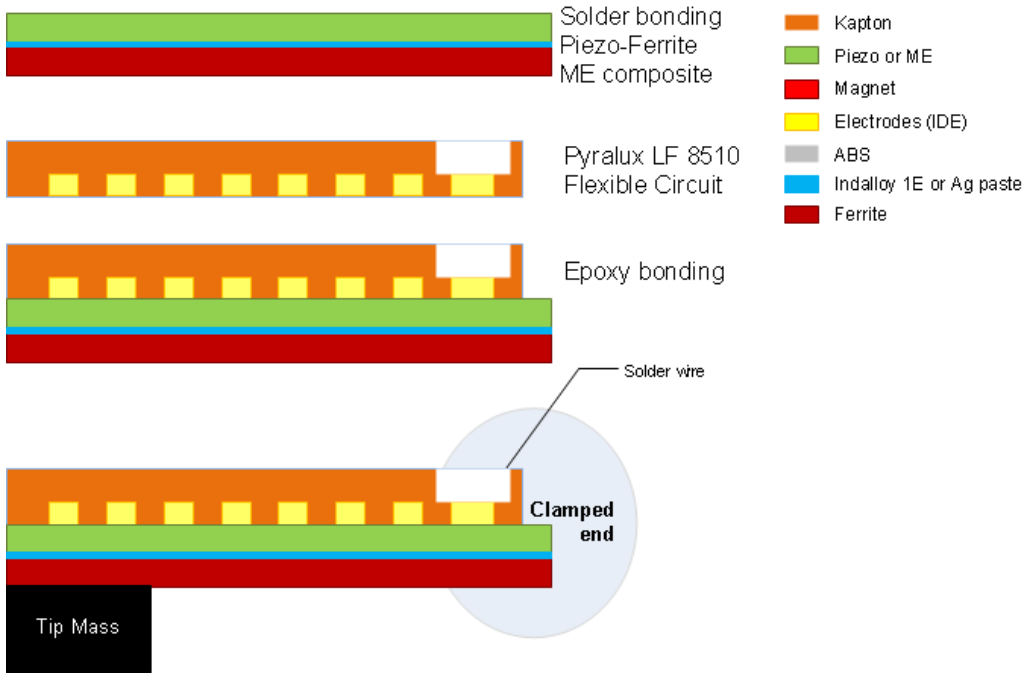

Figure 7.2 Schematic of the fabrication process flow for ME macro fiber composite cantilever

For the MFC's flexible circuit, an interdigitated electrode (IDE) pattern of 150 μm line width copper interconnects spaced at 150 μm was designed and printed. Moog Inc. made the flexible circuits from Dupont Pyralux LF8510 tape and for ease of wire bonding provided immersion Ag

finish on the contact pads. The ME composite was diced into 150 μm wide fibers with a 3ml resin blade with 45 μm diamond size particles (Semicon Tools, Inc).

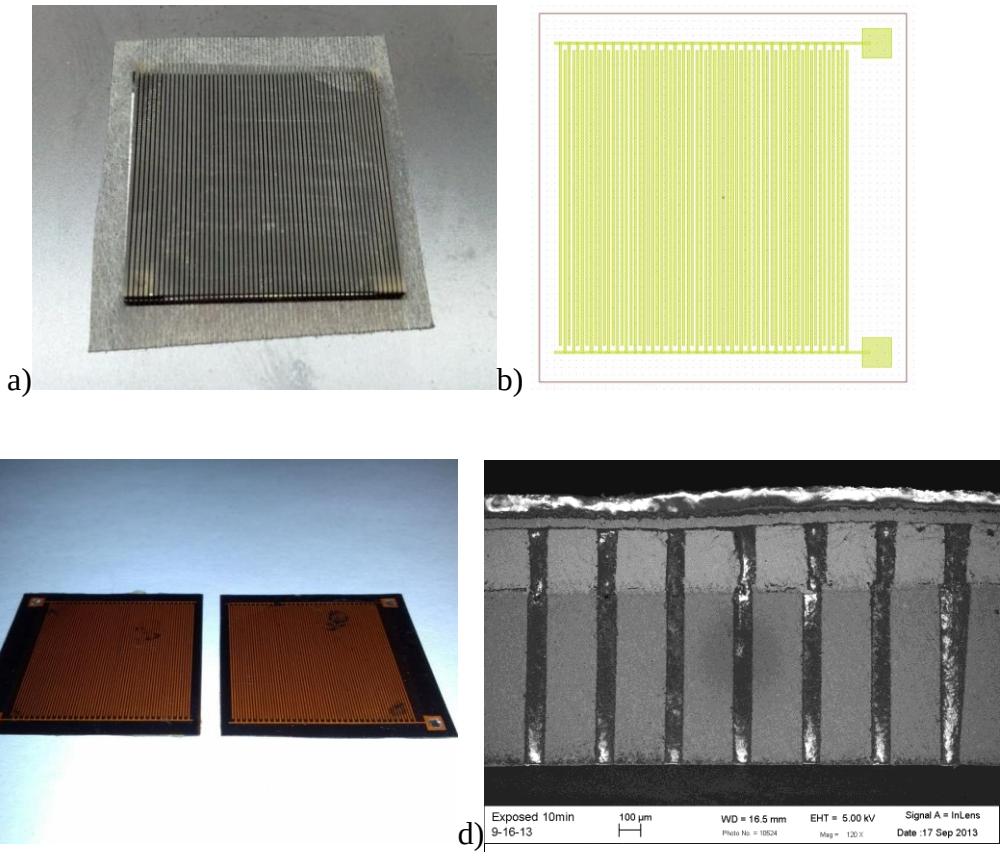

Figure 7.3 a) diced ME composite b) IDE pattern for flexible circuit and c) final ME macro fiber composite (ferrite of 0.5mm on left and 0.6mm on right) and d) SEM cross section of the ME MFC.

The flexible circuit was spin coated with Extreme 2115 250cP epoxy and vacuum bonded for 12 hours on one side of diced ME composite fibers at room temperature. The MFC was poled at vendor recommended 4000V/mm condition.

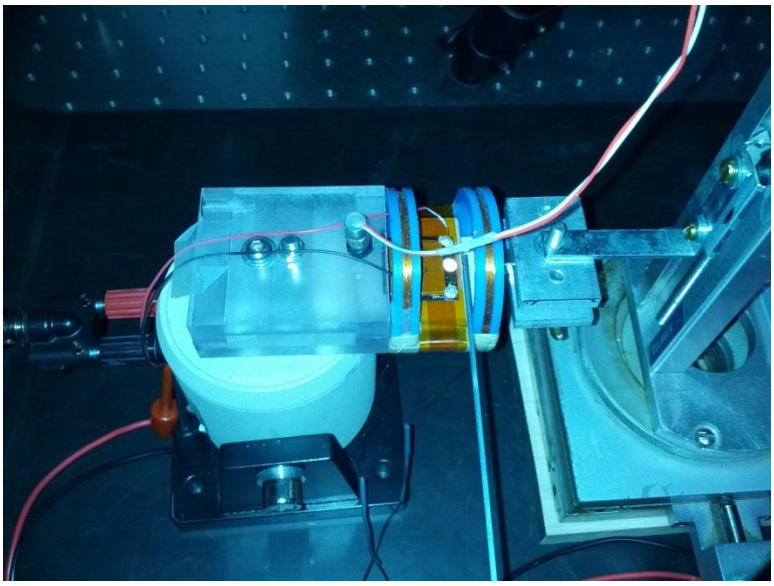

Figure 7.4 Magnetoelectric test setup with translatable DC bias shown on the right side of the figure.

We utilized a cantilever type (the harvester is clamped in free-clamped mode) aluminum clamp mounted onto a TMC solution TJ-2 electromagnetic shaker which was powered by an HP 6825A power supply/amplifier operating as a fixed gain amplifier. SigLab 20-42 data acquisition system with four input channels and two output channels was used for the voltage frequency response function (FRF) measurements. This data acquisition system has an internal resistance of 995 kΩ and this resistance was in parallel with any load resistance attached externally to the device under the test. The reference acceleration was measured at the clamp using an accelerometer (Piezotronics Inc. model # U352C67). Voltage generated by the harvester and the power loading curves were generated by placing a digital IET Labs load resistor in series with the harvesters. The output signal from the accelerometer was conditioned using a charge amplifier (Piezotronics Inc.). The velocity at the tip of cantilever beam was measured using a digital vibrometer (Polytec OFV 353). Polytec 5000 controller was used to generate input signals to the seismic shaker to create vibration and also to capture the output signals from accelerometer and vibrometer. The

velocity FRF's for each harvester was measured by clamping each of them and facing the laser head.

Results and Discussion

The saturation magnetostriction of the ferrite film was measured to be 12ppm and the saturation occurs at 1767Oe.

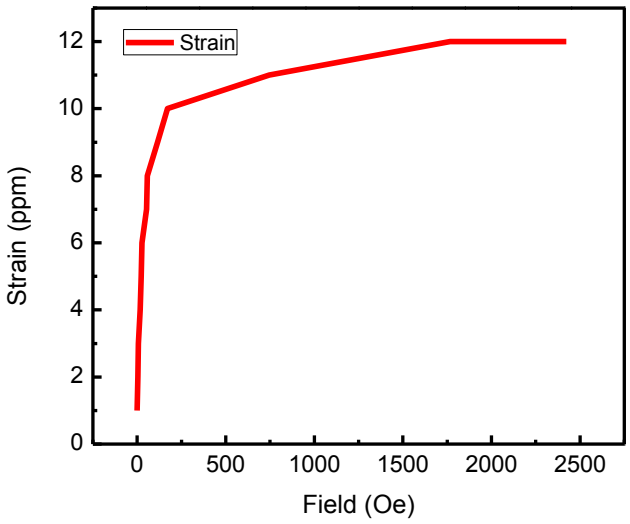

Figure 7.5 Magnetostriction results for Electroscience Type 40011 ferrite

The resonant frequency and ME voltage coefficients for the 0.5mm thick ferrite ME composites operating in d_{31} and d_{33} modes is shown in Fig. 7.6 and listed in Table 7.1. The applied AC magnetic field was 1Oe at 1kHz with a saturation DC magnetic bias of 21.9Oe and 27.8Oe respectively for the 0.5mm and 0.6mm ferrite ME composites. In ME laminates, the first longitudinal frequency is proportional to the inverse of its length whilst for asymmetric ME laminates like an ME unimorph, the first bending resonance is lower than that of the longitudinal and proportional to the inverse of composite length[8] [9]. This explains the low resonance

frequencies of the d31 and d33 ME unimorphs prior to their singulation into ME fibers. The ME voltage coefficients are shifted to the left on the d33 mode vs. the d31mode as the d33 mode electrode pattern is electrically unidirectional whilst the d31 mode pattern is bidirectional. In addition, a 2^{nd} resonance was obtained close to the first. For an unclamped rectangular plate, the frequency ratio between the 2^{nd} and 1^{st} modes for length:width ratios[10] of 1, 1.5 and 2.5 are 1.47, 1.07 and 1.53. For a clamped rectangular cantilever, the same ratios are 2.44, 3.56 and 5.21. From the table below, the ratio between modes for our slightly rectangular plates (1 < length:width ratio < 1.5) range between 1.26-1.63. Unlike the piezo which were diced into 21mm squares, the square ferrite LTCC tapes were sintered into non-square and slightly rectangular shapes. For further confirmation, we fabricated a d_{31} mode piezo similarly sized and shaped as the ferrite and conducted a frequency impedance analysis. Its 1^{st} resonance was at 59.6 kHz with a 2^{nd} mode at 87.6 kHz and 80.6 kHz with a 2^{nd} mode at 97.8 kHz for d33 and d31 modes respectively – a mode ratio of 1.47 and 1.21 respectively. A perfectly square resonator is known to have a whispering gallery effect, that is a single high quality factor resonance due to combination of both x and y lateral modes[11]. Therefore, the 2^{nd} peak is due to the 2^{nd} mode of a free-free-free-free slightly rectangular plate.

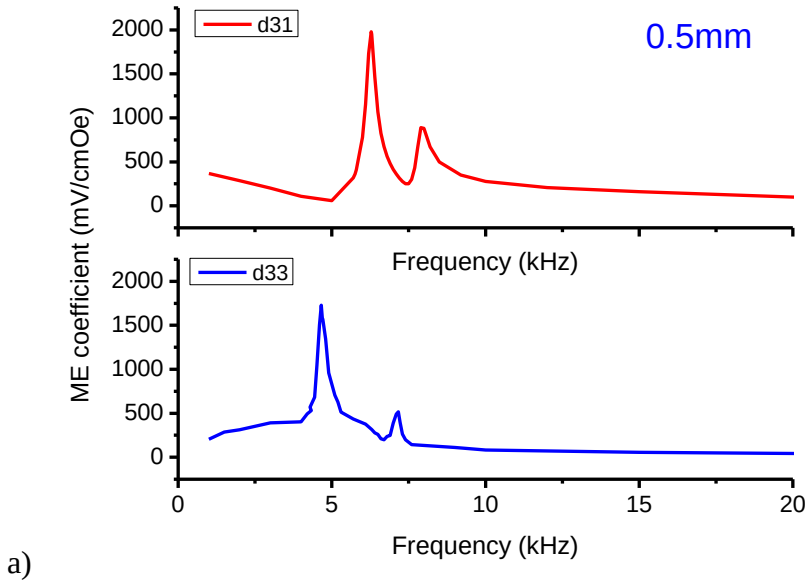

a)

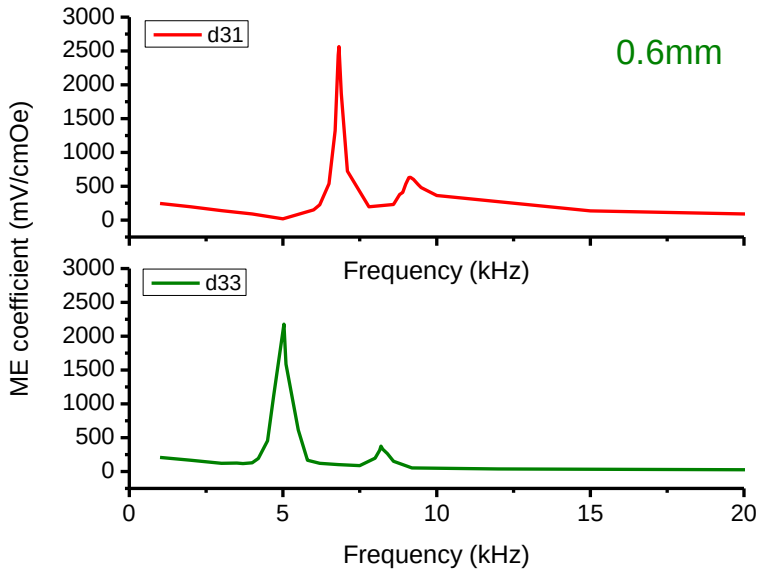

b)

Figure 7.6 Magnetoelectric voltage coefficient results for a) 0.5mm Ferrite and b) 0.6mm Ferrite ME composites operating in d31 and d33 modes.

Table 7.1: Summary of the ME voltage results for ME composites vs. Ferrite thickness

		Ferrite Thickness(mm)					
		0.5			0.6		
	mode	1st	2nd	Ratio	1st	2nd	Ratio
Frequency response (kHz)	d31	6.31	7.98	1.26	6.82	9.15	1.34
	d33	4.66	7.15	1.53	5.04	8.19	1.63
ME coeff. (mV/cmOe)	d31	1985	893		2574	634	
	d33	1730	515		2177	376	

It has been reported that the L-L mode (longitudinal magnetized-longitudinal poled) has the largest ME voltage coefficient of all the four basic modes namely longitudinal-longitudinal (L-L), transverse-longitudinal (T-L), L-T and T-T[9]. This is usually assumed to be due to the higher longitudinal piezoelectric coefficient d33 over the transverse coefficient d31. In case of a push-pull type configuration where the ME composite consists of numerous ME elements with adjacent piezo elements poled in opposite directions, the ME voltage coefficient was found to be better due to the higher elemental capacitance[9]. Despite the fact that this higher capacitance is in parallel across the IDE pairs, the total device capacitance was extremely low for a fiber based piezoelectric device and causes the required matching load impedance to be greater. Two ME MFC's, with ferrite thicknesses of 0.6mm and 0.5mm, operating in d_{33} .mode achieved open circuit voltage of 101.11mV and 93.84mV (ME voltage coefficient of 1667 mV/cmOe and 1564 mV/cmOe). The peak power was found to be 1.987nW across 555kΩ and 1.718nW across 510kΩ matching resistor load. The measurements were conducted at 264Hz and 259Hz frequency with applied DC magnetic bias of 35Oe and an AC magnetic field of 4Oe respectively.

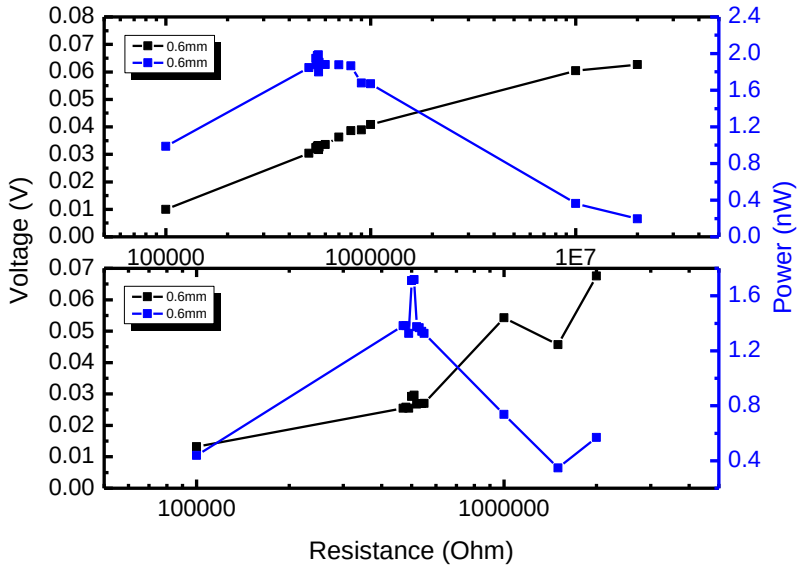

Figure 7.7 Voltage and power loading curves for 0.5mm (top) and 0.6mm (bottom) ME composite MFC's.

Due to the 995kΩ resistance of the data acquisition system (which is in parallel to the 555kΩ and 510kΩ matching resistor loads for the 0.6mm and 0.5mm ferrite ME MFC's), the effective load seen by the transducer were 356kΩ and 337kΩ for the two ME MFC's of ferrite thickness of 0.6mm and 0.5mm respectively. This matching impedance amounts to an effective electrical capacitance of 1.69nF and 1.82nF, respectively. After dicing, MFC fabrication and poling, the measured capacitance was 0.14nF and 0.118nF at 1kHz respectively. The discrepancy between the capacitance calculated from the matching impedance and that measured prior to poling maybe due to a) the frequency difference between the capacitance measurement and that of the operation and b) resonant operation of the magnetically induced vibration of the piezoelectric. As shown in the inset of Fig. 7.8(a), the ferrite has a low coercive field of the order of ~20 Oe. The lowest effective longitudinal field that was achievable was ~35 Oe.

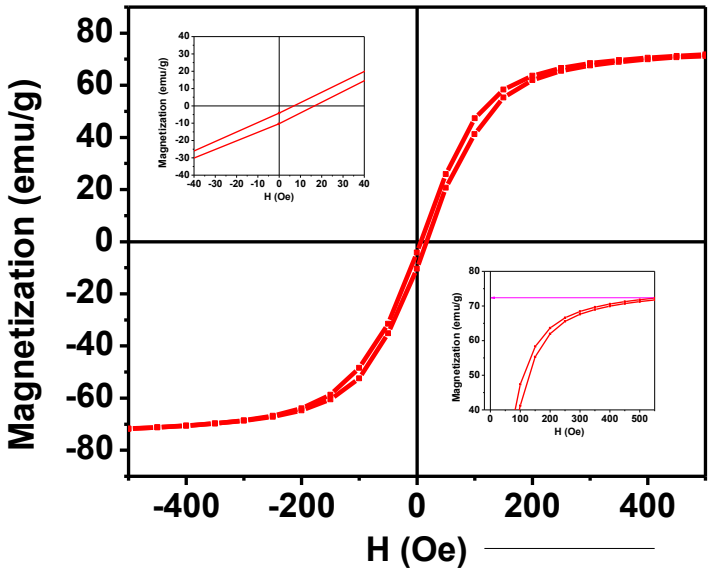

a)

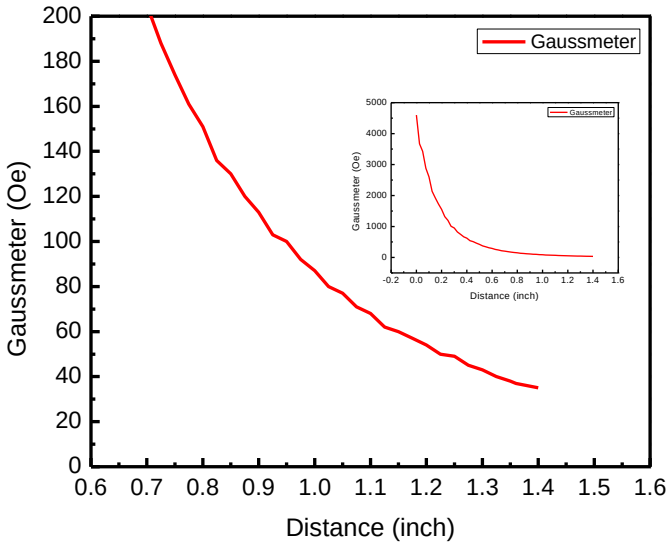

b)

Figure 7.8 a) Magnetization-Field (M-H) hysteresis loop for the Electroscience Ferrite 40011 and b) the effective DC Magnetic bias achievable by using a longitudinally translatable NdFeB magnet

We would like to achieve <100Hz simple cantilever based application and for doing so, the following options are available: a) add an inertial tip mass, b) decrease stiffness of the support

and c) decrease stiffness of the Magnetoelectric composite. The stiffness of the support, the Copper IDE kapton flexible circuit can be adjusted by using a tape with less copper (less copper thickness, more space between copper lines, etc), thinner kapton and low elasticity epoxy between the copper. The stiffness of the ME composite can be adjusted by using lesser thickness of the magnetostrictive and piezoelectric materials and that of the epoxy in between the ME fibers.

Conclusion

We developed a low temperature jet vapor solder bonded (<125 ^{o}C) magnetoelectric composite fibers and incorporated them with kapton based copper flexible circuit using a room temperature curing epoxy. With this bonding approach, we achieved an ME voltage coefficient of 1667 mV/cmOe and 1564 mV/cmOe at 264Hz and 259Hz for 0.6mm and 0.5mm ferrite based MFC's. The resulting magnetoelectric macro fiber composites provided low frequency energy harvesting capability under vibration and magnetic field. Further work is required to optimize the power generation capability of these magnetoelectric macro fiber composites.

Acknowledgements: The authors gratefully acknowledge the financial support from ***Air Force Office of Scientific Research (AFOSR)*** *through Young Investigator Program* and Office of Basic Energy Science, Department of Energy (S.P.). We are also greatly indebted to Justin Farmer CEHMS Laboratory manager for help with the experimental setup. We also would like to thank Bret Halpern of Jet Process Corporation, North Haven, CT for the solder deposition and T.J. Belton and Travis Belton of Moog Components Group Galax Operations, Galax, VA for flexible circuit fabrication.

References

[1] Nan C-W, Liu G, Lin Y. Influence of interfacial bonding on giant magnetoelectric response of multiferroic laminated composites of Tb[sub 1 - x]Dy[sub x]Fe[sub 2] and PbZr[sub x]Ti[sub 1 - x]O[sub 3]. Applied physics letters 2003;83:4366.

[2] Liu G, Nan C-W, Cai N, Lin Y. Dependence of giant magnetoelectric effect on interfacial bonding for multiferroic laminated composites of rare-earth-iron alloys and lead--zirconate--titanate. Journal of Applied Physics 2004;95:2660.

[3] Gheevarughese V, Laletsin U, Petrov V, Srinivasan G, Fedotov N. Low-frequency and resonance magnetoelectric effects in lead zirconate titanate and single-crystal nickel zinc ferrite bilayers. JOURNAL OF MATERIALS RESEARCH-PITTSBURGH THEN WARRENDALE-2007;22:2130.

[4] Zhao P, Zhao Z, Hunter D, Suchoski R, Gao C, Mathews S, Wuttig M, Takeuchi I. Fabrication and characterization of all-thin-film magnetoelectric sensors. Applied physics letters 2009;94:243507.

[5] Park C-S, Priya S. Cofired Magnetoelectric Laminate Composites. Journal of the American Ceramic Society 2011;94:1087.

[6] MacDonald WD, Eagar TW. Transient Liquid Phase Bonding. Annual Review of Materials Science 1992;22:23.

[7] Roman JW, Eagar TW. Low stress die attach by low temperature transient liquid phase bonding. PROCEEDINGS-SPIE THE INTERNATIONAL SOCIETY FOR OPTICAL ENGINEERING: SPIE INTERNATIONAL SOCIETY FOR OPTICAL, 1992. p.52.

[8] Wan JG, Li ZY, Wang Y, Zeng M, Wang GH, Liu J-M. Strong flexural resonant magnetoelectric effect in Terfenol-D/epoxy-Pb(Zr,Ti)O[sub 3] bilayer. Applied Physics Letters 2005;86:202504.

[9] Zhai J, Xing Z, Dong S, Li J, Viehland D. Magnetoelectric Laminate Composites: An Overview. Journal of the American Ceramic Society 2008;91:351.

[10] Blevins RD. Formulas for natural frequency and mode shape. New York: Van Nostrand Reinhold Co., 1979.

[11] Wei-Hua G, Yong-Zhen H, Qiao-Yin L, Li-Juan Y. Whispering-gallery-like modes in square resonators. Quantum Electronics, IEEE Journal of 2003;39:1106.

Chapter 8

Design, Modeling and Experimental Verification of Low Frequency Resonant Piezo MEMS Structures for Energy Harvesting

Ronnie Varghese, [1] Shree Narayanan, [2] Donald Leber, [2] and Shashank Priya[1,*]

[1]Center for Energy Harvesting Materials and Systems (CEHMS), Bio-Inspired Materials and Devices Laboratory (BMDL), Virginia Tech, Blacksburg, VA 24061, USA
[2]Electrical and Computer Engineering Department, Virginia Tech, Blacksburg, VA 24061, USA

Abstract

In this paper, we report the development of a low frequency (<100Hz) resonant piezo MEMS structures for energy harvesting. The structures were fabricated on platinized silicon wafer and bulk piezo material. $Pb(Zr,Ti)O_3$ (PZT) piezoelectric thin film was rf sputtered on platinized silicon. PZT thin film properties were optimized for energy harvesting by improving the texture degree with respect to the underlying platinized Si substrate. The silicon MEMS fabrication process flow consisted of two modules – a) the mechanical module wherein the Si cantilever structures were created and b) the electrical module for PZT capacitor formation. This simplified process flow reduces the number of unit operations by ~40%. Using this modular approach, we studied different cantilever structural designs and based on this learning, conceived a low frequency structure that resembles a circular labyrinth. We describe various methodologies for modulation of the natural frequency of a cantilever by varying its cross section dimensions along three axes. For electrical testing under vibration, a wafer level tester was engineered using gold plated pogo pins on a custom printed circuit board. As an alternative to cleanroom based Si

micromachining processes, circular labyrinth structures were also manufactured from Piezo sheets, unimorphs and bimorphs using a novel non cleanroom micromachining technique called microwater jet cutting. This structure has demonstrated <100Hz resonant operation without a tip mass.

Keywords: Piezoelectric MEMS; energy harvesting; Silicon micromachining; texturing; frequency tuning

Introduction

Micro scale low frequency energy harvesting has been mainly dominated by inductive or electromagnetic devices [1, 2]. However, the miniaturization of such devices is limited by the size of the magnet used as the inertial mass and the size of the coil that can be fabricated in the MEMS scale. Consequently, for MEMS scale energy harvesting, piezoelectricity is the transduction of choice and especially due to its compatibility with cleanroom based silicon micromachining techniques. However, the resonance increases to kHz range on scaling down low frequency piezoelectric devices to MEMS sizes. Use of large inertial masses on simple single cantilever beam structures have been reported for low frequency MEMS energy harvesting[3]. An S-shaped MEMS cantilever system was capable of achieving < 30Hz but required a substantially large tip mass[4]. Such structures are limited in their power due to the size of the piezoelectric element. Low frequency structures with larger piezoelectric functional areas would increase the energy conversion.

We report on a new tip mass free low frequency vibration energy harvesting structure that is capable of attaining resonant frequencies of less than 100Hz with less torsion than spiral designs[5] and with a smaller foot print than zigzag [6] or meandering [7] structures. This

structure, named Circular Labyrinth or Zigzag, has achieved <100Hz resonant operation both on the Si MEMS platform and with bulk Piezo material. For Si wafer based fabrication, we report a new Piezo MEMS Si micromachining process flow which has fewer steps and is simpler to implement whilst for bulk Piezo, we reveal a new approach of micromachining using a micro water jet. Non Si wafer based micromachining has been attempted earlier by laser micromachining – either by laser shaping LTCC tape and then cofiring the shaped tape [8] or using laser cutting piezo sheets directly[9]. The former is a very elegant way but the laser cut tape will shrink during sintering and if not carefully sintered can crack across the corners. The latter is plagued by a heat affected zone that can degrade the piezo properties (by amorphization and lead loss) in that area of the laser cut cantilever. Micro water jet cutting overcomes such concerns as it uses a ultrasonic water jet to ablate the piezo material in a required pattern.

Experimental Procedures

Silicon Micromachining

For wafer size deposition of PZT thin films, one can either employ sol-gel or RF sputtering. We chose RF sputtering due to a) higher deposition rates, b) ease of depositing over topography, c) ability to control stress and d) ability to integrate into a 'mechanical-first' Piezo MEMS fabrication process. Unlike the standard 'electrical first' fabrication process[10], the vibrational structure is defined and created and then the electrical module with its PZT capacitors is processed.

Our fabrication process is split into two –mechanical and electrical modules. The mechanical module consisted of silicon micromachining processing steps. The electrical module comprised of steps to fabricate the PZT capacitive elements of PZT thin film sandwiched between 2 Pt

electrodes. We use 2 shadow masks for a combined bottom Pt and PZT and top Pt depositions respectively. All wet etch processes are thus avoided. After development of our process flow and fabrication process, we came across a more complicated mechanical-first process that utilizes screen printed thick PZT[11]. The electrical module thin film stack consist of 3000A Pt over 1 micron PZT of 2 different stoichiometry's, $Pb(Zr_{0.60}Ti_{0.40})O_3$ and $Pb(Zr_{0.52}Ti_{0.48})O_3$, over 3000A Pt with an adhesion layer of 100A Ti. The substrates were 700C O_2 annealed PECVD SiO_2 coated 0.5mm Si p(100) wafers (has a minor flat at 90 to the major flat permitting easy assignment of front and back side processing steps). PZT RF sputtering and Pt DC sputtering was conducted on Aja International ATC Orion system whilst the Ti deposition was conducted on Kurt Lesker PVD 75E-beam evaporator.

Table 8.1 Unit Operation detail of the 2 modules in a Piezo MEMS process flow

When the modules are combined, our process is unique in that each module is processed on a specific side of the silicon wafer. Traditionally, dual side processing is required to define the cantilever. Without the use of an SOI wafer, the cantilever beam thickness is defined first by a short Deep Reactive Ion Etch (DRIE) from the front side and then a backside DRIE is conducted to release the structures[12]. We have developed a self-aligned and self-isolated MEMS

fabrication process capable of fabricating vibrational structures with an inertial tip mass and with only 2 photo lithography steps. The key feature of this process is the use of a patterned SiO_2 hard mask to define the beam thickness in the DRIE and then after removal of that SiO_2 hard mask, using a 2nd patterned photoresist mask to proceed with a 2nd DRIE to release the cantilever. Unlike the process used for the unreleased MEMS structure of a Piezo accelerometer[13], our process is developed to a) in situ remove the SiO2 hard mask before the 2nd DRIE and b) then conduct the 2nd DRIE to the front side for release. The removal of the SiO_2 hard mask after the 1st DRIE can be skipped in some cases and the DRIE SiO_2:Si etch rate selectivity can be utilized to define the cantilever beam thickness. That is, after SiO_2 hard mask definition and 1st DRIE, the 2nd DRIE mask pattern is applied but SiO_2 need not be removed. This inorganic hard mask will etch slower than Si and thus when the Si DRIE reaches the front of the wafer, the sections that were covered by SiO_2 would have lagged behind during etch and would be thicker.

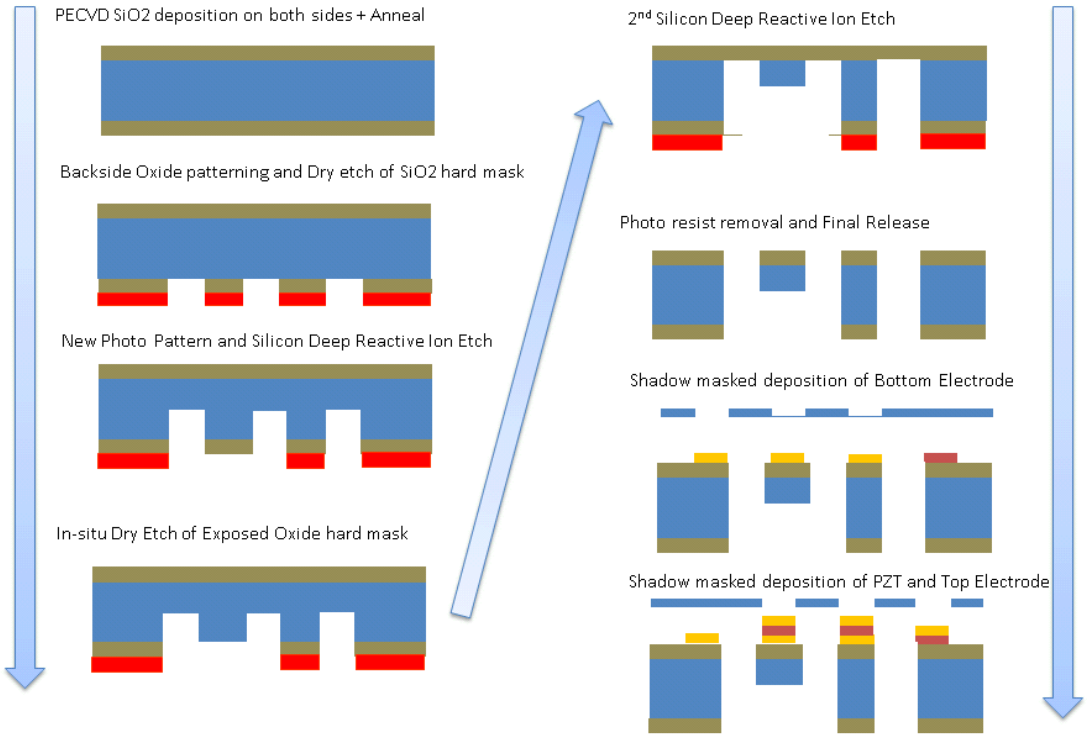

Figure 8.1 New Self aligned Mechanical First Electrical Last process

Bulk Piezo Micromachining

PZT has a lower Young's modulus of elasticity than Si (60 vs 169 GPa) and therefore a cantilever fabricated out of bulk piezo can be presumed to have lower resonant frequency for the same shape and beam thickness. Bulk piezo materials like sheets, unimorph and bimorphs etc can be machined using a) CNC (via size limited by drill bit size, dirty process with cooling fluid) b) Laser ablation (Slag formation and damage to PZT; low throughput and speed; high cost per device; via sizes <200 microns possible albeit with slag areas of at least 20 microns) and finally c) Micro water jet (no damage to PZT; high throughput and speed; cost per device 2/3rd of laser; ~200um wide via possible; clean process as part is only exposed to water and cutting debris). Micro Electric discharge machining (EDM) was ruled out as it cannot cut nonconductive ceramics. Microwaterjet processing prefers a leading edge for start of cut, requires that the material is loaded onto a fixture (preferably metal) and can provide via widths of ≥ 200microns. We used PSI-5H4E Piezo sheets and T215-H4-503X series poled bimorphs. Despite the fact that series poled bimorphs require higher matching loads, they were chosen as numerous reports claim the high power and voltage generating benefits of series poled over parallel poled bimorphs [14-16]. The unimorphs were made in house by bonding Ni Alloy 201 from McMaster-Carr to the aforesaid Piezo sheets. These piezo sheets and composites were then micro water jet cut into the new low frequency structure reported in this paper.

Wafer level Characterization - Mechanical

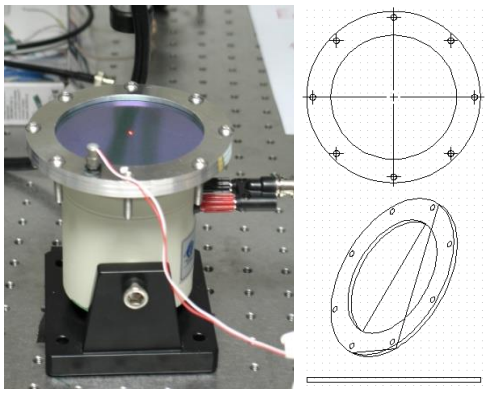

Figure8.2 Vibration testing setup with perimeter clamping of MEMS wafer

For mechanical testing of MEMS wafers, a Polytec MSA 500 was used with a special clamp that clamps the wafer along its edges (figure above). As the shaker is moving the whole wafer and all its MEMS devices simultaneously, we scan each cantilever from tip to base and take the transfer function between the tip and base to compute the resonance frequency. Typical 3D animation plots of the actual vibration characteristics are shown below (figure below).

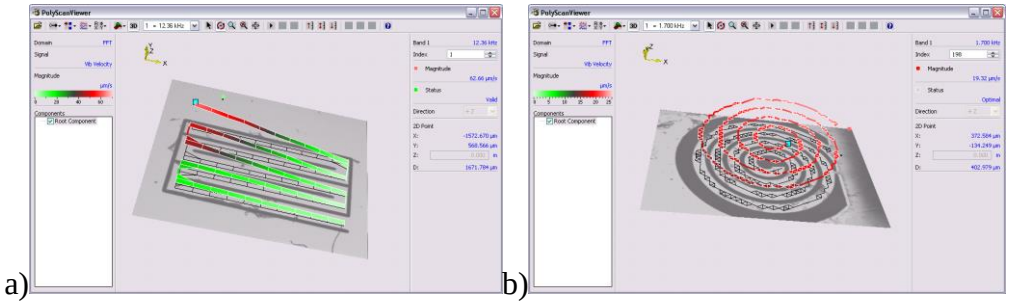

Figure 8.3 Animation plots of the Velocity FRF at fundamental resonance of a) a linear zigzag and b) a circular spiral

We utilized a cantilever type (the harvester is clamped in free-clamped mode) Aluminum clamp mounted onto a TMC Solution TJ-2 electromagnetic shaker which was powered by an HP 6825A power supply/amplifier operating as a fixed gain amplifier. SigLab 20-42 data acquisition system with four input channels and two output channels is used for the Voltage frequency response function (FRF) measurements. This data acquisition system has an internal resistance of 995kΩ

and this resistance was in parallel with any load resistance attached externally to the device under test. The reference acceleration was measured at the clamp using an accelerometer (Piezotronics Inc. model # U352C67). Voltage generated by the harvester and the power loading curves were generated by placing a digital IET Labs load resistor in series with the harvesters. The output signal from the accelerometer was conditioned using a charge amplifier (Piezotronics Inc.). The velocity at the tip of cantilever beam was measured using a digital vibrometer (Polytec OFV 353). Polytec 5000 controller was used to generate input signals to the seismic shaker to create vibration and also to capture the output signals from accelerometer and vibrometer.

Wafer level Characterization - Electrical

At present, MEMS harvesters are tested individually after the wafer has been singulated by dicing. This requires that the MEMS device be packaged or temporarily glued to a special carrier wafer to protect the MEMS structures from damage during dicing. Prior to packaging and singulation, we decided to employ wafer level testing and to do so we introduced a novel concept of using wafer probe cards fabricated from a PCB with Gold plated pogo pin probes (figure below). Eagle^{TM} software was used to lay out the pogo pin locations and route the wiring pads to the perimeter of the PCB. All wiring is thus confined to the outside of the test setup and do not interfere with the Laser Vibrometry measurement. This approach is especially useful if one has numerous devices on a wafer (we have 88 different cantilevered devices on our mask layout).

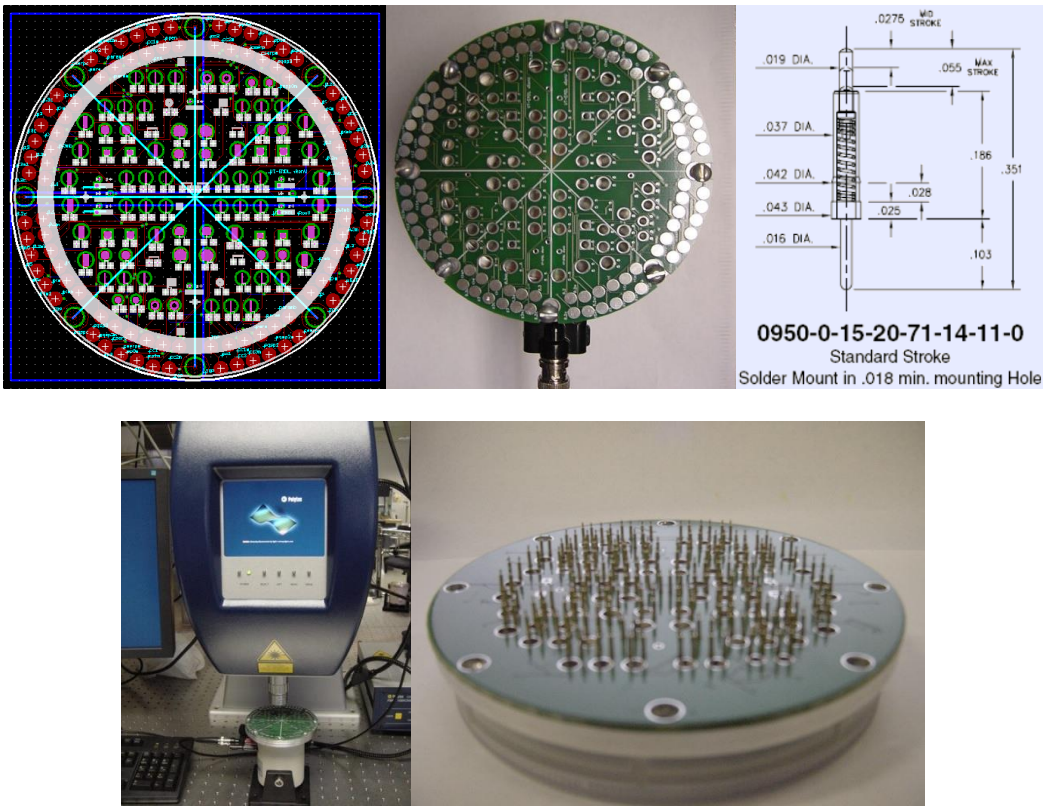

Figure 8.4 Electrical test setup: (clockwise from top left) PCB layout design, as manufactured, with pogo pins soldered on and finally clamped over a device wafer

Results and Discussion

Electrical Module

Thin Film Development

PZT thin film was cold sputtered from internally formed targets of 2 stoichiometry's, $Pb(Zr_{0.60}Ti_{0.40})O_3$ and $Pb(Zr_{0.52}Ti_{0.48})O_3$(hitherto referred to as PZT 60/40 and PZT 52/48

respectively), onto 2 platinized Si substrates – from Inostek (Korea) which has a 1500A Pt (111)/100A Ti/ 3000A SiO_2/Si stack vs. our stack of 3000A Pt/100A Ti/ 10000A SiO_2/Si. The XRD patterns (shown below) from the 2 substrates clearly show random texturing of our Pt vs. Inostek's highly (111) Pt.

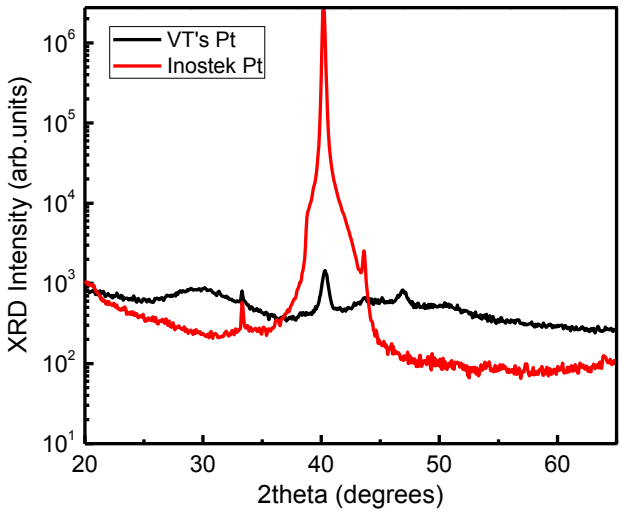

Figure 8.5 XRD pattern of Inostek (red) vs. our Platinized Si

PZT thin films of (100) orientation near the morphotropic phase boundary has the highest piezoelectric performance [17, 18]. As a) PbO seed layer has been theorized to generate (100) texturing of PZT [19] and b) PbO has a very high vapor pressure, we annealed our platinized Si substrates in closed (but not air tight) environment along with PbO powder. We postulated that the PbO will sublime on heating and then on cooling would condense on the Pt. However from the figures below, PbO sublimation at 600°C for 5hrs seemed to randomize the PZT structure irrespective of whether it was sputtered or sol-gel PZT.

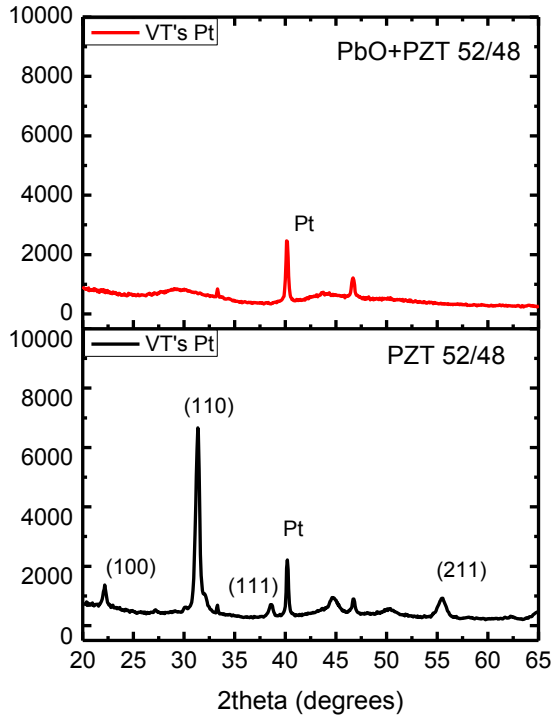

a)

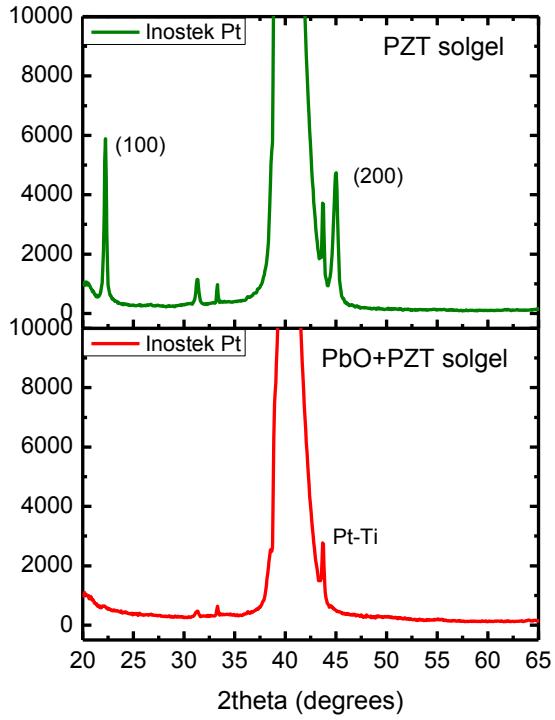

b)

Figure 8.6 a) sputtered PZT 52/48 and b) sol-gel PZT 60/40 on PbO sublimed over Inostek platinized Si

As oxidizing the Ti adhesion layer can provide a textured Pt surface[20], we proceed to pre-anneal our platinized Si at 700°C in a pure O2 environment. We can see that PZT 52/48 is more textured, albeit more (110) than (100), on the oxygen annealed platinized Si.

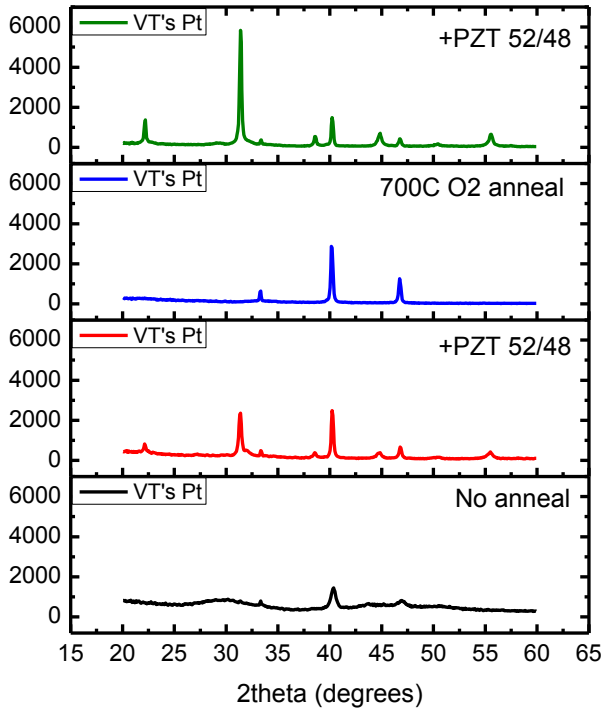

Figure 8.7 Effect of Oxygen pre-annealing of our platinized Si on PZT texturing

As the sputter yield of Pb, Zr and Ti in an Ar plasma environment differs by the elastic collision cross section between sputtering ion Ar and the elements in the target, the stoichiometry of the deposited thin film cannot be expected to be the same as that of the PZT target. Therefore we studied the dependence of PZT texturing on the target composition. Clearly, PZT 60/40 target provided more (100) and (111) texturing than PZT 52/48.

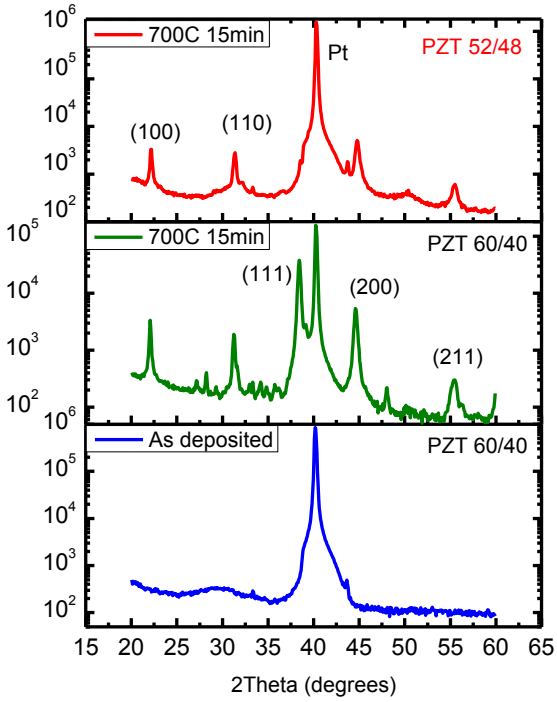

Figure 8.8 PZT texturing dependence on stoichiometry of the sputtering target

Since a) the piezoelectric coefficient in d33 mode is almost twice that in d31 mode and b) traditionally used ZrO2 charge barrier layer deposition was not available, we investigated the use of Atomic layer deposited (ALD) Al2O3 and HfO2 on PZT texturing. From the figure below, both amorphous ALD films seem to randomize the PZT.

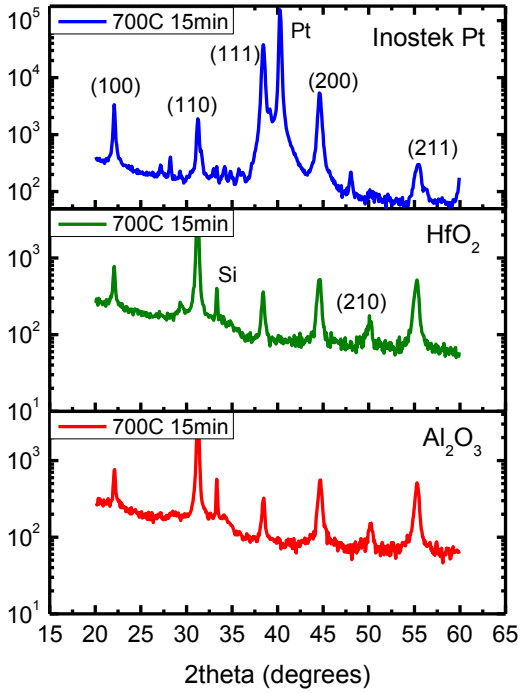

Figure 8.9 Effect of ALD thin films of Al2O3 and HfO2 on PZT texturing

Mechanical Module

X-Y Cross section variation

The pictures below depict clockwise from top left – 300um width, 200um cantilever, Taper wider end clamped (300um to 200um), Parabolic (300um to 200um to 300um) , Taper narrower end clamped (200um to 300um) cantilevers and finally a Bezier. All these cantilevers have the same length and thickness, have beziers at their clamped end and vary only along their widths. The resonance frequency is in the order (Table 8.2 8.2), Taper wider end clamped > 300um=200um > Parabolic > Taper narrower end clamped and for each type. Tapering wider end towards clamp is similar to the triangular and trapezoidal shaped harvesters reported already

reported in literature [21-24]. For similar footprint as an equivalent rectangular device, such devices have been shown to have much higher power output as these cantilevers have wider clamped ends (where the stress is maximum).

Adding a Bezier at the clamped end increased the frequency slightly. Adding such trapezoidal or even a circular Bezier, spreads the stress distribution near the clamp, improves the tolerance to acceleration, and alleviates residual stress induced cantilever breakage but sometimes at the cost of power reduction[25]. But if the Bezier is less than 20% of the length of the beam, there is considerable improvement in power harvested due to a) larger stress distribution and b) higher accelerations possible.

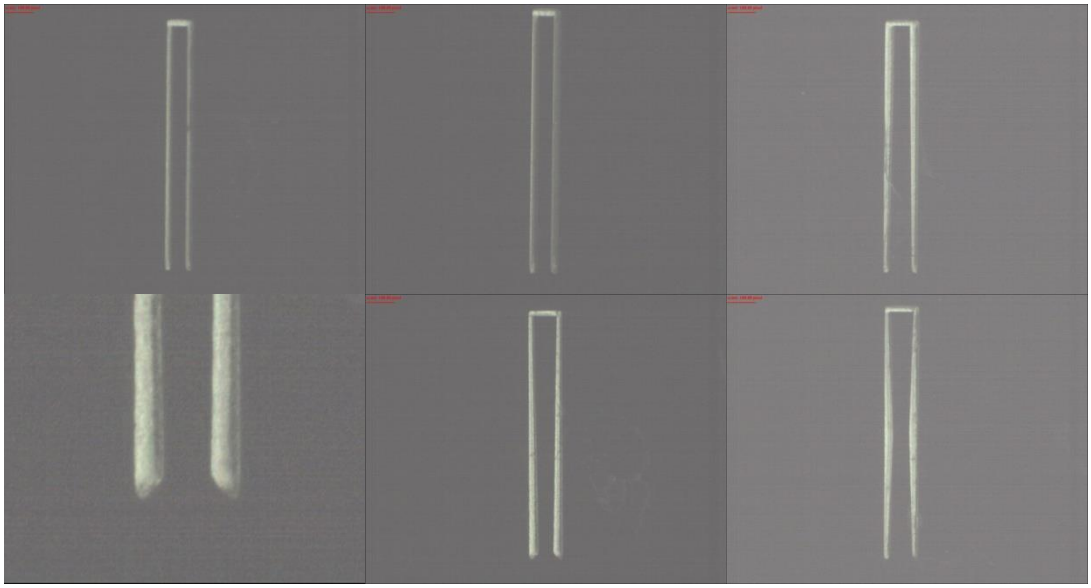

Figure 8.10 Cantilevers with varying widths and a Bezier at clamped end

Table 8.2: Fundamental resonance of cantilever structures with varying widths

		Resonance(kHz)	
		Model	**Actual**
300um	with bezier		68.720
		77.628	68.298
200um	with bezier		70.860
		77.539	70.123
Taper_wider end clamped (300um > 200um)	with bezier		80.090
		87.503	78.775
Parabolic	with bezier		70.631
		77.144	68.583
Taper_thin end clamped (200um > 300um)	with bezier		62.656
		68.560	60.083

Z Cross section variation

Natural frequency of MEMS vibrational structures are determined by their dimensions. Once designed into fabrication, modulation of frequency is difficult to achieve at wafer level or across multiple structures at the same time. We propose a simple scheme that when incorporated into the MEMS fabrication process can vary the frequency up or down from that in the original design. For example, if there are 5 structures each designed for 10kHz, 15kHz and 20kHz, we can vary each of those 5 structures per frequency group as follows: for the 10kHz group, we can have a structure each at 9.6, 9.8, 10, 10.2, 10.4 KHz.

Without a tip mass, the fundamental freqeuency of a Piezo MEMS cantilever is calculated-:

$$f_n = \frac{\nu_n^2}{2\pi}\frac{1}{l^2}\sqrt{\frac{D_p}{m}} \qquad (1)$$

where

$$D_p = \left[E_p^2 t_p^4 + E_s^2 t_s^4 + 2E_p E_s t_p t_s \left(2t_p^2 + 2t_s^2 + 3t_p t_s\right)\right] \times \left[12(E_p t_p + E_s t_s)\right]^{-1} \quad (2)$$

With a tip mass, the above equation transforms into -

$$f_n' = \frac{v_n^2}{2\pi}\sqrt{\frac{0.236 D_p w}{(l - l_m/2)^3(0.236 m w l + \Delta m)}} \quad (3)$$

In the design phase of the device, the adjustable parameters are : a) l_m , length of inertial mass, b) l, length of beam, c) Δm, inertial mass and d) w_p , width of beam. But during fabrication, there is variability across and within wafers. To tune the frequency into specification, we have use another approach. From above equation, to change D_p, we can change thickness of Piezo layer t_p or Support beam Silicon t_s. The thicker layer will have the largest effect on variation in D_p and which in our case is Silicon t_s. So our simple scheme is to vary the thickness of the vibrational structure either decreasing (increase frequency) or increasing from clamped end. For proof of concept, we designed these macro sized cantilevers (figure below) and studied their vibration characteristics (table below).

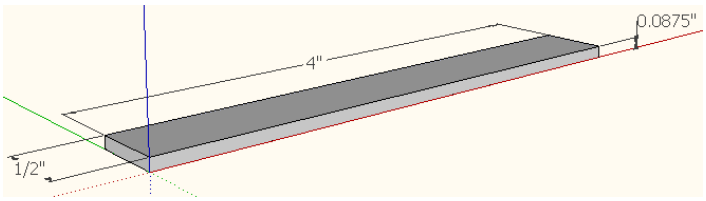

a)

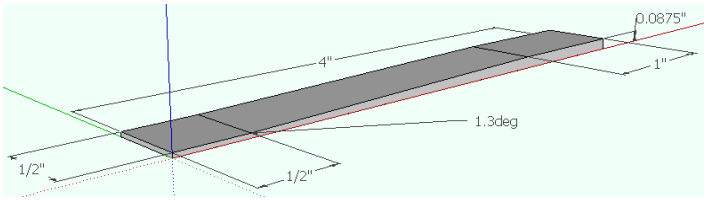

b)

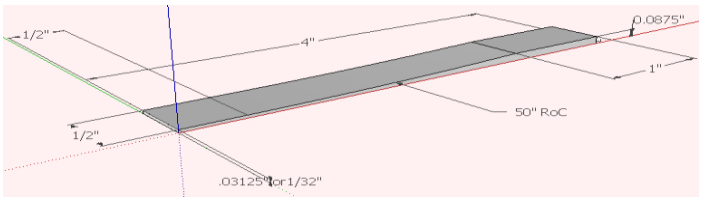

c)

Figure 8.11 a) Flat b) Angled and c) 50" Radius of curvature beam

Table 8.3 Fundamental resonance of cantilevers of varying thickness across their length

(Hz)	Flat	Radius - Clamped at thick end	Radius - Clamped at thin end	Angled - Clamped at thick end	Angled - Clamped at thin end
No mass	173.79	211.35	47.57	226.07	50.77
With tip mass	114.65	91.65	28.45	105.59	32.22

From the above table, the effect of which end is clamped and that of adding an inertial mass is pronounced. On adding a tip mass, the resonant frequency of the variable cross section beam decreases below that of the flat simple beam. In addition, for no tip mass, if the variable cross section beams are clamped on their thicker end, the frequency increases from that of the thinner end clamping and that of the flat beam. With a tip mass, a gradient in width decreases the frequency from that of the flat beam but the frequency of thicker end clamping is greater than thinner end clamping. This fact can be used for tuning of resonance frequency of MEMS beams inside the fab without changing the device layout dimensions (figure below).

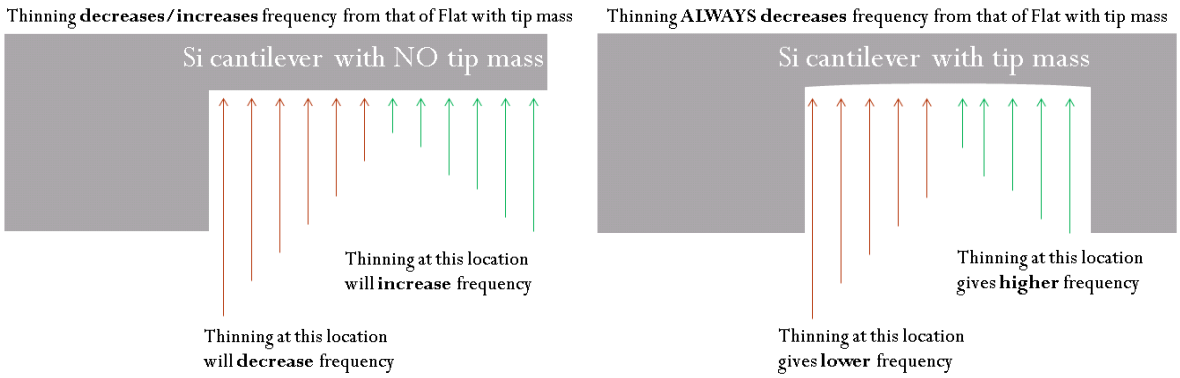

Figure 8.12: Proposed methodology to tune the frequency of partially or fully manufactured MEMS structures with tip mass

Low Frequency Structures

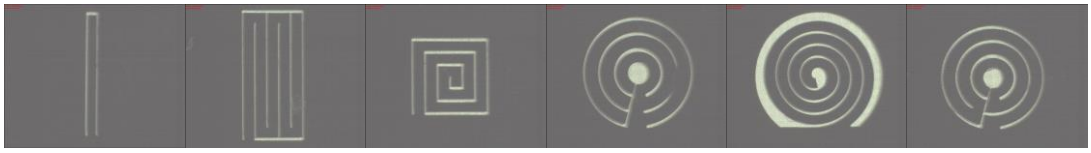

a)

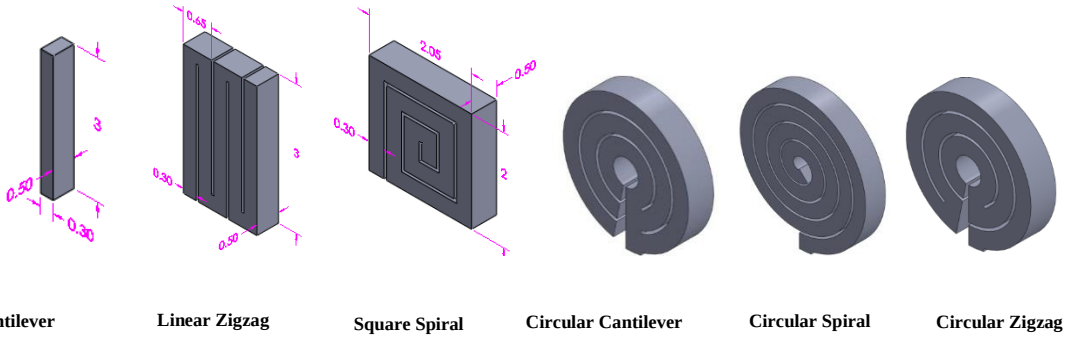

b)

Figure 8.13 Silicon MEMS cantilever structures a) As fabricated b) CAD-generated

The 1st resonance mode of various curvilinear and rectilinear wound structures (figure above) for full wafer thickness of 0.5mm is shown below. Clearly, the resonance of the 3 turn Circular

zigzag or labyrinth structure is similar to that of a similarly sized 3 turn spiral structure and dimensionally larger 5 beam zigzag.

Table 8.4 Fundamental resonance of non-linear cantilever structures

		Resonance (kHz)	
		Model	**Actual**
4 turn Circular Spiral		6.065	6.710
3 turn Circular Spiral		12.637	13.413
3 turn Circular Zigzag		12.938	13.406
2 turn Circular Zigzag		34.070	38.688
3 arc Circular cantilever	long arc	20.644	20.787
	middle arc	44.747	45.063
	short arc	76.514	77.370
2.5 turn Square Spiral		16.825	15.450
2 turn Square Spiral		40.345	36.190
3 beam Linear Zigzag		28.883	33.130
5 beam Linear Zigzag		13.464	13.550

We micro water jet cut 18mm diameter 4 turn and 5 turn Circular zigzag patterns in Piezo sheets, unimorphs and Bimorphs as shown below. The vias were a maximum of 235 microns wide.

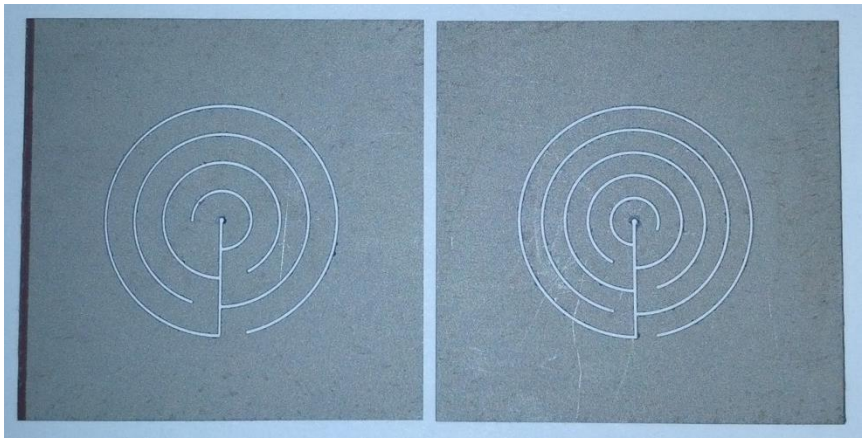

Figure 8.14 Micro water jet cut Piezo sheets – 4 turn Circular Zigzag on left and 5 turn on right

The vibration and harvesting characteristics at 0.1g acceleration are summarized below. Undoubtedly, the bimorph with its dual layer piezo has the best energy harvesting performance and all the piezo structures achieved < 100Hz performance without a tip mass. From the power loading (Voltage and Power vs. Matching resistance load) curves, we can clearly see that the optimal load varies with type of device and structure. Despite having almost similar surface areas (CZ4 = 246.01mm^2 vs. CZ5 = 243.08mm^2), CZ5 structure has a higher matching load than the CZ4 structure across all piezo stacks and expectedly so due to the lower resonance frequency of the 5 turn structure. The voltage performance shows that the strain created in these structures are independent of the number of turns.

Table 8.5 Vibration (0.1g) and Electrical Harvesting performance of the Micro water ject cut devices

Frequency (Hz)+/- 3dB	**Sheet**	**Unimorph**	**Bimorph**
CZ4	52.71 +/- 1	64.0+/-2.5	89.3 +/-5.7
CZ5	43.25 +/- 0.5	37.75+/-4.25	67.74 +/-4.97

Voltage (V_{oc} ,V)	**Sheet**	**Unimorph**	**Bimorph**
CZ4	0.138	0.567	1.842
CZ5	0.196	0.639	1.294

Power(µW)	**Sheet**	**Unimorph**	**Bimorph**
CZ4	1.02	5.466	52.89
CZ5	1.288	7.232	18.88

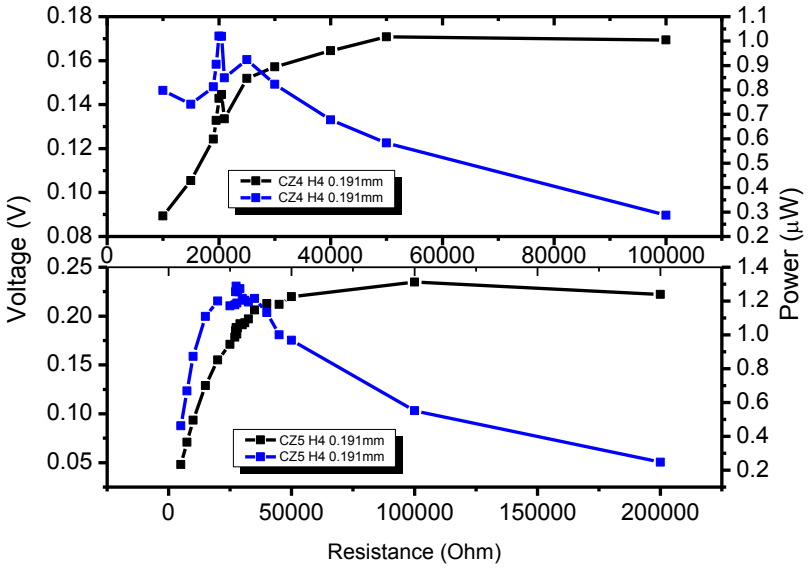
Voltage (V)
Power (μW)
Resistance (Ohm)
CZ4 H4 0.191mm
CZ4 H4 0.191mm
CZ5 H4 0.191mm
CZ5 H4 0.191mm

a)

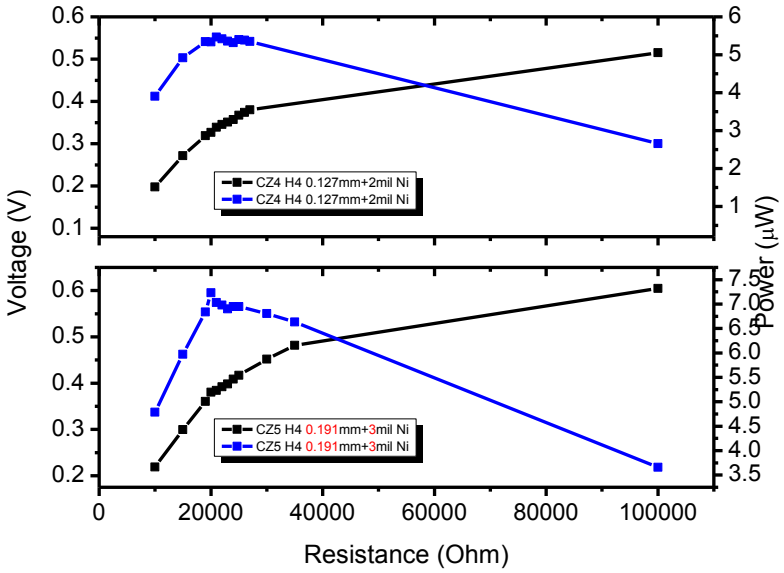
Voltage (V)
Power (μW)
Resistance (Ohm)
CZ4 H4 0.127mm+2mil Ni
CZ4 H4 0.127mm+2mil Ni
CZ5 H4 0.191mm+3mil Ni
CZ5 H4 0.191mm+3mil Ni

b)

c)

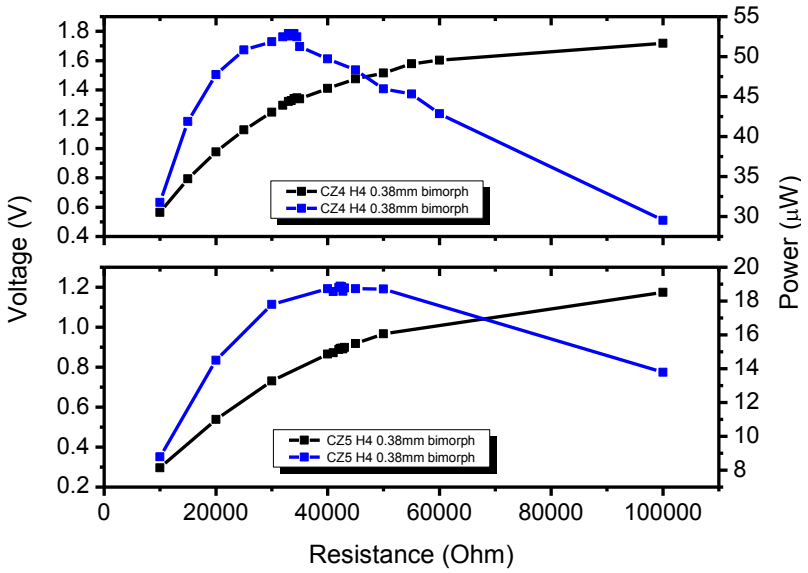

Figure 8.15 Power Loading curves for Piezo a) sheet b) unimorph (note the different Ni thickness used for each CZ structure) and c) bimorph

For d33 mode harvesting, we propose a new Chevron type angled interdigitated electrode (IDE) pattern that permits a) ensures that the inter-electrode distance is relatively constant with curvature of the cantilever (impossible with linear IDE), b) prevents premature dielectric breakdown at points in the pattern with smaller piezo gaps (with linear IDE, the gap at some locations can be closer than the others and cause dielectric breakdown during poling) and c) assist in the torsional mode harvesting as the change in angle is centered along the torsional axis of the beam.

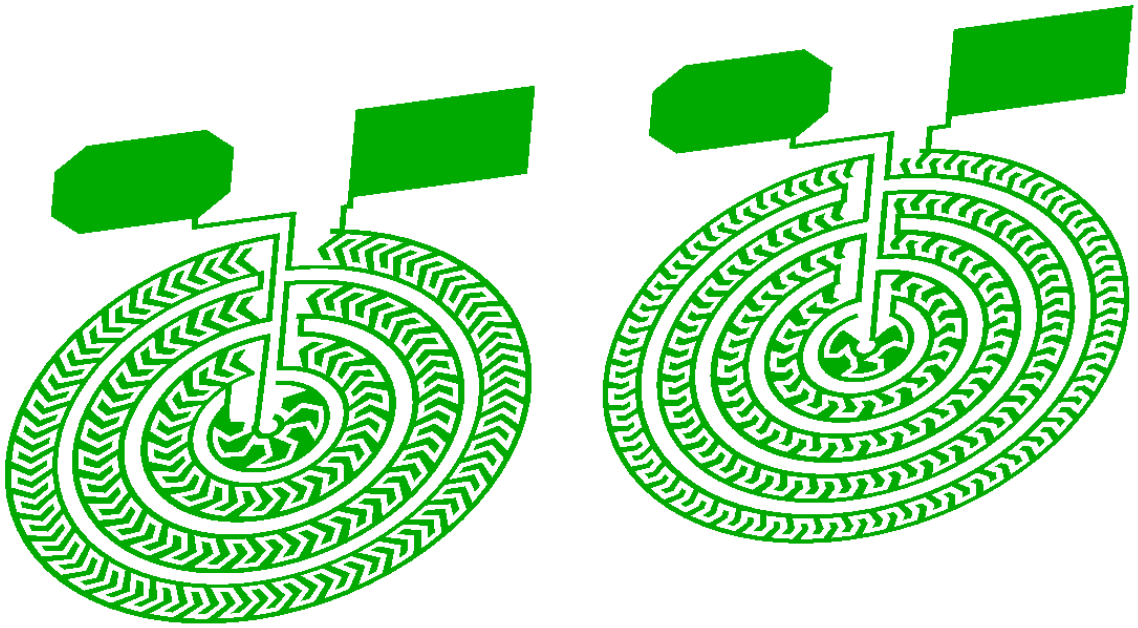

Figure 8.16 Chevron interdigitated electrode pattern for d33 mode energy harvesting

Conclusion

We have demonstrated the first tip mass free <100Hz resonant energy harvesting device by using a circular labyrinth vibration structure. We have utilized both Si and Piezo micromachining to fabricate these structures. We achieved an average of 1.15, 6.35 and 35.89 μW for Piezo sheet, unimorph and bimorph respectively. The exceptional energy harvesting performance of these structures was realized at very a low acceleration of 0.1g. 5 turn structure provides lower frequency and requires higher matching load. We describe various techniques for tuning the resonant frequency of MEMS cantilevers using variable cross sections in the x-y and z dimensions. We detail a novel approach to the Si wafer based Piezo MEMS fabrication process. A wafer level testing methodology has been developed for vibration MEMS testing. Finally, we

explain different techniques utilized to obtain the harvester constituent RF sputtered PZT thin films.

Acknowledgements: The authors gratefully acknowledge the financial support from ***Air Force Office of Scientific Research (AFOSR).***We are also greatly indebted our CEHMS colleagues, Anthony Marin, Amin Karami, and Reema Gupta for assistance with metrology assistance, Daniel Apo for ANSYS modeling and John Bird for PCB design and fabrication assistance.

References

[1] Jong Cheol P, Dong Hyun B, Jae Yeong P. Micro-Fabricated Electromagnetic Power Generator<newline/> to Scavenge Low Ambient Vibration. Magnetics, IEEE Transactions on 2010;46:1937.
[2] Wang P, Tanaka K, Sugiyama S, Dai X, Zhao X, Liu J. A micro electromagnetic low level vibration energy harvester based on MEMS technology. Microsyst Technol 2009;15:941.
[3] Shen D, Park J-H, Noh JH, Choe S-Y, Kim S-H, Wikle Iii HC, Kim D-J. Micromachined PZT cantilever based on SOI structure for low frequency vibration energy harvesting. Sensors and Actuators A: Physical 2009;154:103.
[4] Liu H, Lee C, Kobayashi T, Tay C, Quan C. A new S-shaped MEMS PZT cantilever for energy harvesting from low frequency vibrations below 30 Hz. Microsystem Technologies 2012;18:497.
[5] Amin Karami M, Yardimoglu B, Inman DJ. Coupled out of plane vibrations of spiral beams for micro-scale applications. Journal of Sound and Vibration 2010;329:5584.
[6] Amin Karami M, Inman DJ. Parametric Study of Zigzag Microstructure for Vibrational Energy Harvesting. Microelectromechanical Systems, Journal of 2012;21:145.
[7] Berdy DF, Srisungsitthisunti P, Byunghoo J, Xianfan X, Rhoads JF, Peroulis D. Low-frequency meandering piezoelectric vibration energy harvester. Ultrasonics, Ferroelectrics and Frequency Control, IEEE Transactions on 2012;59:846.
[8] Sobocinski M, Leinonen M, Juuti J, Jantunen H. Monomorph piezoelectric wideband energy harvester integrated into LTCC. Journal of the European Ceramic Society 2011;31:789.
[9] Kim H, Bedekar V, Islam RA, Woo-ho L, Leo D, Priya S. Laser-machined piezoelectric cantilevers for mechanical energy harvesting. Ultrasonics, Ferroelectrics and Frequency Control, IEEE Transactions on 2008;55:1900.
[10] Lee B, Lin S, Wu W, Wang X, Chang P, Lee C. Piezoelectric MEMS generators fabricated with an aerosol deposition PZT thin film. Journal of Micromechanics and Microengineering 2009;19:065014.

[11] Xu R, Lei A, Dahl-Petersen C, Hansen K, Guizzetti M, Birkelund K, Thomsen EV, Hansen O. Screen printed PZT/PZT thick film bimorph MEMS cantilever device for vibration energy harvesting. Sensors and Actuators A: Physical 2012;188:383.
[12] Shen D, Park J-H, Ajitsaria J, Choe S-Y, Wikle III HC, Kim D-J. The design, fabrication and evaluation of a MEMS PZT cantilever with an integrated Si proof mass for vibration energy harvesting. Journal of Micromechanics and Microengineering 2008;18:055017.
[13] Yu HG, Wolf R, Deng K, Zou L, Tadigadapa S, Troilier-McKinstry S. Fabrication and performance of d33-mode lead-zirconate-titanate (PZT) MEMS accelerometers. vol. 4559, 2001. p.130.
[14] Ng TH, Liao WH. Sensitivity Analysis and Energy Harvesting for a Self-Powered Piezoelectric Sensor. Journal of Intelligent Material Systems and Structures 2005;16:785.
[15] Aktakka EE, Peterson RL, Najafi K. Multi-layer PZT stacking process for piezoelectric bimorph energy harvesters. Diamond 2011;10:8000.
[16] Lee BS, Lin SC, Wu WJ. Fabrication and Evaluation of a MEMS Piezoelectric Bimorph Generator for Vibration Energy Harvesting. Journal of Mechanics 2010;26:493.
[17] Muralt P. Recent Progress in Materials Issues for Piezoelectric MEMS. Journal of the American Ceramic Society 2008;91:1385.
[18] Du X-h, Zheng J, Belegundu U, Uchino K. Crystal orientation dependence of piezoelectric properties of lead zirconate titanate near the morphotropic phase boundary. Applied Physics Letters 1998;72:2421.
[19] Chen S-Y, Chen IW. Temperature–Time Texture Transition of Pb(Zr1−xTix)O3 Thin Films: I, Role of Pb-rich Intermediate Phases. Journal of the American Ceramic Society 1994;77:2332.
[20] Sanchez L, Potrepka D, Fox G, Takeuchi I, Polcawich R. Improving PZT Thin Film Texture Through Pt Metallization and Seed Layers. MRS Online Proc. Library 2011;1299.
[21] Baker J, Roundy S, Wright P. Alternative geometries for increasing power density in vibration energy scavenging for wireless sensor networks. Proc. 3rd Int. Energy Conversion Engineering Conf.(San Francisco, CA, Aug.), 2005. p.959.
[22] Park J-H, Kang J, Ahn H, Kim S-B, Liu D, Kim D-J. Analysis of Stress Distribution in Piezoelectric MEMS Energy Harvester Using Shaped Cantilever Structure. Ferroelectrics 2010;409:55.
[23] Frey A, Seidel J, Schreiter M, Kuehne I. Piezoelectric MEMS energy harvesting module based on non-resonant excitation. Solid-State Sensors, Actuators and Microsystems Conference (TRANSDUCERS), 2011 16th International, 2011. p.683.
[24] Goldschmidtboeing F, Woias P. Characterization of different beam shapes for piezoelectric energy harvesting. Journal of micromechanics and microengineering 2008;18:104013.
[25] Defosseux M, Allain M, Basrour S. Comparison of different beam shapes for piezoelectric vibration energy harvesting. Proc. of PowerMEMS 2010 The 10th International Workshop on Micro and Nanotechnology for Power Generation and Energy Conversion Applications, 2010.

Chapter 9

Dispersion Passivated Copper Ink Printing: a New Approach for Oxidation Resistance

Ronnie Varghese,[1] Yu Zhao,[1] Elliot McCallister,[1] Alex O. Aning[2] and Shashank Priya[1,*]

[1]Center for Energy Harvesting Materials and Systems (CEHMS), Bio-Inspired Materials and Devices Laboratory (BMDL), Virginia Tech, Blacksburg, VA 24061

[2]Materials Science and Engineering Department, Virginia Tech, Blacksburg, VA 24061, USA

Abstract

In this paper, we report a new approach to passivation of copper thin films and interconnects using metallic oxide dispersion. Unlike metallic doping or alloying, this method is uniquely suited to wet chemical deposition techniques like electroplating, ink jet printing, spin coating, sol-gel, etc. Sol-gel chemistry is used to introduce dopant metallic alkoxides into the copper ink or solution. Subsequent thermal treatment of the copper thin film or interconnect line brings the dopants to the surface where they form a passivating oxide layer. Magnesium and Aluminum were chosen as the dopant metals and their alkoxides were employed. The stabilized sols of Magnesium and Aluminum alkoxides were mixed with the copper ink in < 5 mol% concentrations and the copper solutions spun coated on oxidized silicon substrates. The resistivity was measured by Van der Pauw 4 point probe to be 10.1 μΩ-cm which is 10x that of pure copper (1.67 μΩ-cm). Corrosion testing show that doped copper films has a high resistivity outer protective layer of the dopant metallic oxide.

Introduction

Copper based interconnects form the basic routing in most CMOS based CPU chips. Miniaturized Copper based coils are being in RF devices and inductive energy harvesters. Due to easier availability, processing and reliability of Copper, it has been the conductor of choice in printed circuitry. Copper is easily oxidized during ambient air heat treatment and has low oxidation resistance. Copper ink based 3D printing has been developed for industrial use but suffers from the need to cure the ink in an oxygen free environment (usually forming or inert gas). Pulsed light or photonic sintering has been employed to cure Copper ink with minimal oxidation in air[1]. The micro to milli seconds of high intensity pulsed UV light exposure cause extremely localized heating without damaging any organic substrate below the printed copper ink. However, such light sources and control equipment are expensive and require special ozone sensors and abatement. Below 10nm, the melting point of copper decreases considerably and so nanoparticle based ink has been developed to lower curing or sintering temperature This methodology was used to lower the sintering temperature to 200°C but with the consequence of high resistivity of 40 μΩ-cm [2]. Organically stabilized copper nanoparticle ink has been shown to enable low temperature curing albeit in inert or forming gas ambience[3]. However, this post cured Copper is still susceptible to oxidation whilst copper interconnects alloyed with Al has been shown to have high oxidation resistance[4]. Therefore, a post cured corrosion resistant copper ink would be extremely advantageous.

For ambient atmosphere sintering, alloying Cu metallization interconnects with a few atomic % of Al and Mg has been shown to be very effective[5]. The oxidation resistance of these alloyed Cu was orders of magnitude greater than that of undoped Cu. On heat treatment in ambient air, the Al and Mg, though deposited as Cu-Al and Cu-Mg alloys, were found to diffuse out to the Cu

surface and oxidize to form a passivating layer. The key properties of the alloying element is that it should have a) high diffusivity in copper, b) high free energy formation of oxide, c) below Cu in Ellingham diagram, d) minimal increase in the resistivity of copper, e) low solubility in copper and f) alloy should be mechanically stronger[6].

In order to replicate the same phenomenon in Copper nanoparticle ink, Al and Mg nanoparticles have to be used. Al and Mg nanoparticles are considered biological[7] and explosion[8] hazards for ambient use. One approach is to use core-shell nanoparticles of Cu-Al and Cu-Mg and such technology has been tried to create Cu-Ag core-shell nanoparticles[9]. However the fabrication process is complicated and often unstable. At the time of writing, we were unable to find a Cu-Al or Cu-Mg core-shell process in literature. So we decided to explore the possibility of using organometallic compounds of Al and Mg. Such compounds were found to be rare, difficult to synthesize and highly unstable. However, alkoxides of Al and Mg are ready available and stable especially in the liquid form necessary to mix with the Cu ink. Salts of Al and Mg were ruled out due to their hygroscopic nature. Al and Mg alkoxides can also be diluted or dissolved to the required doping concentration in organic solvents. However, Al and Mg alkoxides have oxygen directly bonded to the metal ion and so we are not introducing the dopant metal into copper as an alloying element but as oxide dispersed in it. Al_2O_3 and MgO dispersion strengthened copper has been used for decades in copper wires and high temperature applications [10, 11].

Experimental Procedures

We procured Copper nanoparticle ink Cu-iJ70 from Applied Nanotech, Inc. and as per the MSDS, it contains Copper in ethyl acetate, glycol ether and other proprietary compounds. The Cu-iJ70 ink has particle sizes ranging from 20-100nm with an average of 70nm. The solid

content weight is 40%. The vendor recommended conditions for pyrolysis is 100C for 30-60min and a final anneal in forming gas N_2/H_2 (H_2 <4%) at 350°C for 45min (with 30min ramp). As per the vendor specifications, the final resistivity of the cured ink is 5-7 μΩ-cm.

To this base ink, we added the Al and Mg alkoxides dissolved in organic solvents with or without chelating agents. The alkoxides employed were Aluminum-tri-sec-butoxide (97%, Sigma Aldrich), Magnesium ethoxide (98%, Sigma Aldrich) and Magnesium methoxide in methanol (6-10 wt. %, Sigma Aldrich). The solvents utilized were Ethyl acetate (99.8%, Sigma-Aldrich), 1-butanol (99%, Sigma-Aldrich) and 1-Octanol (99%, Alfa-Aesar). The chelating agents were Triethanolamine (TEA, 99%, Sigma-Aldrich), Diethanolamine (DEA, 99%, Sigma-Aldrich) and Acetic Acid (99%, Sigma-Aldrich). Acetic Acid has been used to stabilize Mg methoxide in methanol solutions[12]. DEA and TEA were used to stabilize Al tri-sec-butoxide in butanol solutions[13]. The doping concentration was typically 1-5mol% in copper ink. A summary of the dopant solutions are tabulated below.

Table 9.1 Ingredients of the Dopant solutions

Designation	**Metal Alkoxide**	**Solvent**	**Chelating Agent**
A	Al tri-sec-butoxide	1-butanol	TEA
B	Al tri-sec-butoxide	1-butanol	DEA
C	Al tri-sec-butoxide	Ethyl Acetate	DEA
D	Al tri-sec-butoxide	Ethyl Acetate	TEA
E	Magnesium methoxide	Methanol	Acetic Acid
F	Magnesium methoxide	Methanol	DEA
G	Magnesium methoxide	2-Methoxyethanol	
I	Magnesium ethoxide	2-Methoxyethanol	
O	Magnesium methoxide	Methanol, Octanol	DEA
K	Al tri-sec-butoxide	Octanol	DEA
L	Al tri-sec-butoxide	Octanol	TEA

The doped ink was then spun coated for 5sec at 500rpm, 5sec at 1500rpm and finally for 20sec at 3000rpm on 1000A SiO_2 on 0.5mm Si substrates. The as coated samples were then pyrolized at 120C on a hot place for 40sec and then annealed in ambient air in a furnace at 350C for 45min (ramp rate of 30min). The resistivity of the uniformly coated films was measured using Van der Pauw 4 point probe method on a Keithley SCS 4200. The films were then annealed 2 more times at the same conditions and X-ray diffraction studies were performed after each anneal. To determine the extent of Copper oxidation with depth, X-ray photoelectron spectroscopy depth profile of the thin films were also attempted.

Results and Discussion

Firstly, we were unable to pyrolyse our doped Copper samples for the vendor recommended 30-60min in air as the dopant solution caused agglomeration of the copper film. Only dopant solutions C, E, F, K, L and O gave stable mixtures with the ANI copper ink and therefore the most uniform spun coated films. After pyrolysis and furnace sintering, an SEM image of doped Copper ink E sample shows similar density of structure as undoped copper ink sample.

a)

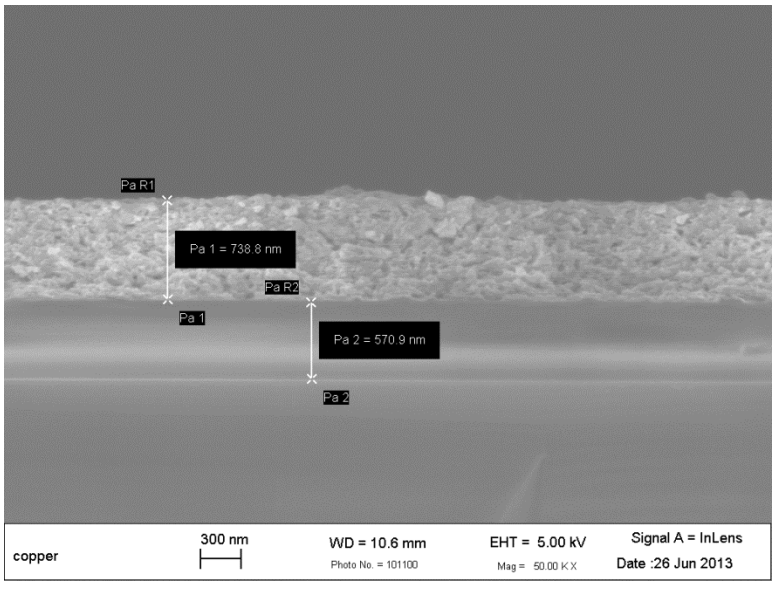

b)

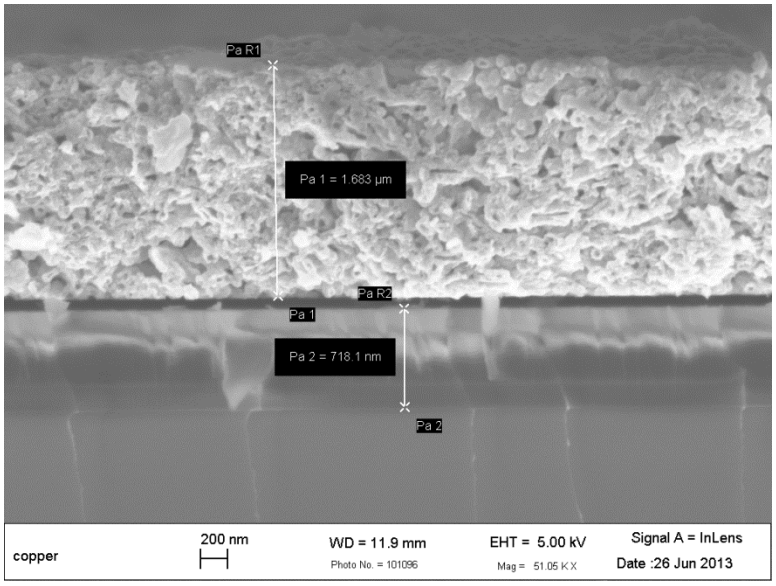

Figure 9.1 SEM of a) undoped ANI Copper ink vs. b) doped Copper ink sample E

The resistivity of doped copper ink samples 8.5, 12.1, 10.1, 10.6 and 9.3 μΩ-cm respectively for C, E, K, L and O inks (average of 10.1 μΩ-cm) whilst that of the ANI Copper ink was immeasurable (as it was oxidized). Please note that for all samples, in order to break through any surface oxide prior to resistivity data collection, the probe tips were lightly impacted on thin film surface at least 5 times. XPS elemental depth profile was futile for determining the level of copper oxidation with depth. The oxygen of the Al and Mg oxides masked the copper oxidation extent. X-ray Diffraction studies were more successful at discriminating the extent of oxidation from the 3 ambient air anneals. From XRD analysis, the Copper is (220) textured in almost all samples. The undoped Copper has an increase in CuO formation and decrease in Cu. Doped Copper shows an increase in Cu and no change in CuO – probably due to dopant induced grain size increase of Cu. For comparison, drop vs. spin coated undoped Cu samples, that was air dried at room temperature for 12hrs, show Cu(22O) and CuO vs. Cu(22O), Cu_2O, CuO and Cu (200) respectively. Clearly, Al_2O_3 and MgO are amorphous at the curing temperature of 350C.

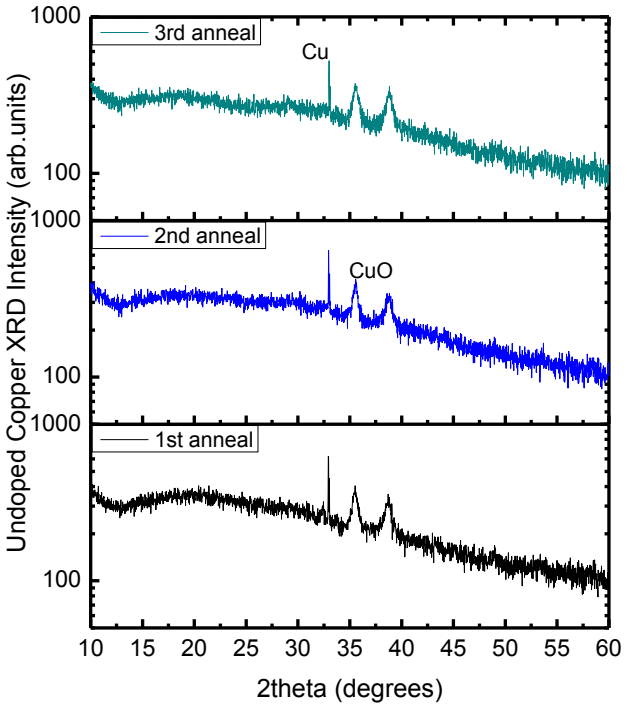
3rd anneal
Cu
2nd anneal
CuO
1st anneal
Undoped Copper XRD Intensity (arb.units)
1000
100
10 15 20 25 30 35 40 45 50 55 60
2theta (degrees)

a)

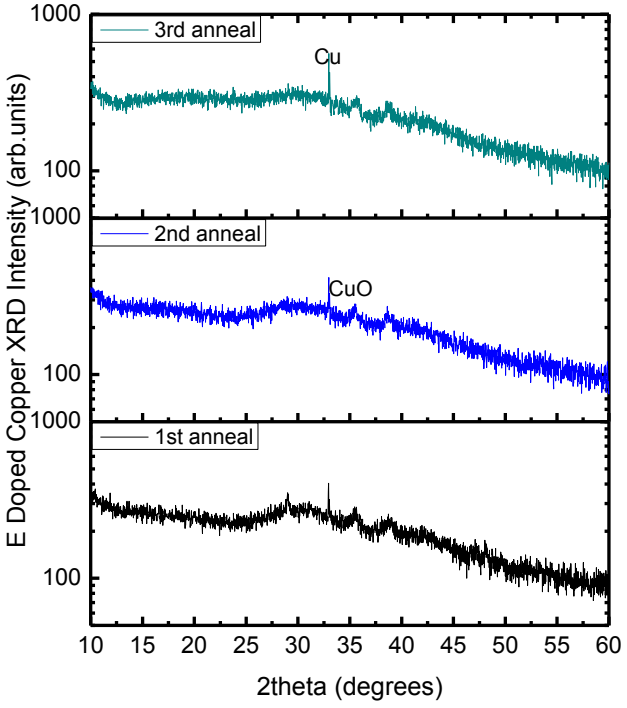
3rd anneal
Cu
2nd anneal
CuO
1st anneal
E Doped Copper XRD Intensity (arb.units)
1000
100
10 15 20 25 30 35 40 45 50 55 60
2theta (degrees)

b)

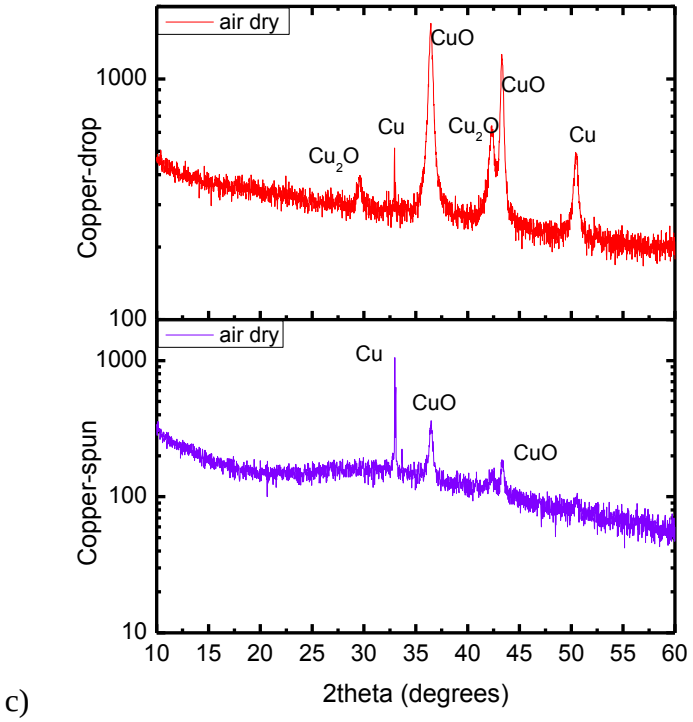

c)

Figure 9.2 XRD data for a) undoped Copper and b) E-doped Copper after 3 anneals vs c) undoped ink air dried

The oxidation of pure copper in air at 300C has been studied and the copper ion out diffusion to form Cu_2O at the surface can be reduced by doping with Al and Mg. In the latter case, the Cu2O formation is suppressed and CuO formation by oxygen in-diffusion will only occur[14]. Despite having oxygen present throughout the bulk of the thin film, the doped copper is conductive. We postulate that the Al and Mg oxides form a thin coating around Copper agglomerates that are electrically connected and that this passivating oxide is suppressing Cu_2O formation.

To prove our hypothesis, we mixed the doping solutions with Copper 325 mesh (99.999% Sigma Aldrich) powder. These dopant soaked ~44 micron Cu particles were then pyrolysed at 150C for an hour (ramp rate 1C/min) and then annealed at 350C for an hour (ramp rate 10C/min), both in air. We obtained reddish brown copper agglomerates that were oxidized on the outside (as

determined by a continuity check with a multimeter) but were as conductive as copper powder in the inside.

Conclusion

We report the successful use of Aluminum and Magnesium alkoxide in Copper nanoparticle ink to alleviate the oxidation of Copper during ambient air sintering at 350C. On curing, these alkoxides in <5 mol% concentrations created copper agglomerates in a matrix of Aluminum or Magnesium oxides. These copper agglomerates were fused enough to create electrical connectivity. To prove the matrix theory, we created slurries of pure micron sized copper particles in the alkoxide solutions and then sintered them in crucibles. The surfaces of these copper agglomerates were oxidized and not conductive but the interior was electrically conductive. Equally, the doped copper films have a high resistivity outer protective layer of the dopant metallic oxide around its copper clusters. The resistivity of the doped copper thin films was measured by Van der Pauw 4 point probe to be 10.1 μΩ-cm which is 10x that of pure copper (1.67 μΩ-cm).

Acknowledgements: The authors gratefully acknowledge the financial support from ***Air Force Office of Scientific Research (AFOSR)***.We are also greatly indebted to Donald Leber, Micron Lab Manager, and Tong Liu, both of the ECE Department at Virginia Tech for assistance with the electrical measurements.

References

[1] Kim H-S, Dhage S, Shim D-E, Hahn HT. Intense pulsed light sintering of copper nanoink for printed electronics. Appl. Phys. A 2009;97:791.

[2] Cho MS, Choi WH, Kim SG, Kim IH, Lee Y. A Low Sintering Temperature and Electrical Performance of Nanoparticle Copper Ink for Use in Ink-Jet Printing. Journal of Nanoscience and Nanotechnology 2010;10:6888.

[3] Lee B, Kim Y, Yang S, Jeong I, Moon J. A low-cure-temperature copper nano ink for highly conductive printed electrodes. Current Applied Physics 2009;9:e157.

[4] Hong S-H, Zhu Y, Mimura K, Isshiki M. Role of Al2O3 layer in oxidation resistance of Cu–Al dilute alloys pre-annealed in H2 atmospheres. Corrosion Science 2006;48:3692.

[5] Lanford WA, Ding PJ, Wang W, Hymes S, Muraka SP. Low-temperature passivation of copper by doping with Al or Mg. Thin Solid Films 1995;262:234.

[6] Lanford WA, Ding PJ, Wang W, Hymes S, Murarka SP. Alloying of copper for use in microelectronic metallization. Materials Chemistry and Physics 1995;41:192.

[7] Braydich-Stolle LK, Speshock JL, Castle A, Smith M, Murdock RC, Hussain SM. Nanosized Aluminum Altered Immune Function. ACS Nano 2010;4:3661.

[8] Bouillard J, Vignes A, Dufaud O, Perrin L, Thomas D. Ignition and explosion risks of nanopowders. Journal of Hazardous Materials 2010;181:873.

[9] Magdassi S, Grouchko M, Kamyshny A. Copper Nanoparticles for Printed Electronics: Routes Towards Achieving Oxidation Stability. Materials 2010;3:4626.

[10] Groza J. Heat-resistant dispersion-strengthened copper alloys. JMEP 1992;1:113.

[11] Groza JR, Gibeling JC. Principles of particle selection for dispersion-strengthened copper. Materials Science and Engineering: A 1993;171:115.

[12] Kim JY, Jung HS, Hong KS. Effects of Acetic Acid on the Crystallization Temperature of Sol–Gel-Derived MgO Nano-Powders and Thin Films. Journal of the American Ceramic Society 2005;88:784.

[13] Tadanaga K, Ito S, Minami T, Tohge N. Precursor structure and microstructure of Al2O3 xerogels prepared from aluminum-tri-sec-butoxide chemically modified with mono-, di-, tri-ethanolamines. Journal of Non-Crystalline Solids 1996;201:231.

[14] Ding PJ, Lanford WA, Hymes S, Murarka SP. Effects of the addition of small amounts of Al to copper: Corrosion, resistivity, adhesion, morphology, and diffusion. Journal of Applied Physics 1994;75:3627.

Chapter 10

Significance of Research and Further Investigations

Research Accomplishments

This dissertation compiles some of the work that went towards the realization of MEMS vibration energy harvesters. With this work we have made the following original and unique achievements:

- To overcome the lack of a methodology to model the extensive data that goes into making a Temperature-time-transformation (TTT) diagram, we derived a mathematical formulation of the TTT diagram that allows the prediction of the predominant phase and the ranking of each phase of interest. When generalized for use in the texturing of bulk ceramics, 'n' number of peaks in the related X-ray Diffraction spectra will lead to 'n' proportions and (n-1) equations.

- We reveal the first instance of a photo-elemental prediction method reported in literature. Using this method, one gains the ability to tune elemental content of thin films based on n & k. The use of an economical nondestructive technique enables lab scale implementation and the approach can be generalized for any multicomponent thin film system.

- A noninvasive, unobtrusive (clamp free; no gluing) measurement technique has been developed for asymmetrically induced magnetic strain in magnetostrictive thin films. The use of 2 AC bias permits unique solution of magnetostriction from Laser Doppler Vibrometer measured deflection.

- We disclose the first known measurement of thermal conductivity of PZT thin films and the first use of Time Domain Thermoreflectance (TDTR) in the study of texturing of thin films. We exploit TDTR for the first known ex-situ analysis of heterogeneity at a buried PZT-Pt interface. In doing so, we were able observe trends of PZT's thermal properties with texture (especially k and G_{PZT-Pt} with (111)).

- The first nondimensional Energy Harvester (to our knowledge at time of writing) has been developed where we utilize the hardening force between magnets loaded on piezo harvesters to coerce the resonance of the piezo harvester to be no longer dependent on the dimensions of harvester but only on the stiffness force between the magnets. Such piezomagnetoelastic technology can be employed as a self-encapsulating package harvester that in an AC magnetic field doubles as a magnetoelectric harvester.

- We created the first Magnetoelectric Macro Fiber composite (ME MFC) in erstwhile reported literature that is capable of < 300Hz resonance without a tip mass. Prior to their singulation into fibers, we took advantage of a <150°C solder bonding process in the fabrication of the ME composites.

- Dispersion strengthened copper ink process was developed not for mechanical property improvement but for improving oxidation resistance of printed or spun coated Copper thin films. Stable Al and Mg alkoxide solutions were formulated and mixed with nanoparticle copper ink to form Copper thin films that are 6x more resistive than bulk copper.

- A Tip mass free <100Hz vibration MEMS energy harvester was designed and fabricated using novel Si and bulk Piezo micromachining. This structure being curvilinear required the development of a curved IDE pattern to enable operation in d33 mode. A wafer level testing

method using a pogo pin PCB tester is also disclosed. We utilized Micro Water jet for the micromachining of piezoelectric ceramics.

- Figure of Merits (FOM) in Energy Harvesting utilize Power density calculations and therefore MEMS devices with their small volumes tend to have large power densities. In most applications, energy harvesters are used to charge a battery or super capacitor. Therefore a FOM which is weighted more towards its ability to do so is more appropriate. We therefore proposed a new FOM that can report the energy harvester's capability in the same metric as that of a battery – milliAmpere hour (mAhr). This FOM is calculated from the current generated and the resonant frequency of the harvester – (Current*3600secs/hr)/frequency. Energy harvester performance is evaluated by the voltage generated at a) low matching load, b) low natural frequency and c) low acceleration. The new FOM is proportional to voltage and inversely proportional to impedance and frequency. Table 10.1 compiles the state of the art in Piezoelectric MEMS energy harvesting at the time of writing. Table 10.2 discloses the new FOM and compares it against the industry standard FOM. It is clear that our energy harvester reported in Chapter 8 has the capabilities close to that of typical AA battery (2000 mAhr).

Table 10.1 Piezoelectric MEMS Energy harvester performance comparison

Harvester types	**Voltage** *(V)*	**Power** *(μW)*	**Acceleration** *(g = 9.8m/s2)*	**Volume** *(mm3)*	**Resonant Frequency** *(Hz)*	**Bandwidth** *(3dB)*
d31 PZT Sol[1]	0.89	2.16	1	0.1944	608	
d31 PZT Sol[2]	0.16	2.15	2	0.652	461.15	
d31 AD PZT[3]	1.792	2.765	2.5	0.4245	255.9	
d33 AD PZT[3]	2.292	1.288	2	0.612	214	
d33 PZT Sol[4]	3	1		0.027	13900	
d33 poly-PZT[5]	1.6	1.4	2	0.3248	870	
d31 AlN[6]	5.2	60	2	12.7272	592	
d31 Epi-PZT PLD[7]	0.005	0.0055	1.02	0.0000296	971	
d31 Epi-PZT RF Sputter[8]	2.6	244	5.1	4.625	126	
d31 Epi-PZT RF Sputter[9]	0.27	0.13	1	0.153	2297	6.3
d31 NKNT-BF Sol[10]	0.38	1.82	1	7	130	
S-shape PZT[11]	0.042	0.00117	0.06		27.4	3
d31 PZT frequency-up-conversion[12]	0.05	0.12	0.8	17.5	36	22
d31 PZT[13]	1.2	67.9	1	27.3	419	26.3
PZT Ultra-wide bandwidth[14]	0.8	45		0.021	1300	400
Microwater jet CZ4 bimorph	1.34	53	0.1	93.1	89.3	5.70
Microwater jet CZ5 unimorph	0.38	7.232	0.1	64.881	37.75	4.25

Table 10.2 Comparison of MEMS Harvester performance: Figure of Merit industry standard vs. proposed

Harvester types	**Power Density** *(mW/cc)*	**Normalized Power Density** *(mW/cc/g^2)*	**NPD *BW** *(mW-Hz/cc/g^2)*	**NPD*BW/f_r** *(mW/cc/g^2)*	**New FOM (Power/Voltage x 3600/f_r)** *(mW/V)*(3600/Hz)*1000= mAh*	**New FOM density/g^2** *mAh/cc/g^2*
d31 PZT Sol[1]	11.11	11.11			14.3702	73920.76
d31 PZT Sol[2]	3.30	0.82			104.9008	40222.70
d31 AD PZT[3]	6.51	1.04			21.7065	8181.48
d33 AD PZT[3]	2.10	0.53			9.4534	3861.70
d33 PZT Sol[4]	37.04				0.0863	
d33 poly-PZT[5]	4.31	1.08			3.6207	2786.86
d31 AlN[6]	4.71	1.18			70.1663	1378.27
d31 Epi-PZT PLD[7]	185.81	178.60			4.0783	132429244.50
d31 Epi-PZT RF Sputter[8]	52.76	2.03			2681.3187	22289.30
d31 Epi-PZT RF Sputter[9]	0.85	0.85	5.35	0.0023	0.7546	4932.07
d31 NKNT-BF Sol[10]	0.26	0.26			132.6316	18947.37
S-shape PZT[11]					3.6601	
d31 PZT frequency-up-conversion[12]	0.01	0.01	0.24	0.0065	240.0000	21428.57
d31 PZT[13]	2.49	2.49	65.41	0.1561	486.1575	17807.97
PZT Ultra-wide bandwidth[14]	2142.86				155.7692	
Microwater jet CZ4 bimorph	0.57	56.93	**324.49**	**3.6337**	1594.4912	**1712665.04**
Microwater jet CZ5 unimorph	0.11	11.15	47.37	**1.2549**	1814.9320	**2797324.38**

Future Work

This research work is an improvement on the existing knowhow of MEMS based energy harvesters and certainly, further research can overcome the shortcomings of and pitfalls in this work with better processes, methods or devices. A few suggestions on avenues to expand this work are:

- The TTT diagram model can be expanded to include non-PZT systems and those which have more phases to model.
- Perpendicular mode magnetostriction measurements of thin films by Laser Doppler vibrometry can be attempted.
- The TDTR work can be expanded to include studies of the effect of intentional seed layers on PZT texturing and thermal properties of other piezoelectric thin films.
- The Circular Labyrinth structure can be morphed for other applications. For example, it can be used a micro accelerometer for low frequency operation.
- The design of the Circular Labyrinth structure can be optimized with greater stress distribution at each of its bends. The ensuing stress enhancement can improve harvesting performance.
- The stiffness of the ME MFC harvester can be modulated to lower the resonant frequency to below 100Hz.

- The PiezoCap concept can be expanded into a ball shaped harvester where a magnetic sphere in the annular space of a larger harvester sphere can actuate PiezoCap's on the latter's surface. This ball harvester (see figure below) can be conceived to be a multi-directional harvester.

Figure 10.1 Ball Harvester concept using PiezoCap technology

References

[1] Fang H-B, Liu J-Q, Xu Z-Y, Dong L, Wang L, Chen D, Cai B-C, Liu Y. Fabrication and performance of MEMS-based piezoelectric power generator for vibration energy harvesting. Microelectronics Journal 2006;37:1280.

[2] Shen D, Park J-H, Ajitsaria J, Choe S-Y, Wikle III HC, Kim D-J. The design, fabrication and evaluation of a MEMS PZT cantilever with an integrated Si proof mass for vibration energy harvesting. Journal of Micromechanics and Microengineering 2008;18:055017.

[3] Lee B, Lin S, Wu W, Wang X, Chang P, Lee C. Piezoelectric MEMS generators fabricated with an aerosol deposition PZT thin film. Journal of Micromechanics and Microengineering 2009;19:065014.
[4] Jeon YB, Sood R, Jeong Jh, Kim SG. MEMS power generator with transverse mode thin film PZT. Sensors and Actuators A: Physical 2005;122:16.
[5] Muralt P, Marzencki M, Belgacem B, Calame F, Basrour S. Vibration Energy Harvesting with PZT Micro Device. Procedia Chemistry 2009;1:1191.
[6] Elfrink R, Kamel T, Goedbloed M, Matova S, Hohlfeld D, Van Andel Y, Van Schaijk R. Vibration energy harvesting with aluminum nitride-based piezoelectric devices. Journal of Micromechanics and Microengineering 2009;19:094005.
[7] Reilly E, Wright P. Modeling, fabrication and stress compensation of an epitaxial thin film piezoelectric microscale energy scavenging device. Journal of Micromechanics and Microengineering 2009;19:095014.
[8] Morimoto K, Kanno I, Wasa K, Kotera H. High-efficiency piezoelectric energy harvesters of c-axis-oriented epitaxial PZT films transferred onto stainless steel cantilevers. Sensors and Actuators A: Physical 2010;163:428.
[9] Isarakorn D, Briand D, Janphuang P, Sambri A, Gariglio S, Triscone J, Guy F, Reiner J, Ahn C, De Rooij N. The realization and performance of vibration energy harvesting MEMS devices based on an epitaxial piezoelectric thin film. Smart Materials and Structures 2011;20:025015.
[10] Kim S-H, Leung A, Koo CY, Kuhn L, Jiang W, Kim D-J, Kingon AI. Lead-free (Na0.5K0.5)(Nb0.95Ta0.05)O3–BiFeO3 thin films for MEMS piezoelectric vibration energy harvesting devices. Materials Letters 2012;69:24.
[11] Liu H, Lee C, Kobayashi T, Tay C, Quan C. A new S-shaped MEMS PZT cantilever for energy harvesting from low frequency vibrations below 30 Hz. Microsystem Technologies 2012;18:497.
[12] Liu H, Lee C, Kobayashi T, Tay CJ, Quan C. Piezoelectric MEMS-based wideband energy harvesting systems using a frequency-up-conversion cantilever stopper. Sensors and Actuators A: Physical 2012;186:242.
[13] Aktakka EE, Peterson RL, Najafi K. A self-supplied inertial piezoelectric energy harvester with power-management IC. Solid-State Circuits Conference Digest of Technical Papers (ISSCC), 2011 IEEE International, 2011. p.120.
[14] Hajati A, Kim S-G. Ultra-wide bandwidth piezoelectric energy harvesting. Applied Physics Letters 2011;99:083105.

Chapter 11

Appendix

Other New Technologies and Techniques for Energy Harvesters and Sensors

Magnetoelectric Thin Film Transformer for Sensing

A single layer transformer structure is shown below (Figure 11.1). It consists of a NFO dot over a patterned Platinum electrode which in turn is over a patterned or unpatterned PZT thin film. A diffusion barrier layer of Pt also serves as the ground for both input (ring) and output (dot) electrodes.

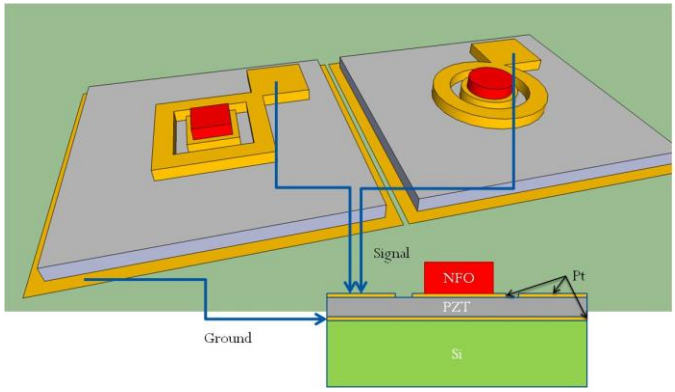

Figure 11.1 Schematic of a Single Layer Transformer structure

We have utilized photo etched metal shadow masks to deposit patterned thin films (see Table 11.1 below for process sequence). We also used magnets (shown in blue in Figure 11.2) to protect the underlying layer's electrical pads from deposition.

Table 11.1 Shadow mask based fabrication process flow

Process	Mask orientation	Magnets
SiO2 deposition		
Ti deposition		
Blanket bottom Pt deposition		
PZT mask		
PZT deposition		
PZT annealing		
1st Ring pattern/mask		
Pt deposition		
1 Pad protection		1
PZT deposition		1
PZT annealing		
2nd Ring pattern/mask	Rotate 90deg	
Pt deposition		
2 Pad protection		2
PZT deposition		2
PZT annealing		
3nd Ring pattern/mask	Rotate 90deg	
Pt deposition		
3 Pad protection		3
PZT deposition		3
PZT annealing		
4th Ring pattern/mask	Rotate 90deg	
Pt deposition		
4 Pad protection		4
PZT deposition		4
PZT annealing		
Final Ring+Dot pattern/mask		
Pt deposition		

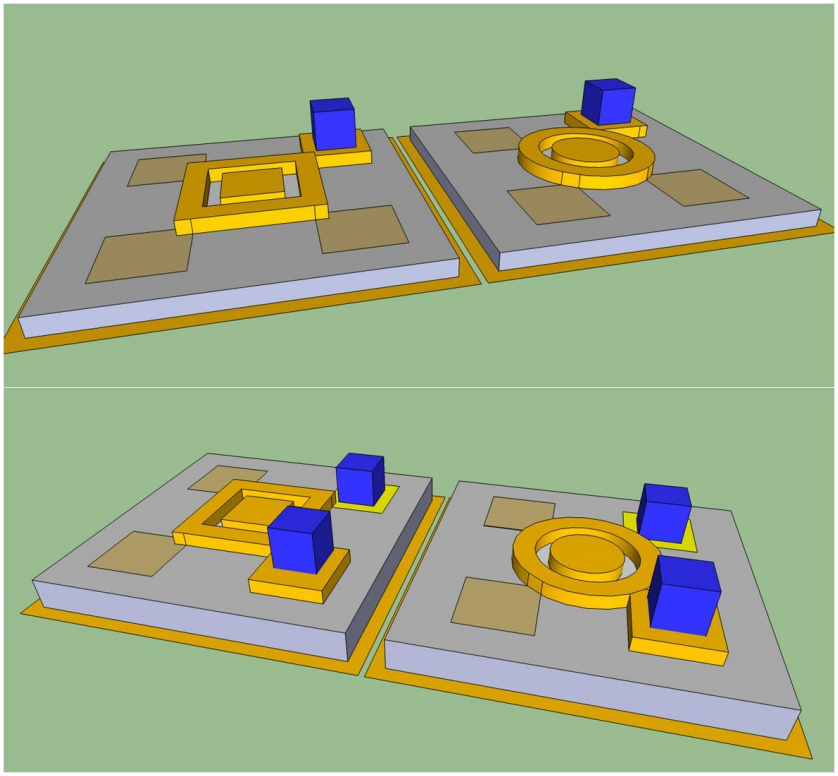

Figure 11.2 Shadow mask processing using metal shadow mask and magnets (to protect electrical pads from deposition)

We had to develop custom testing capability for testing our ME devices (Figure 11.3). We procured a Agilent E4991A Impedance Analyzer, Jmicro Technology probe station and GGB Picoprobes with special wire tethers (to create common ground between input and output).

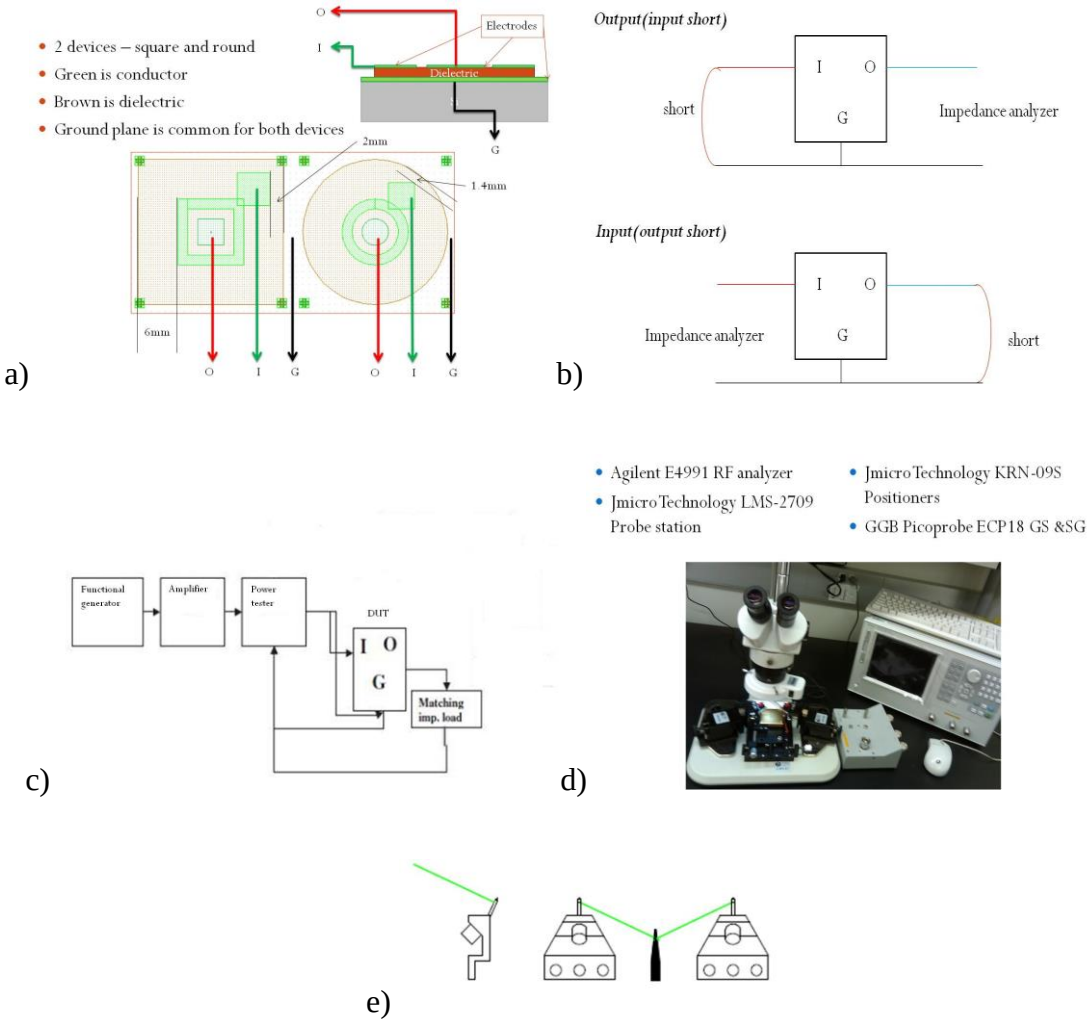

Figure 11.3 Electrical connections and equipment for High Frequency ME testing – a) DUT (device under test), b) impedance testing schematic, c) Gain testing schematic, d) test bench and e) probe tip with special wired tethers for common ground

We developed and characterized the single layer thin film Unipoled transformer device and then using Silicon micromachining processes like Deep RIE, decrease the substrate clamping effect on the ME device by backside removal of the vestigial substrate material (Figure 11.4). The

location of the neutral plane or axis in the device stack decides the bending oscillations. By manipulating the location of the neutral plane with the geometric midplane of the active layers, we can manipulate the bending moments and frequencies. Moreover, a fixed boundary condition at the edge of the device (see bottom inset of figure below) can be used to induce bending modes and reflect the surface acoustic waves back into the device. This work is pending.

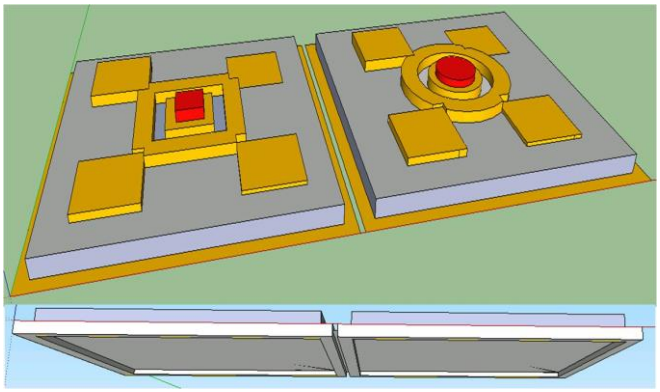

Figure 11.4 Unipoled transformer stack with the backside Si removed (shown in lower part)

Flow Induced Vibration from Vortex Shedding

For energy harvesting applications in confined forced flow systems and in areas exposed to momentary gusts or sudden turbulence, a simple Piezo macro fiber composite harvester is envisioned. If clamped in a certain manner, away or into flow with a particular induced disturbance upstream of the harvester, the MFC can undergo harmonic oscillations at steady state flow. The wake of circular cylinder[1] or bluff object[2] has been shown to create Karman Vortex shedding and these vortices cause oscillations in a peizo element placed downstream. The former also show that if the harvester placed in the turbulent boundary layer, smaller periodic oscillations can be created.

A flow disturbance was created upstream of the harvester by a flat plate (Figure 11.5) - a) positioned 45 degrees to the wall of the wind tunnel or b) rotated from 90 degrees to -90 degrees in 1 second. Wind speed was maintained at 16 mps or 36 mph. The different configurations tested are as follows: 1) Piezo MFC is facing into the flow or away from flow (shown below), 2) an L-shaped metal piece was attached to MFC to create eddies, 3) 'Perpendicular' was MFC perpendicular to flow, 4) 'Blocking' flow mode and 5) 'Parallel' was MFC parallel to flow (shown below).

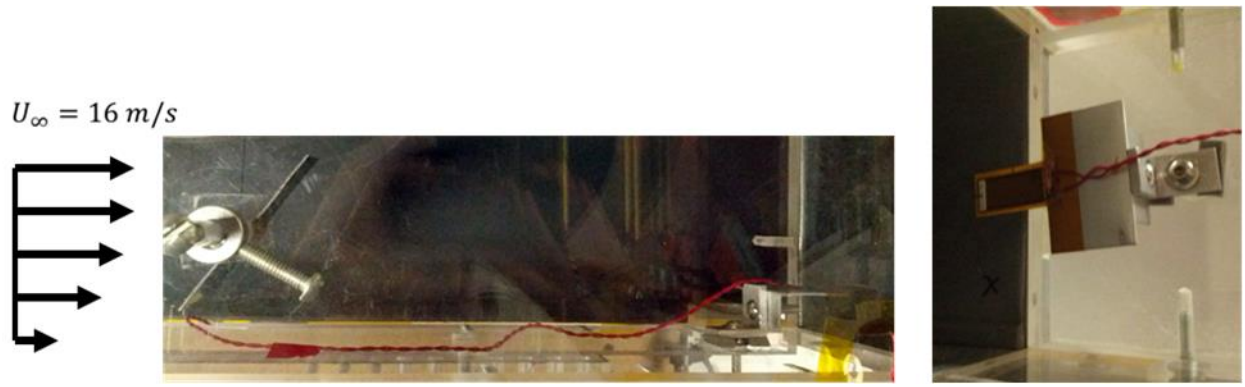

Figure 11.5 Configuration of Piezo MFC parallel to wind tunnel with free end away from flow

The results are summarized below for the 45 degree plate (Figure 11.6):

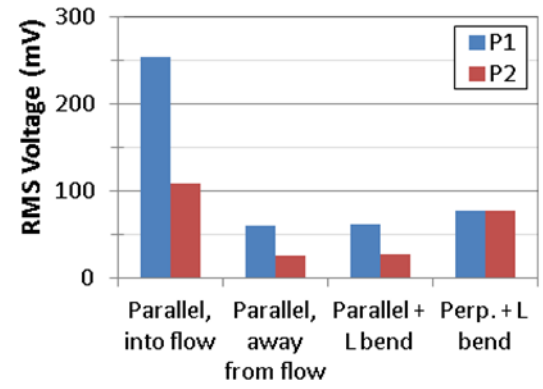

Material	Orientation	V_{RMS} (mV)	Dominant Frequencies (Hz)
P1	Parallel (free end into flow)	255	35
P1	Parallel (free end away from flow)	60	40
P1	Parallel + L bend	62	22
P1	Perpendicular + L bend	78	35
P2	Parallel	109	55
P2	Parallel	26	59
P2	Parallel + L bend	28	35
P2	Perpendicular + L bend	77	71

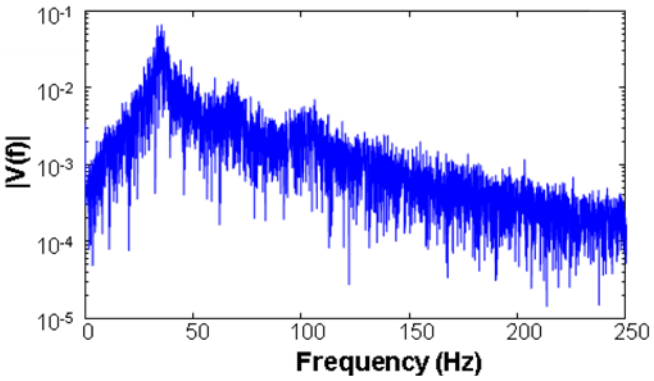

Figure 11.6 Results of a Piezo MFC with a 45 degree plate upstream (clockwise from top left): Comparison between P1 d33 and P2 type d31MFC's, Dominant frequencies for P1 vs. P2 vs. orientation and typical Voltage FRF

For the rotating plate condition, the results were less spectacular (Figure 11.7) but still demonstrate applications where random sudden gusts of flow are common.

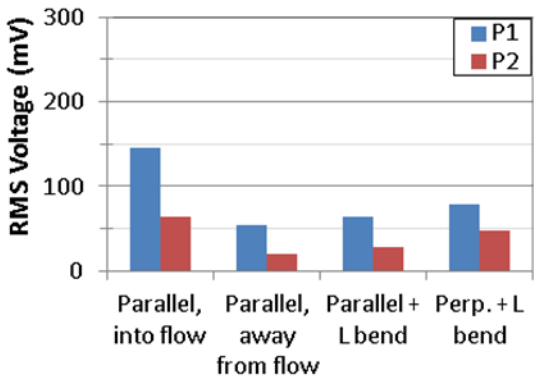

Material	Orientation	V_{RMS} (mV)	Dominant Frequencies (Hz)
P1	Parallel (free end into flow)	145	29
P1	Parallel (free end away from flow)	55	40
P1	Parallel + L bend	64	23
P1	Perpendicular + L bend	78	36
P2	Parallel	64	54
P2	Parallel	20	63
P2	Parallel + L bend	28	36
P2	Perpendicular + L bend	48	60

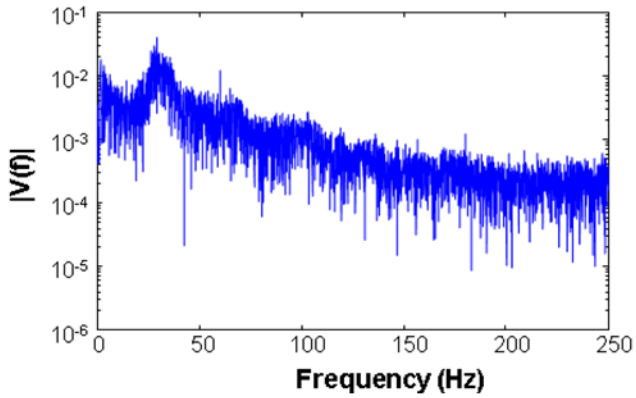

Figure 11.7 Results of a Piezo MFC with a rotating plate upstream (clockwise from top left): Comparison between P1 d33 and P2 type d31MFC's, Dominant frequencies for P1 vs. P2 vs. orientation and typical Voltage FRF

References

[1] Akaydin HD, Elvin N, Andreopoulos Y. Energy Harvesting from Highly Unsteady Fluid Flows using Piezoelectric Materials. Journal of Intelligent Material Systems and Structures 2010;21:1263.

[2] Weinstein LA, Cacan MR, So PM, Wright PK. Vortex shedding induced energy harvesting from piezoelectric materials in heating, ventilation and air conditioning flows. Smart Materials and Structures 2012;21:045003.